POLITECNICO
MILANO 1863

SCUOLA DI INGEGNERIA INDUSTRIALE
E DELL'INFORMAZIONE

Executive Summary of the Thesis

Effect of plasma triangularity on turbulent transport in the tokamak boundary

Laurea Magistrale in Nuclear Engineering - Ingegneria Nucleare

Author: Riccardo Saura

Advisor: Prof. Matteo Passoni

Co-advisors: Prof. Paolo Ricci, Maurizio Giacomin

Academic year: 2020-2021

1. Introduction

Nuclear fusion is a promising technology for energy production, consisting of the fusion of light nuclei with the release of heat. The fusion mixture, in the form of a fully ionised gas, called plasma, is contained by powerful magnetic fields ($\sim 10T$) in axial-symmetric machines called tokamak. Within these machines, the matter stratifies, forming three main zones: the core, at the centre, the hottest ($\sim 10keV$), densest and most nested region is where fusion occurs, the edge region, characterised by strong gradients, wraps the core. The outermost region, the Scrape Off Layer (SOL), where the temperature is lower ($\sim 10eV$) but fluctuations caused by turbulence are very important is in contact with the machine walls. The last two layers, called tokamak periphery, control the confinement and transport properties of the plasma, thus both the effectiveness of keeping the plasma in stable, stationary conditions and the flows of particles and heat reaching the walls of the machine. By means of additional poloidal magnetic fields it is possible to shape the tokamak periphery cross section into complex geometries that can improve these latter properties. One of the most important parameter describing the shaping effects is the triangularity. A configuration is said to be with triangularity when its cross section assume a "D" shape.
In this thesis the results of some linear and nonlinear simulations will be analysed in order to investigate the properties of some of these geometries after presenting the model used and the implementation of its linearization.

2. Modelling of Tokamak Periphery

This thesis work relies on GBS equations to describe plasma. These dimensionless laws can picture the self-consistent behaviour of a plasma composed by electrons and hydrogen ions immersed in an external magnetic field $\vec{B}$, described by its scalar intensity $B = ||\vec{B}||_2$ and its versor $\vec{b} = \frac{\vec{B}}{B}$. The model decomposes the particle dynamics into one parallel to the magnetic field, free to vary, and one perpendicular to it, dependent on the other described fields. This approximation is called drift-reduced. In this way it is possible to describe the field by means of six mutually independent scalar variables: the number density n i.e. the number of particle of each species per unit volume, the electronic tem-

perature T_e, the ion temperature T_i, the electric potential ϕ, the magnetic potential ψ, and the parallel ion velocity $V_{\parallel,i}$. The two potentials describe the electromagnetic fields trough the equations $\vec{E} = \nabla\phi - \frac{1}{c}\frac{\partial\psi\vec{b}}{\partial t}$ and $\vec{B} = \nabla\times(\psi\vec{b})$. In order not to include phenomena not physically relevant the magnetic potential $\psi\vec{b}$ has been imposed to be parallel to the equilibrium magnetic field. To make GBS equations more handily, the curvature field is introduce $\vec{\kappa} = \vec{b}\cdot\nabla\vec{b}$ and the further operators are used: the parallel gradient $\nabla_\parallel = \vec{b}\cdot\nabla$ and the perpendicular gradient $\nabla_\perp = \vec{b}\times(\nabla\times\vec{b})$, the curvature operator $C(\cdot) = \frac{B}{2}(\nabla\times\frac{\vec{b}}{B})\cdot\nabla(\cdot)$. Also, two dependent variables are included: the vorticity $\omega = \nabla^2_\perp\phi$ and electron parallel velocity $V_{\parallel,e} = \nabla^2_\perp\psi$. The set of equations is too long to be reported here, for a complete discussion please refer to [1, 2].
From adimensionalisation, two important parameters emerge. The first, the dimensionless resistance ν, takes into account collisions between particles within the plasma, the second, the ion to electron temperature ratio τ, measures the importance of typical ion temperature with respect to electrons' one. The values at which temperature and density are normalised are those typical in the edge of a tokamak such as TCV, in Lausanne, Switzerland: $n_0 = 10^{-19}m^{-3}$, $T_{0e} = 20eV$.

2.1. Simulations Geometry

GBS equations portray the plasma dynamics in the entire volume of the tokamak. The problem, therefore, through the fields describing the plasma, depends on the four space-time coordinates. Since a non-relativistic description is pursued spatial and temporal variable are treated separately. In a tokamak the plasma is, in general, shaped in axial-symmetric topological solid torus, stratified as discussed in 1. The magnetic field lines wraps around toroidal surfaces called magnetic surfaces, one of them represented in figure 1. This surfaces allow to define a local right-handed reference system [y,x,z] describing the whole space. x is the flux coordinate, perpendicular everywhere to magnetic surfaces, z is the toroidal direction and y is the poloidal[1] one.

[1]The poloidal direction is that which follows the minor circumference of the torus and therefore passes through the central hole, the toroidal direction is that which follows the major circumference.

The (x,y) plane is said poloidal plane. Another reference system will come in handy in the linear analysis, the right-handed cylindrical system [R, Φ, Z], describing respectively the radial, angular and vertical directions.

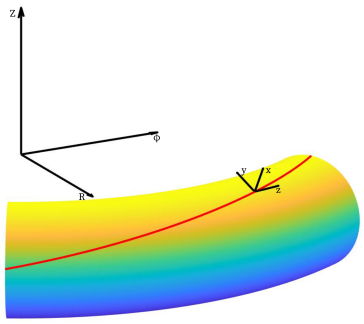

Figure 1: Portion of a magnetic sourface with a magnetic field line (red line) wrapping around it. The two reference systems [y,x,z] and [R,Φ,Z] are highlighted.

2.2. Ballooning Mode

Ballooning mode is one of the principal instabilities present in edge and SOL layer. It is driven by the bad curvature region, i.e. a region where density gradient and curvature points toward opposite directions: $\vec{\kappa}\nabla n < 0$. The mode is made unstable by the presence of plasma collisions, which can be represented by not null resistivity ν in the model. This branch is called Resistive Ballooning Mode (RBM). A more complete treatment can be found in [2].

3. The Linear Solver

It is first necessary to linearise the set of GBS equations using a first-order perturbative method. In linear approximation, the work is carried in the condition $\varepsilon = \frac{a}{R} \to 0$, said infinite aspect ratio, a and R being the minor and major radius of the tokamak torus. It was assumed that each field f^* described in 2, was describable as the sum of an equilibrium field f_0 plus a perturbation f, such that $f \ll f_0$: $f^* = f_0 + f$. It is assumed that the equilibrium for n and T_e can be expressed as $f_0 = f_{00}(1 + x/L_f)$, f_{00} being a scalar, and it is null for the other fields ϕ, ψ, $V_{\parallel,i}$. T_i is neglected since the linear analysis has been carried in the hypothesis $T_i \ll T_e$, or $\tau \sim 0$, said

cold ion approximation. According to non-local, linear theories on curvature driven modes, the turbulence in radial direction develops less than in poloidal one [2]. Therefore the x-direction is negligible and consequently the analysis develops on a single magnetic surface.
With this in mind, it is possible to simplify the operators introduced in 2 to:

$$\hat{C} = \frac{b_Z(y)}{b_y(y)}\partial_y \tag{1}$$
$$\nabla_\perp^2 = \partial_y^2 \tag{2}$$
$$\nabla_\parallel = \frac{1}{R}b_y(y)\partial_y + \partial_z \tag{3}$$

Here, b_j is the component of $\vec{b}$ in j-th direction. It is adopted the dependence of any perturbation f as:

$$f(y,z,t) = f(y)e^{\tilde{\gamma}t - in_z z} \tag{4}$$

Here i is the immaginary unit. In this way it is possible to perform the analysis of each individual modes in z, described by wave number n_z, justified by the superposition principle for linear systems. It is not possible to follow the same procedure for the y direction because of the y-dependant coefficient in geometrical operators. Finally, since $\tilde{\gamma} = \gamma + i\omega \in \mathcal{C}$, because of the properties of complex numbers, $\gamma = \Re(\tilde{\gamma})$, called growth rate, describes the exponential growth of the perturbation, $\omega = \Im(\tilde{\gamma})$ describes the oscillatory behaviour of the mode.
From eq. 4 it is possible to retrieve a simplified version of eq. 3.

$$\nabla_\parallel = \frac{1}{R}b_y(y)\partial_y - in_Z \tag{5}$$

The retrieved eigenvalue problem for the y dependence is

$$\tilde{\gamma}n = \frac{R}{L_n}\partial_y\phi + 2\hat{C}(T_e + n - \phi) - \nabla_\perp V_{\parallel,e} \tag{6a}$$
$$\tilde{\gamma}\nabla_\perp^2\phi = 2\hat{C}(T_e + n) + \nabla_\parallel(V_{\parallel,i} - V_{\parallel,e}) \tag{6b}$$
$$\tilde{\gamma}\left(\frac{m_e}{m_i}V_{\parallel,e} + \frac{\beta}{2}\psi\right) = \nu(V_{\parallel,i} - V_{\parallel,e}) \nabla_\perp(\phi - n - 1.71T_e) \tag{6c}$$
$$\tilde{\gamma}V_{\parallel,i} = -\nabla_\parallel(n + T_e) \tag{6d}$$
$$\tilde{\gamma}T_e = \eta\frac{R}{L_n}\partial_y\phi + \frac{4}{3}\hat{C}(\frac{7}{2}T_e + n - \phi) + \frac{2}{3}\nabla_\parallel(0.71V_{\parallel,i} - 1.71V_{\parallel,e}) \tag{6e}$$

If we assume that we have an evenly spaced grid points discretizing the y-direction we can address this problem numerically. By defining a vector $\vec{x}$ as the collection of values that the various fields take on the grid points and replacing the differential operators with matrices that approximate them through finite differences it is possible to lead to the symbolic problem:

$$\tilde{\gamma}L\vec{x} = M\vec{x} \tag{7}$$

Here, L and M are the two matrices collecting all the finite difference approximations. Solving for the generalised eigenvalue of M with respect to L it is possible to find the growth rate as the eigenvalue with maximum real part.

3.1. Field Lines Discretisation

It has been assumed the existence of a grid discretizing the y direction, and therefore the magnetic surface poloidal cross section. To handle efficiently the discretisation it is firstly assumed that the current flowing in the plasma presents a gaussian distribution $I_p = e^{-(R^2+Z^2)/(2a_g^2)}$. Dedicated coils for plasma shaping, instead, are modeled as current filaments, i.e., concentrated at a single point (R_j, Z_j). Their current intensity I_j is given relative to that passing through the plasma.
From theory it is known that magnetic surfaces are characterised by a constant flux function Ψ, related to the poloidal magnetic field through the dimensional equation

$$\vec{B}_p = \frac{1}{R}\nabla\Psi \times \vec{e}_\phi \tag{8}$$

Here $\vec{e}_\phi$ is the ϕ direction versor. To be able to write an analytical dependence of Ψ in the (R,Z) plane the coils are confounded with infinitely long straight filaments. This is justified by the infinite aspect ratio we are working in. Is therefore possible to express Ψ as:

$$\Psi = \frac{A}{2}\left[\log(R^2+Z^2) + \mathrm{Ei}(\frac{R^2+Z^2}{2a_g^2})\right] + \frac{A}{2}\sum_{j=1}^{N} I_j \log((R-R_j)^2 + (Z-Z_j)^2) \tag{9}$$

In eq. 9, A is a coefficient proportional to the plasma current.From that the implicit equation $\Psi(R,Z) = \Psi_0$ allows to retrieve numerically the magnetic surface's cross section coordinates. From that the curve can be discretized in N_y equally spaced points and two array containing each grid points' coordinates. The magnetic field on the grid points $b_Z(y_i)$, $b_R(y_i)$ and

$b_y(y_i) = \sqrt{b_Z^2 + b_R^2}$ can be evaluated analytically, with Biot-Savart like solutions.

3.2. Magnetic configurations

In this work four magnetic configuration has been used.

- *Circular* (C): Magnetic poloidal cross sections are circular.
- *Global Symmetric (GS)*: A coil it is used to confer elongation in the lower part of the configuration, conferring the shape of a reversed drop. In the lower part the magnetic field is weaker and therefore the safety factor $q \propto \frac{dz}{dy} \propto \frac{1}{b_y}$ can reach high values. Therefore, magnetic lines stay at the bottom of the configuration longer than at the top.
- *Global Positive* (GP): Three coils are arranged asymmetrically to confer positive triangularity, i.e. the cross section assume a D shape that points toward the Low Field Side (LFS). q behaves similarly to GS.
- *Global Negative* (GN): This configuration is obtained from GP through a symmetry in the poloidal plane with respect a vertical axis intersecting the magnetic one. In this case, therefore, the D shape points towards the High Field Side (HFS).

4. Linear GBS Results

4.1. Resistive Ballooning Mode

The set 6 is not analytically soluble, neither if the it simplified in order to describe RBM only. To solve this issue a local analysis is pursuit into the most unstable point in a circular geometry, i.e. the point where $b_R(y) = 0$ and $b_Z(y) > 0$, where the coefficient of the curvature 1 is maximum. Eq. 10 is retrieved:

$$\left(\tilde{\gamma}^2 + \frac{1}{\nu}\left(\frac{k_\parallel}{k_y}\right)^2 \tilde{\gamma} - (\gamma_{id}^{RBM})^2\right)\phi = 0 \quad (10)$$

being k_y the y-wave-vector, characterising the y-eigensolution, and $k_\parallel = R(b_y k_y - k_z)$, $k_z = \frac{n_z}{R}$, and $\gamma_{id}^{RBM} = \sqrt{2(1+\eta)R/L_n}$ the eigenvalue it would be retrieved if the parallel electron velocity would be neglected. To maximise the result of eq. 10 it is needed that $k_z \simeq b_y k_y$, the "$\simeq$" relation due to the discrete set of values k_z and k_y can assume. This corresponds to what is retrieved from simulations in C geometry. For what concerns the others, linearity is found, but with a reduced coefficient,even less pronounced in GP. This behaviour can be attributed to the increase of length in a shaped curve.

	C	GS	GP	GN
$(k_y/k_z)_{avg}$	15.1	7.6	10.4	11.6
$\overline{b_y}(k_y/k_z)_{avg}$	1.03	0.73	0.80	0.88

Table 1: Proportionality between the evaluated k_y for every k_z. In the second line the value is multiplied by the average b_y along the curve.

In addition, circular geometry was used to successfully perform a linear code validation process on previous literature [2].

Shaped configurations' growth rate $\gamma = \Re(\tilde{\gamma})$ is summed up in figure 2. In all the three geometries it is a monotonically increasing function always smaller than γ_{id}^{RBM}, and sharply decreasing for small values of k_y. This is due to the fact that in the presence of shaping the perturbation is localized in the Low Field Size (LFS), also for low values of n_Z, where it is made unstable, increasing its growth rate. Moreover the retrieved y dependencies shows the maximum of the perturbation lowest region, where the q increase and the field line wrap less around the surface.

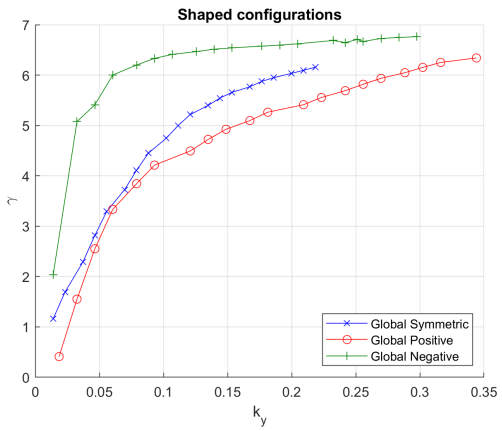

Figure 2: Dispersion relation for RBM simulation in GS, GP, GN, configurations

Results in fig. 2 suggest also that negative triangularity is detrimental to the stability of the system since γ is increased with respect to other

configurations, particularly for the modes with low k_y. Positive triangularity, instead seems to be slightly advantageous for stability, and takes place on higher k_y.

4.2. Full case

In the full frame eq. 6 are tackled without any simplifications, allowing to picture the whole complexity but loosing on analytical manageability.
Also in this case the proportionality between k_y and k_z is respected in circular shape with the same coefficient than in table 2. In the other configurations the proportionality is less strict. Anyway, also in this case k_y is increased for the GP and GN configuration with respect GS.
The growth rate is pictured in figure 3. While the main features are kept unchanged some important differences deserve to be observed. As in 4.1 negative triangularity configuration is appraised as the most unstable, the maximum growth rate being in the same range. In full picture, also GP is unfavourable with respect GS, with its curve crossing GN curve at high k_y.

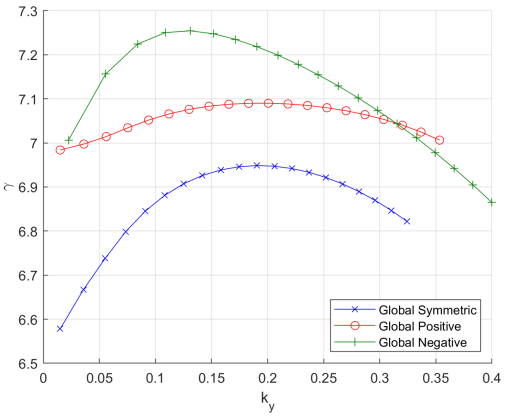

Figure 3: Dispersion relation for RBM simulation in GS, GP, GN, configurations

Differently on the RBM case, the full simulation pictures a not null behaviour in the small k_y, atypical for Ballooning Mode regime. Therefore, something else other than such must intervene.

4.3. Lp Evaluation

Pressure gradient length L_p in the edge region allows to comprehend how effectively the plasma is confined. High values of L_p are symptoms of mild gradients and loose confinements. In the present work it was evaluated firstly through the linear solver's results, through a non-local theory called gradient removal [3] where the turbulence saturation causes a flattening of the pressure profile and therefore the disappearance of the turbulence's drive.

$$L_p = \frac{q}{c_s}\left(\frac{\gamma}{k_y}\right)_{max} \tag{11}$$

Eq. 11 is a non-linear one and it needs to be solved numerically, scanning through various values of L_p and n_Z and linearly interpolating to find the solution. Also to remove the y-dependence on q it has been chosen to use the q at LFS mid plane.

		GS	GP	GN
L_p $\nu = 0.1$ **linear**	$[\rho_s]$	42.4	34.9	52.0

Table 2: Pressure length evaluated in different geometries.

The linear code evaluates as positive the effect of GP leading to a steeper gradient. The GN configuration, instead, is largely detrimental also in this case. However all the three evaluated pressure gradients lengths are in the order of the edge thickness, suggesting very poor confinement properties. What is found agrees with Riva's results [3], in an elongation-less configurations.

5. Nonlinear GBS Results

Two sets of nonlinear simulations have been carried for each shape through nonlinear GBS code. The two sets differ for the different value of resistivity, $\nu = 0.1$ and $\nu = 0.3$. Simulation have been run until convergence of the average value of each field. Emerging data have been averaged on time and on the toroidal angle. The radial dependence is extrapolated for the LFS outer-midplane. An exponential fit is performed for density and temperature field, to capture a first approximation of their gradient length according to the equation $f(x) \propto e^{(-x/L_n)}$. Pressure gradient length is retrieved through

$$\frac{1}{L_p} = \frac{1}{L_n} + \frac{1}{L_{T_e}} \tag{12}$$

Results are reported in table 3.

	ν	GS	GP	GN
L_p $[\rho_s]$ **n-linear**	0.1	17.5	24.8	15.2
L_p $[\rho_s]$ **n-linear**	0.3	19.7	36.9	18.4
L_p $[\rho_s]$ **linear**	0.1	42.4	34.9	59

Table 3: Pressure length evaluated in different geometries, and models.

Positive triangularity presents the worse confinement properties, exhibiting higher pressure gradient length. Negative one, on the contrary, seems the most suitable to confine plasma. The effect of the resistivity is to increase transport properties, causing milder gradients. This effect is particularly evident for positive triangularity. Non linear result are completely in disagree with the ones reported in 4.3. This can be partially attributed to the simplifications in the linearisation process. Also, a finite aspect ratio has been considered, leading to stabilising effect. These results, in fact, agree with the one found in literature [3], where it emerges that negative triangularity has the best confinement properties.

6. Conclusions and Outlooks

Understanding plasma turbulence in the tokamak edge is of fundamental importance since it regulates the overall performance of a tokamak, it controls the heat exhaust to the wall, the core confinements features and the transport properties of the plasma.
In this work, firstly a linear method has been presented. Successively, the triangularity role in RBM branch has been investigated in a linear frame, leading to the evidence that negative triangularity is essentially detrimental for the system, the pressure gradient has been evaluated with a linear and linear-based solved. Finally the confinement properties have been analysed also through non-linear simulations.
Nonlinear, most reliable, data portray negative triangularity as advantageous for the stability of the magnetic configuration. Plasma confinement capabilities were found to be better when negative triangularity shaping is imposed. In any case, this is not unequivocally found in both discussions and therefore a deeper analysis is necessary.
The discordance between the linear analysis, the non linear one and that reported in [3] leads to questioning the validity of the results, in particular the linear ones. The succeeding of linear simulations in the circular benchmark suggests problems in the linear solver dealing with shaped configurations. Since only the geometric operators change between the two cases, this gives clear clues as to where the problem may be.
Nevertheless, only three particular configurations and a single set of parameters were analysed. The analysis is therefore limited and different shaping of plasma conditions might lead to different results.
Future extensions of the present work can be found mainly in an extended analysis of different magnetic configurations and plasma parameters. Furthermore, it has been reported in previous literature that the aspect ratio and the Shafranov shift are stabilising parameters [3]. The inclusion of these variables, excluded in this work, may lead to results more in agreement with current literature.
In addition, a more thorough analysis of the geometric operators is desirable, especially with regard to their well-posedness. Such work has been initiated in the course of this thesis and there is evidence pointing to problems in the parallel gradient. Finally, extension to other branches of instability could lead to a more complete understanding of the phenomena involved, particularly when integrated with the Scrape Off Layer study. In that case, the linear solver should be modified to deal also with open surfaces, and the edge conditions should be discussed.

References

[1] P. Ricci M. Giacomin. Investigation of turbulent transport regimes in the tokamak edge by using two-fluid simulations. *Journal of Plasma Physics*, 86, 2020.

[2] Annamaria Mosetto. *Turbolent regimes in the tokamak scrape-off layer*. PhD thesis, Faculté des sciences de base, EPFL, Lausanne, Switzerland, 2014.

[3] F. Riva. *Verification and validation procedures with applications to plasma-edge turbulence simulations*. PhD thesis, Faculté des sciences de base, EPFL, Lausanne, Switzerland, 2019.

POLITECNICO
MILANO 1863

SCUOLA DI INGEGNERIA INDUSTRIALE
E DELL'INFORMAZIONE

"Effect of plasma triangularity on turbulent transport in the tokamak boundary"

Tesi di Laurea Magistrale in
Nuclear Engineering - Ingegneria Nucleare

Author: **Riccardo Saura**

Student ID: 943298
Advisor: Prof. Matteo Passoni
Co-advisors: Prof. Paolo Ricci, Maurizio Giacomin
Academic Year: 2020-21

Abstract

Plasma dynamics in the boundary of magnetic fusion devices plays a key role on the overall confinement properties.
The tokamak boundary description is intrinsically nonlinear and characterised by a wide range of spatial and temporal scale and it is patterned after a complex magnetic geometry that guarantees good confinement in the core region, while mitigating the heat flux to the wall. The moulding of the plasma in "D" shapes, commonly said triangularity, allows to deeply influence stability and transport properties, granting more steady confinement configuration characterised by lower turbulent fluctuation. In the present thesis the turbulence in the tokamak boundary is studied with a two-fluid Braginiskii model. The focus is firstly on a linear analysis, allowing to determine the dominant instabilities' growth rate and the confinement properties.
Therefore, a nonlinear, preliminary, study it has been carried out through the GBS code

Keywords: plasma physics, plasma confinement, triangularity, plasma turbulence simulation, GBS code, pressure gradient length

Abstract in lingua italiana

La dinamica di un plasma al bordo di macchine per la fusione a confinamento magnetico, gioca un ruolo chiave nella determinazione delle proprietà globali di confinamento.
La descrizione dei limiti esterni di un tokamak è intrinsecamente non lineare e caratterizzata da scale spaziali e temporali molto ampie e si basa su una geometria magnetica complessa che garantisce un buon confinamento nella regione di core e limita gli effetti del flusso di calore sulle pareti della macchina. Modellare il plasma in forme a "D", comunemente dette configurazioni con triangolarità, permette di influenzare profondamente le proprietà di stabilità e trasporto, garantendo un confinamento più stabile nel tempo e caratterizzato da basse fluttuazioni dovute alla turbolenza.
Nella presente tesi la turbolenza nel bordo di un tokamak è analizzata con un modello a due fluidi di tipo Braginiskii. Il lavoro si focalizzerà in primo luogo su una analisi lineare, permettendo di determinare la velocità di crescita delle instabilità dominanti e le proprietà di confinamento.
Quindi, uno studio preliminare non lineare è compito attraverso il codice GBS.

Parole chiave: fisica dei plasmi, confinamento magnetico dei plasmi, triangolarità, simulazione della turbolenza nei plasmi, codice GBS, lunghezza di equilibrio della pressione

Contents

1 | Introduction

In this chapter it is provided a brief overview on nuclear fusion and machines used to perform it.
The energetic problem (§ 1.1) is firstly addressed with the aim to better appreciate the impact the nuclear fusion promise to have in such an environment.
Right after, the physical fundamentals of such a technique are sifted through (§ 1.2) with a special eye for the suitable reactions (§ 1.2.1), the Lawson Criterion (§ 1.2.2) and the plasma state (§ 1.2.3). Plasma confinement techniques are also discussed (§ 1.2.4).
In a second moment the machine used for nuclear fusion is analysed (§ 1.3) focusing on the different regions that compose the plasma (§ 1.3.1).
Then, in a further section plasma shaping is addressed (§ 1.4), tackling the periphery dynamics (§ 1.4.1) and triangularity (§ 1.4.2).
Once detailed all the previous themes the discussion will by nature close on the definition of the goal and the motivation behind this thesis work (§ 1.5)
The results of the present thesis extend the previous work of [25], carried out in limited geometry, to more complex magnetic configurations that include a null of the poloidal magnetic field, and of [34] implementing a different approach.

1.1. International Energy production and consumption

In the last four centuries the western countries have developed a lifestyle based on the heavy labour proxy to machines able to perform increasingly complicated tasks relatively promptly and accurately. Rapidly this costume spread all around the globe affecting every nation lifestyle. As a matter of fact, then, each country needs nowadays energy to power up everyday life, industries and human activities in general.
It is well agreed that the wellness in a society's lifestyle is directly proportional to the energy consumption of the country it belongs to, especially in the developing phase of the state [6], this last observation excepted only by last decades energy consumption history in highly developed countries because of the relatively recent tendency to consumption

efficiency [16]. An increase of global primary source in the next century is then forecast on the basis of the actual socio-political assets and the way to produce that energy is an issue that has to be assessed in the present.
The energetic problem, as worldwide and intimately connected with human life, is a convoluted and multifaceted problem with difficult resolution, with a widespread fallout as on society, environment and economy.

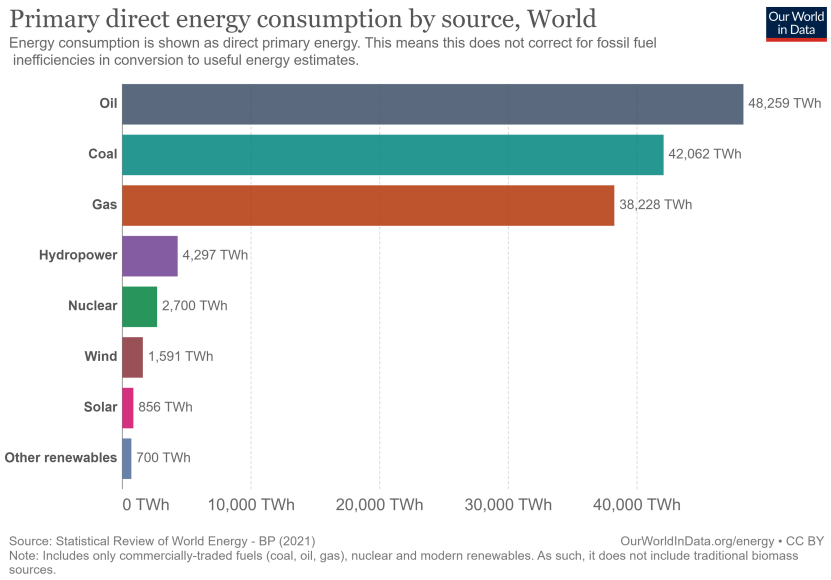

Figure 1.1: World primary direct energy consumption by source in 2020. [26]

Despite the increasing need, energy comes with a cost. The actual primary source mix is based on fossil fuel such as oil, natural gas and coal, (figure 1.1) which combustion releases a huge amount of CO_2, pollutant and greenhouse gasses in the atmosphere, representing an important threat for the environment. Also, gas and oil are not diffused sources, resulting in few countries that control the greatest part of their production, e.g. Europe produces only about 10% of the gas it consumes. Fossil fuel needs confer an important international political power to oil and gas producers, leading to critical tensions such as the Iranian crisis in 1946 or Russia-Ukraine political crisis in 2006-2014. Because all of this reasons such an important source presents a highly unstable price (figure 1.2) impacting adversely on the energy security of any population.

It is then crucial for many extents to exit from the oil's centrality in energy production and some alternatives have been taken into action as renewable energy source and nuclear fission energy. Despite the last being somehow diffused at worldwide scale and producing

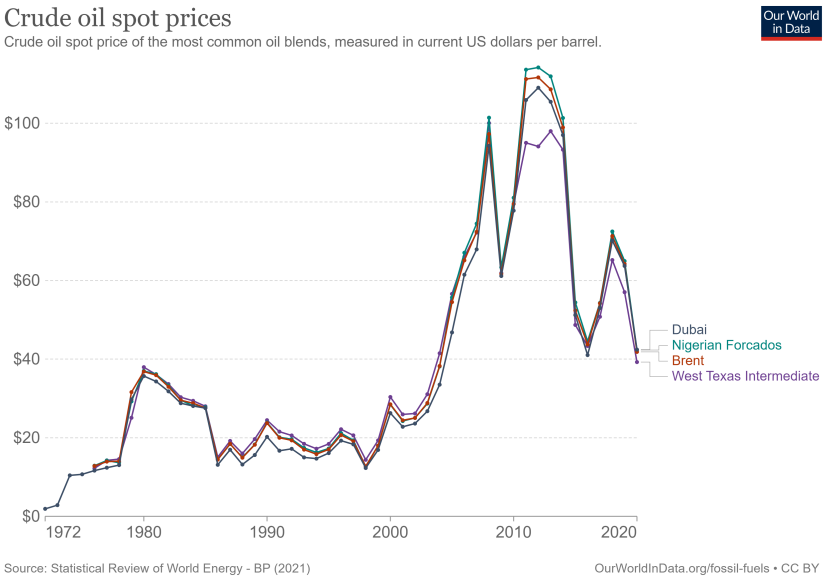

Figure 1.2: Crude oil spot price of the most common oil blends, measured in current US dollars per barrel. [27]

a great amount of energy it is quite controversial among some populations causing the shutdown of various facilities as in California in 2020. Some more welcome nuclear sources, the nuclear fusion techniques, have been under study for many years.

1.2. Energy Production by Nuclear Fusion

Nuclear fusion is the physical process that lights up stars. The basic is based on the difference in binding energy between the reactants and the products in some nuclear reaction. The binding energy is the energy due to the force that keeps together the protons and neutrons in nuclei, called strong force and being much stronger and short ranged then electromagnetic force. The great magnitude of this force causes a huge difference in mass along the reaction. The mass defect is then converted in kinetic energy for the products, and it is quantified according to the notorious Einstein equation

$$E = (m_i - m_f)c^2 \tag{1.1}$$

with m_i and m_f respectively the initial and the final total mass of the matter involved in the reaction. If it occurs that $m_i > m_f$ the reaction is said to be exothermic and some energy is conferred to the products.

1.2.1. Nuclear Fusion Reactions

In fusion reactions light nuclei fuse together to form a heavier and stabler product. As a matter of principle every reactant leading to a nucleus lighter than Fe^{56} will release energy. Anyway, lighter nuclei are a better and more common choice.

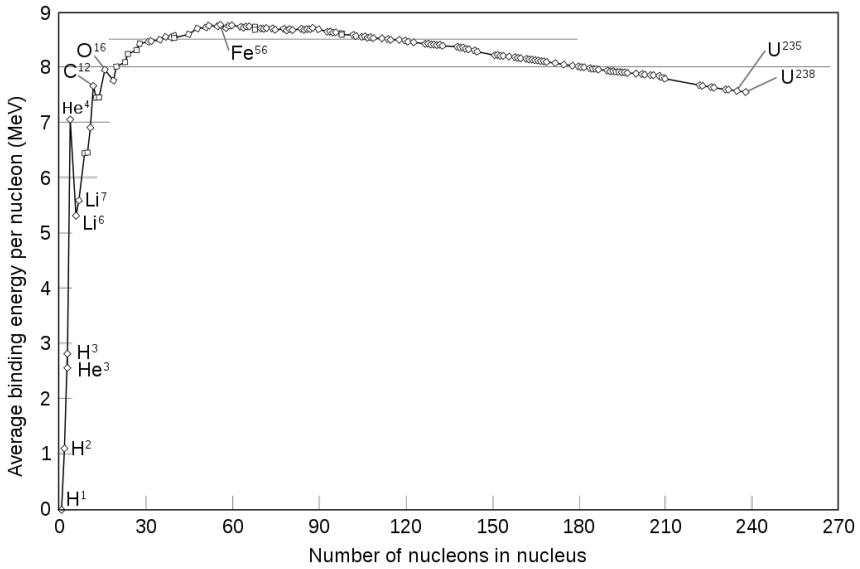

Figure 1.3: Binding energy per nucleon against number of nucleons.

Firstly, as clearly shown by figure 1.3, as long as $A < 4$, the binding energy is characterised by sharp increases per each nucleon added to the nucleus, leading to a higher energy release. This behaviour peaks with the He_2^4, a double magic nucleus, with both, protons and neutrons', energetic levels completed, leading to a particularly stable structure. There are then many possible fusion reactions, the most common of which are summarised in table 1.1.

Reaction			Branch	E_f [MeV]
$D + D$	$\longrightarrow$	$He^3 + n$	50%	3.27
	$\longrightarrow$	$T + H$	50%	4.03
$D + He^3$	$\longrightarrow$	$He^4 + H$	100%	18.3
$D + T$	$\longrightarrow$	$He^4 + n$	100%	17.6

Table 1.1: Different fusion reaction having as reactants D, T, He^3

The first important figure of merit is explicit in the table 1.1. As it was possible to anticipate the highest yields refer to reactions that have He^4 in the products, due to its high stability. Such reactions then would be possibly preferred.

A second reason to use light nuclei is due to the process' dynamic. To describe the characteristic of the process in which two particles collide, said scattering, an important parameter, the cross section σ, comes in handy. This concept is a very general one, applicable to a great variety of phenomena, from scattering to fiscal reactions. It emerges in the hypothesis that a spatially homogeneous, temporally constant, monochromatic and well collimated beam of particle impinges on an ideal target, thin enough not to make the flux varies significantly during the reactions. The cross section, though, represents the proportionality that can be found between the reaction rate R and the incoming particle flux and it is associated with the likelihood that a reaction takes place.

$$R = \sigma v n \tag{1.2}$$

In general the cross section can depend on various reaction parameters as the energy of the incoming particles or the scattering angle. A well-known result is the Rutherford cross section [22], describing the scattering in a classical theory frame between two particles, in the target reference system, provided the force they interchange has a potential in the form $\mathrm{U} = \frac{\alpha}{r}$. In case of the Coulomb force between two nuclei $\alpha = A_1 A_2 e^2$ where A_i is the nucleus mass number and e is the unitary charge. The differential cross section with respect the deflection angle χ is

$$\frac{d\sigma_C}{d\chi} = \pi \left(\frac{\alpha}{m v_\infty^2} \right)^2 \frac{\cos(\chi/2)}{\sin^3(\chi/2)} \tag{1.3}$$

where $m = \left(\frac{1}{m_1} + \frac{1}{m_2} \right)^{-1}$ is the reduced mass of the system, $m_i = A_i m_u$, m_u being the mass corresponding to 1 atomic mass and v_∞ the velocity of the impinging particle at infinity. From energy conservation the minimum distance $\rho_{\min}$ they can reach is

$$\rho_{\min} = \frac{2\alpha}{m v_\infty^2} = (A_1 + A_2) \frac{2e^2}{m_u v_\infty^2} \tag{1.4}$$

Therefore two nuclei will interact more strongly as the sum of their atomic mass number increases and consequently they will be able to get less close. To allow two nuclei to merge, instead, it is desirable they come as near as possible so that nuclear interaction, which has a finite and short range, can overcome Coulomb repulsion. From 1.4, for every couple of ions it is possible to get them arbitrarily close, provided enough initial energy is supplied. It is advisable, however, to have to confer the minor amount of it, either in the form of ordered beam velocity than as disordered thermal energy. Lighter nuclei, then, suffer lower Coulomb repulsion and have a smaller potential barrier to overcome. It must

be said, however that quantum effects as tunnelling intervene and therefore the reaction is possible also when it would classically forbidden, i.e. when $\rho_{\min} > \rho_{snf}$, ρ_{snf} being the strong nuclear force range. To take in account also this effect it is usually employed the Gamow cross section [18]:

$$\sigma_G(E) = \frac{1}{E} f(E) e^{-\sqrt{\frac{E_G}{E}}} \tag{1.5}$$

where E is the kinetic energy at the beginning of the reaction, E_G is the Gamow energy, which scales as the square of the mass numbers, and $f(E)$ is a slowly varying factor. This, globally, results in a higher probability that the two nuclei will fuse together and consequently they will display a steeper fusion frequency other condition being equal.
Volumetric reaction rate is important feature that must be considered in order to choose the most suitable redaction. It is the expressed by the relation

$$R_{ij} = n_i n_j < \sigma v_r >_E \tag{1.6}$$

with n_α the numeric density [1] of the α-th population, and $< \sigma v_r >_E$ the averaged cross section on the relative velocity distribution between the two population. The reaction rate is an important parameter because it is connected with the volumetric power trough

$$p_f''' = R_f E_f \tag{1.7}$$

Where R_f is the reaction rate of the fusion reaction and E_f is the energy released by this last. The interest will be therefore to chose the reaction that maximise this last. Assuming a Boltzmann distribution of the particle along the energy, cross section and then $< \sigma v_r >_E$ depends only on species temperatures, assumed to be equal for the current evaluation.

From table 1.1 and figure 1.4 it is manifest that the best reaction to work with will be D-T reaction, with the reactants at a temperature of tens of keV to maximise the reaction rate. Incidentally, this is an order of magnitude higher than the Sun's core. It is worth to remark that since in the mixture there is deuterium, D-D reaction will occur as well but with a frequency some order of magnitude lower. Then, and also due to the lower energy yield, the last reaction is negligible.

1.2.2. Lawson Criterion

The products of D-T reaction are well suited for the application we are looking at. By a simple physical observation deriving from momentum and energy conservation, it is

[1] since now we will address the numeric density as density

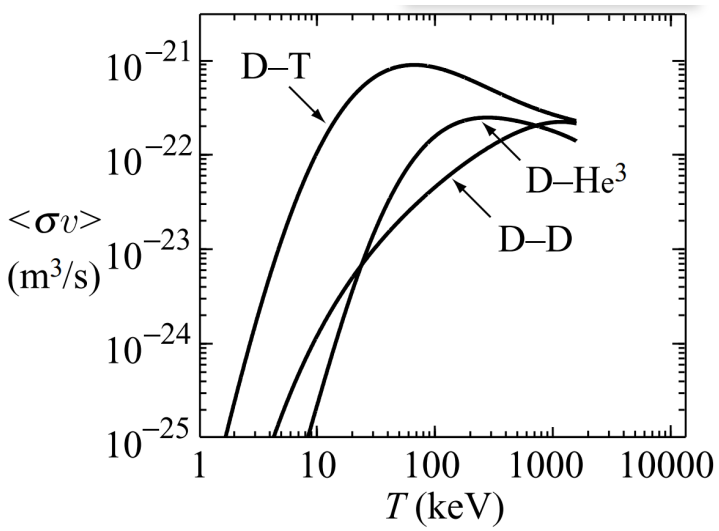

Figure 1.4: $\langle \sigma v_r \rangle$ as a function of T for commonest fusion reactions. [11].

possible to infer that the energy will be shared between helium nucleus and the neutron in the ratio of the inverse of the masses, roughly 1:4. Immediately after the fusion reaction, helium carries 3.5 MeV of kinetic energy, being much energetic than the surrounding particles, but as a heavy charged particle it interacts with them, losing his momentum and contributing to heat the plasma up. This mechanism plays a crucial role in maintaining stable plasma conditions during the time fusions take place[2] balancing the unavoidable losses that will be present. A way to measure the losses is provided by the confinement time, defined as

$$\tau_E = \frac{W}{P_{loss}} \tag{1.8}$$

where $W = \sum_a \int_D n_a T_a$ is the thermal energy of the whole system. The other reaction product, the neutron, instead, carry the most of energy, 14 MeV. Since the neutron is a chargeless particle and the surrounding matter is, in the applications, loose or very thin, it is able to escape. If a moderating material[3] is placed near the plasma it is possible to use the neutron to extract heat from the reaction and use it for electric energy production. It must be underlined that an important neutron field will have some consequences on structural materials, causing a volumetric heat source inside them - the phenomena is called γ-heating -, swelling, embrittlement and structural problems in general [37]. These

[2]It is a quite different time depending on the techniques used. As discussed in this subsection, the aim in magnetic confined fusion is to reach a stable continuous regime despite inertial confinement works on the repetition of short shots because of the intrinsic way they are projected.

[3]A moderating material, or moderator, is a material composed, at least partially, by light nuclei able to scatter neutrons. From energy and momentum conservation neutron loses part of its energy. The energy gained by the collided nucleus is transformed into heat by phononic interactions. Typical moderator materials are hydrogen (H), boron (B), lithium (Li) and carbon (C).

phenomena are very severe due to the neutrons' high energy - actual fast reactor cope with up to 5 MeV neutrons - and lead to a still open issue. Moreover wherever there is a neutronic field some atoms will be activated leading to radioactive material to dispose at the facility's end of life (EOF). With the right material choices, anyway, it is possible to reduce waste half-lives to some dozens of year achieving a remarkable result since activated material would be the only radioactive waste of the process, as nuclear ashes (He^4) are stable.

To reach ignition, the condition in which fusion can self-sustain, it must hold that

$$R_f E_{f,\alpha} \geq P_{loss} \tag{1.9}$$

Assuming a plasma composed by Deuterium and Tritium ions and electrons, sharing the same density and temperature roughly and distributed on a Maxwell-Boltzmann distribution on energy [43] it is possible to show that the ignition condition 1.9 is equivalent to the Lawson criterion

$$\tau_E nT > 5 \cdot 10^{21} s m^{-3} keV \tag{1.10}$$

Since from figure 1.4 the temperature is settled as $T \sim 10keV$ this reduces to the condition

$$\tau_C n > 10^{20} s m^{-3} \tag{1.11}$$

Nuclear reactions take place in stars due to very high gravitational force that cannot be achieved on Earth. [3]. The two main solution proposed by modern technology are the inertial confinement and the magnetic one. The first consist in shining a small spherical pellet of D-T fuel trough a high intensity laser pulse. The particle inertia is exploited to increase the density in the very centre of the fuel, because of the inward momentum transferred by the electromagnetic radiation. This kind of technique has a very short confinement time ($\tau_E \sim 10^{-9} s$) requesting very high densities ($n \sim 10^{30} m^{-3}$). On the other hand, magnetic confinement uses strong magnetic fields to confine the plasma at a considerably lower density ($n \sim 10^{20} m^{-3}$)[4]. This is allowed by the much higher confinement time that such a design can guarantee ($\tau_E \sim 1s$).

[4]For reference, the air density at room temperature is in the order of $n_{air} \sim 10^{25} m^{-3}$

1.2.3. The Macroscopic State of Plasma

The stiff temperatures evaluated in the last paragraph have heavy consequences on the sate of matter the nuclear fuel is found in. Such energies are much higher than the one needed to ionise matter - the ionisation potential are in the order of tens of eV [30]. This will cause the nuclear fuel to behave as a plasma.
The plasma state, commonly known as the fourth state of matter, is a macroscopically neutral gas composed by charged particles. Those particles, unlike in a gas, will interact both by short range interaction, e.g. scattering, and by long range electromagnetic interaction through electric and magnetic field. The region in which the charged nature of particles plays a role is called Debby region, a sphere of radius $\lambda_D = \sqrt{\frac{T}{4\pi e^2 n}}$. Each particle will interact only with particles within the Debby radius, out of this region it is said to be shielded. The magnitude of this parameter has a great variability and depends on the thermodynamic state of the plasma. It usually goes from really small values as $7 \cdot 10^{-7} cm$ in laser plasma up to meters in interstellar gases [15]. For reference, thermonuclear plasma are characterised by a Debye length in the order of $2 \cdot 10^{-3}$ cm
Electromagnetic forces then play a crucial role in plasma dynamic giving rise to collective motion and determining the kind of wave the matter can sustain. On the other hand, the ionised matter will influence the electromagnetic fields through charges and currents. It is not possible then to split the treatment of matter and electromagnetic fields when it comes up to plasma, but a self-consistent integral description must be taken into account. Such a description will be further analysed in chapter 2.

1.2.4. Plasma Confinement Principles

The motion of a charged particle in a constant and uniform magnetic field $\vec{B}$ is a well know result [20]. The particle, due to the Lorentz force keep being confined in the direction perpendicular to the magnetic field in a circular uniform motion, characterised by the gyro-frequency Ω_L and the Larmor radius ρ_L

$$\Omega_L = \frac{qB}{mc} \qquad \rho_L = \frac{v_\perp}{\Omega_L} \tag{1.12}$$

where q is the charge of the particle, m its mass, B the magnetic field magnitude, c the speed of light and $v_\perp$ the perpendicular velocity. Instead, on the magnetic field direction the particle is free to move, resulting in a spiral unbounded motion. As a first approximation, in presence of a static magnetic field, characterised by gradients much higher than the inverse of the Larmor radius, the particle streams along a magnetic field

line in a helical trajectory. This approximation is called guiding centre approximation [29]. To confine a particle in a closed region, then, some more efforts are needed.

By a balance of force is it possible to find the condition needed to ensure equilibrium [11]

$$\vec{J} \times \vec{B} = \nabla p \tag{1.13}$$

where $\vec{J}$ is the plasma current. It holds that

$$\nabla \times \vec{B} = \frac{4\pi}{c} \vec{J} \tag{1.14}$$

in a magneto-static picture, and p is the plasma picture. The balance equation 1.13 derive from the magnetohydrodynamic motion equation in the steady state limit without flows. Such equation can be derived with some work starting from the equations in 2.1. Equation 1.13 allows to find the plasma current necessary to magnetically confine a plasma with finite pressure. It is important to point out that $\vec{J}$ include the plasma current, that means that at least part of the magnetic field needed to confine the plasma is created by the plasma itself. This lead to some instabilities, some of it analysed in the following.
Manipulating equation 1.13 it is easy to show that both the vectors $\vec{B}$ and $\vec{J}$ lay on surfaces of constant pressure, called magnetic surfaces, as $\vec{B} \cdot \nabla p = \vec{J} \cdot \nabla p = 0$. This, according to the Poincaré's theorem, stating that a compact surface which is everywhere tangential to a non-vanishing vector field free of singularities must have the topology of a torus [14], clearly define the shape of the isobaric surfaces. The two fields will then wrap around the torus.
For sake of completeness, it must be said that there is a way to confine particles also without a compact surface. A linear machine, as a matter of fact, it works with open cylinders, that in practical scenarios ends with some physical walls. Here particles are confined by magnetic mirrors, i.e. a non-constant magnetic field with a higher field at the two end of the machine. If the gradient is steep enough and the initial velocity satisfies some condition, the particle is not able to reach the ending wall and it is reflected toward the centre. Such kind of machines are thought not for an industrial energetic use, but instead within a research purpose.
The easiest configuration for a toroidal magnetic geometry it would be a purely toroidal magnetic field $\vec{B_T}$ created by some toroidal coils. This kind of choice, however, do not allow to confine properly particle. As a matter of fact, because of the curvature of the field and the field magnitude gradient some drift establish. The first order approximation

of those are:

$$\vec{v}_{\nabla B} = \frac{c\mu}{q}\frac{\vec{B}\times\nabla B}{B^2} \tag{1.15}$$

$$\vec{v}_{\kappa} = \frac{cmV_{\parallel}^2}{qR_c}\frac{\vec{n}\times\vec{B}}{B^2} \tag{1.16}$$

where $\mu = \frac{mV_{\perp}^2}{2B}$, q and m are the particle's charge and mass, $V_{\perp,\parallel}$ are the perpendicular and parallel velocity of the particle respectively and R_c is the curvature radius of magnetic field line. Moreover, since those velocity depend on the charge, they will tend to split particle with opposite charge and consequently an electric field $\vec{E}$ will form, causing a further drift.

$$v_{E\times B} = c\frac{\vec{E}\times\vec{B}}{B^2} \tag{1.17}$$

Finally, further forethought is needed when the description passes from a single particle picture to a macroscopic one. To stabilise particle's orbits magnetic lines should twist around the magnetic surfaces, averaging out the 1.15-1.16 drift motions. Mainly, there are two way to make this happen: by adding a poloidal magnetic component $\vec{B_P}$ allowing some electric current flow through the plasma or by rotating poloidal cross section of flux surfaces along the toroidal angle, making the magnetic axis[5] not a planar curve, this latter called magnetic torsion ([14, 24]). The choice of one solution in lieu of others determines the machine specifications and distinguishes tokamak from stellarators. In the first machines, indeed, twisting is provided by a plasma current creating a poloidal magnetic field 10 times smaller than the toroidal one, in stellarators, magnetic torsion and flux surfaces rotation are applied.

1.3. The Tokamak Device

Across the world several tokamak-type machines are still in construction, consisting finally in a toroidal chamber where plasma is confined by mean of magnetic fields. Three different sets of coils are fielded.

The first group is arranged to form a toroidal solenoid wrapping the void chamber and producing the only toroidal magnetic component present. Because of this configuration the magnetic field is not constant along the whole magnetic surface. In [R,θ,Z] reference system, an orthonormal cylindrical system, R,θ,Z being respectively the radial, poloidal

[5] A brief discussion of what the magnetic axis is, it is found in A

and vertical coordinate, is possible to express B_T [20] as function of the distance from the centre R, the number of coils N and the current flowing through each coil I_c

$$B_T(R) = \frac{2NI_c}{cR} \tag{1.18}$$

Since equation 1.18 displays a monotonically decreasing behaviour it allows to divide the poloidal cross section in two different zone. The inner part of the tokamak is said High Field Side (HFS), the outer Low Field Size (LFS). Such field can reach values of tens of T [6] [29], needing high currents in the coils, in the order of hundreds of MA [7]. Such high currents would be unsustainable for ordinary coils, need the use of superconducting technology. The coils used to this purpose are pictured in figure 1.5 in blue.

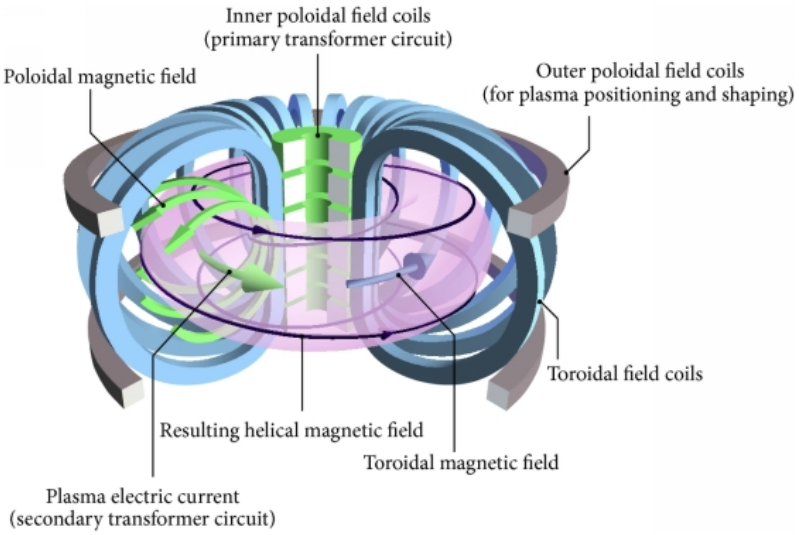

Figure 1.5: Schematic representation of a tokamak machine's set of coils. The blue ones are the one generating the toroidal magnetic field. In green is highlighted the central coil inducing the plasma current. The grey coils are used for shaping and positioning. [38]

As discussed previously, in subsection 1.2.4, a single poloidal field is not sufficient to confine the plasma and a further poloidal field B_p is needed, usually at least 10 times weaker than B_T. Tokamak machine induce in the plasma a current in order to accomplish this requirement, through a central coil working as the primary circuit of a transformer is used - the secondary circuit being the plasma itself. This confers to the machine an intrinsic pulsed behaviour since such a technology cannot work with continuous current unlike

[6] Tesla, SI unit for the magnetic B field.
[7] Ampère: SI unit for electric current.

ordinary coils. Indeed, in order to keep the plasma current as more constant as possible the current flowing in the primary circuit increases linearly. Such a temporal behaviour, clearly, is technically impossible, therefore repeated discharges are needed. The central coil is pictured in green in figure 1.5.

Finally, a third order of coils are placed horizontally, pictured in grey in figure 1.5. Those coils contribute to poloidal component and they are used for plasma positioning and shaping. Theirs effects are quite important for stability purposes, the topic investigated in this work.
Since the magnetic field presents a continuous and differentiable law, it is possible to define a set of lines everywhere tangent to the field itself, called magnetic field lines. Those constitutes a very important figure of merit in the tokamak since they allow to define the magnetic surfaces that compose the layer structure of the magnetic field. Since they are everywhere tangent to magnetic field they obey the law:

$$d\vec{l} \times \vec{B} = 0 \tag{1.19}$$

Here $d\vec{l}$ is the vector between two infinitesimally close points belonging to the field line. From that, in the proper coordinate system, where ϕ is the poloidal angle, θ is the toroidal one and a is the distance of the line from the magnetic axis (§ A) it is possible to retrieve the equation

$$q = \frac{d\theta}{d\phi} = \frac{aB_T}{RB_p} \tag{1.20}$$

This important parameter is called safety factor. It is not constant in general in the tokamak cross section nor along the magnetic surface. As its definition 1.20 suggests it is proportional to the variation of the toroidal angle with the poloidal one. If this parameter is constant along all the curve it represents also the number of toroidal turns accomplished every poloidal one, otherwise, the relation is only local. This parameter allows to distinguish between two different kind of curves. The first, with $\frac{1}{2\pi}\int_0^{2\pi}\frac{1}{q(\theta)}d\theta \in \mathbb{Q}$, are closed curves that come back to the starting point after an integer number of turns along the magnetic surface. If the condition does not hold, the curve wraps forever on the magnetic surface without ever closing.
A second important parameter for what concerns tokamak geometry it is the aspect ratio. This is defined as the ratio between the tokamak major and minor radius, R_0, a. The major radius is the average distance from the tokamak symmetry axis, a is the distance

of the walls from the magnetic axis.

$$AR = \frac{1}{\varepsilon} = \frac{R_0}{\mathrm{a}} \tag{1.21}$$

ε is therefore a measure of how much the tokamak torus can be confused with a straight cylinder. This happens in the limit $\varepsilon \to 0$ said large aspect ratio limit. In usual tokamak the aspect ratio is in the order of $AR \simeq 3$, e.g. a $1GW^{th}$ tokamak[8] could be characterised by $R = 6m$, $\mathrm{a} = 2m$ leading to a volume of, roughly, $V = 10m^3$.

Finally, another important figure of merit is the β parameter, defined as a dimensionless pressure through the equation

$$\beta = \frac{nT_e}{B^2/8\pi} \tag{1.22}$$

It is possible to define also the poloidal and toroidal one, respectively β_p and β_T, substituting in equation 1.22 the poloidal or toroidal component instead of the magnetic field. Usually, to evaluate β average values are used. The importance of this last constant lies in his interpretation as the confinement efficiency. As a matter of fact, if all the magnetic energy were used to compress the plasma would lead to $\beta = 1$. This implies also that it holds always $\beta < 1$.

Parameters 1.20, 1.21 and 1.22 are intimately connected since it holds

$$\beta = \beta_p \frac{\varepsilon^2}{q^2|_{a=\mathrm{a}}} \tag{1.23}$$

Since in tokamak's configuration are characterised by $q \sim 1$, 1.20 implies $\beta_P \sim 1$ and therefore equation 1.23 states that $\beta \sim \varepsilon^2$. This classifies tokamaks as intrinsically low β machines.

The heating of the plasma is firstly on charge to ohmic losses in plasma up to the temperature of some keV. To reach the ignition regime, anyway, this is not sufficient yet and additional power is injected trough accelerated particle beams and electromagnetic wave. Both coils feeding and power injection are energetically greedy processes, impacting on the machine energetic balance. An important parameter describes this

$$Q = \frac{E_f}{E_{ext}} \tag{1.24}$$

being the ratio between energy produced by fusion processes E_f and the energy E_{ext}

[8]Such a wording denote a facility's thermal output and it is read "thermal GW"

inserted in the system. Despite theoretically ignition condition correspond to $Q = \infty$, the highest value achieved for the moment is $Q = 0.7$ in JET facility [17], but it is foreseen to reach $Q = 10$ with ITER in 2050 [32].

1.3.1. The Plasma Poloidal Cross Section

The poloidal cross section of a plasma is characterised by three main zones. The first to be found starting from the innermost region is the core. This region is where the fusion occurs and therefore it needs high pressures. Magnetic pressure ($B^2/8\pi$) can scale up to 300 atm [15]. The temperature and the density inside it are in the order respectively of 10 keV, and $10^{15} cm^{-3}$. The core is compressed by the outer layers and the fluctuation of the various fields are very small: the relative variation of it in the order of 1%.
Facing the core, it is present the edge region. Such a region is a layer connecting innermost and the outermost values, and it is a transitional region. It is characterised by important thermal gradient and is very thin. Gradients can be stepper than 10 keV/m. Here, also the density drops of several order of magnitude. The edge region is limited on the outward from the Last Closed Flux Surface (LCFS) or separatrix, consisting, as the name says, in the last closed flux surface. The outer ones will end on some solid part of the wall.

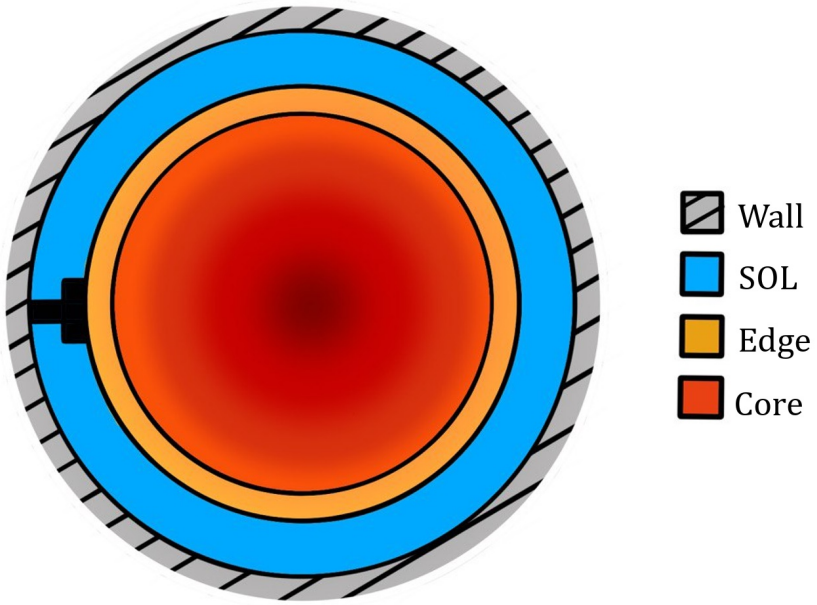

Figure 1.6: Circular plasma cross section, in which the three main regions are highlighted. The inner region corresponds to the core one, the orange to the edge and the blue one to the SOL. The black object on the left represents a limiter, a device used to limit the plasma-wall interaction. It causes the appearance of the LCFS, which poloidal section is the black solid line between the blue and the orange area.

The outer region of a confined plasma is called Scrape Off Layer (SOL). This, together to the edge region form the periphery. It is characterised by very loose plasma and temperatures in the order of 10eV. Since the temperature is low electromagnetic effects become more important making this region the cause of almost the totality of the radiation the machine causes. The low pressure, also, causes the fluctuations in the plasma to be very important, being even higher than the equilibrium values themselves in the outmost layers of this region, the outer-SOL. Despite this layer is populated only a few percent of the total plasma's particles are present, it is crucial for the machine well behaviour since it controls most of the instabilities present in the configuration, with the edge layer and determines the heat and particle flux exchanges with the tokamak's wall, a complex phenomenology called plasma-wall interaction. SOL's Magnetic surfaces, indeed, are open and they end on some region of the tokamak wall. Since 1eV corresponds to roughly 10'000 K SOL's average temperature is way higher than common materials can suffer. To handle this, it has been chosen to localise the region where the most of plasma-wall interactions occur to a single component in order to allow the rest of the wall to milder conditions. The component that directly face the SOL's plasma are the limiter, a slab inserted at HFS along all the toroidal perimeter. In more complex geometries a divertor can be implemented, i.e. a long plate in the lower part of the plasma chamber on which all the magnetic surfaces of SOL closes. Both the divertor and the limiter have better thermomechanical properties than the rest of the wall.

1.4. Importance of Plasma Shaping

In modern tokamak, as anticipated in section 1.3, there is present an additional order of coils with the precise purpose of conferring a complex geometry to the plasma. Such technical solution is called plasma shaping. It consists in using additional poloidal fields to bend the magnetic surfaces, otherwise tori. This technique has mainly importance on the plasma periphery, and much less on the core that maintains a more or less circular shape.

Plasma shaping has many motivations and scopes. First of all, it allows to confine the plasma minimising the plasma-wall interaction, causing the knockout of wall's atoms due to highly energetic plasma's particle. The ablated atoms enter in the plasma and are quickly partially ionised, causing an increase of radiative losses and decreasing the confinement and fusion properties. On the wall side, it loses integrity and structural

properties. Moreover, the shape in which the plasma is moulded influence the heat and particle fluxes, i.e. the plasma transport properties, diminishing them and securing them below the maximum ones the structural materials can handle.

Moreover, bending the field lines it is possible to redirect them on the divertor plate, as implemented in ITER and DTT[9]. In that way, particle streaming along the magnetic lines are collected in the divertor, diminishing the average damages to the walls. Clearly, since a perpendicular diffusion is present in the plasma, some particles will end impacting on the wall, anyway.
As it pictured in figure 1.7 in such configurations this line is characterised by the so-called X-point, where it intersects itself.
Shaped geometries are usually characterised by the LCFS presenting an X-point, or null-point, where the poloidal magnetic component is zero and the field is purely poloidal. In this point the magnetic surface cross itself forming, in the poloidal cross section, a typical "X" shape as in the blue circle of figure 1.7.

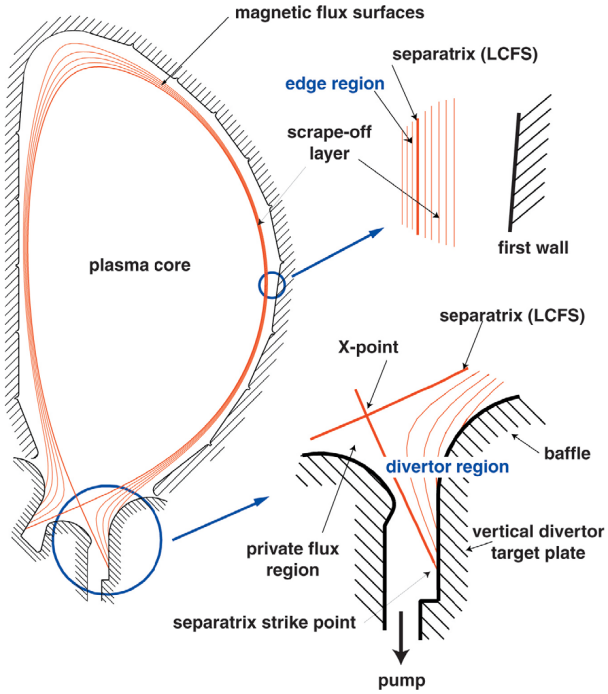

Figure 1.7: Shaped plasma cross section. In the figure is easy to distinguish the core region, the edge and the SOL In the blue circle it is highlighted the X-point. [12]

[9]Research tokamak that will be built in Rome at ENEA research facility in the next years.

1.4.1. Periphery Dynamics

As many studies pointed out, the periphery dynamics is responsible for most of the overall confinement of tokamak device [33].
Two working modes are mainly observed: H and L modes. L mode, or low confinement mode is the characterised by a relatively large amount of turbulence which allows energy to escape the confined plasma. In H-mode, or high-confinement mode, a pedestal develops in pressure distribution, in the edge region, stepping near the separatrix. That causes a radial electric field to establish, implying a strong reduction of turbulence level [10]. The H-mode pedestal is periodically released by the injection of high energy particle from the core in a phenomenon called edge-localised modes (ELMs) causing sudden variations in the energy and mass fluxes that the walls suffer. The settling of one of the two modes is controlled by the transport properties of the plasma that depends on the thermodynamic state, on the magnetic field present, the shaping and various other parameters.
Since in the peripheral region the temperature is quite low, a high collisionality is expected and therefore it is possible to infer a near equilibrium energy distribution. This will have a major role in the treatment done in subsection 2.1.1 and in chapter 2 generally.
Finally, the highly non-linear turbulent processes imply the presence of a large spectrum of relevant time and space scales. At this simulation complication it adds the strong anisotropy typical of this phenomenon, where the parallel wavevectors are much smaller than the perpendicular ones ($k_{\parallel} = \vec{k} \cdot \vec{b} \ll k_{\perp} = || \vec{k} - k_{\parallel}\vec{b} ||$) [4].
In the peripheral region, finally, occurs many modes that are potentially unstable. Such modes could lead to the destabilisation and the disruption of the plasma equilibrium, causing the fading in the confinement properties and therefore the loss of ignition condition. This would be detrimental for a tokamak and would lead the machine into failure.

1.4.2. The Effect of Triangularity

It is said that a magnetic surface presents a not null triangularity when the poloidal cross section is characterised by a "D" shape, as in case of figure 1.7. If the D points outward, toward the LFS, the triangularity is said positive, if points towards the HFS, it is said negative. The triangularity parameter can be retrieved explicitly in the Sobolëv equilibrium (§ A), a special set of self-consistent magnetic equilibria, but is a more general concept, applicable also to other configurations. Edge dynamics is intimately influenced by such a parameter, this last impacting on turbulence and then on fluctuation and instabilities as clearly showed in [7, 9]. In their works Fontana et al. and Huang and al. analysed shots in TCV in Lausanne, Switzerland, over a wide range of elongation and triangularity values.

What they found was a better confinement in negative triangularity and a substantial reduction of turbulent density fluctuation. As showed in previous works [23, 34] the triangularity, especially the negative one, has a huge impact on the transport properties in the peripheral region. The equilibrium that establishes is similar to the H-mode, ensuring therefore a good confinement, but do no present the periodical release due to the ELMs, leading to more steady fluxes on the plasma wall and, in general, to a better confinement.

1.5. Motivation and Scope of the Work

The plasma behaviour in the edge layer in turbulent regime is an important topic in nuclear fusion devices, the complete characterisation of the turbulent regimes and the transport characteristics being an important threat in the current research field.
The external region in a tokamak, formed by the SOL and edge layer, sets and directs a wide compendium of phenomena at the basis of the machine performance. It is in this region that L-H modes settle determining the confinement properties in the core. The edge, through the developed mode and the ELMs, controls the magnitude of heat and particles fluxes arriving to the machine's walls, contributing to setup the properties of the plasma-wall interaction. Finally, through diffusion, edge allow nuclear ashes to flow toward the outer region where they can be collected and removed in order to keep a steady plasma composition. Also, the edge and SOL region determines the stability of the magnetic configuration. The knowledge of them allows to control and correct eventual bad behaviour of the configuration.
All those phenomena's importance is heavily dependent on the shaping attributed to the plasma, in a particular way on triangularity. Moreover, except for some special machine as the TCV[10] at the Swiss Plasma Centre in Lausanne, tokamaks do not have an elevated flexibility for what concerns the magnetic configuration, since their coils are fixed. For that the magnetic configuration of the machine is a parameter that is assessed in the early phase of the device's project. With new machines and tests to be designed, as the DTT in Frascati, Rome and the more important DEMO in the Eurofusion research project, in the near future, the magnetic configuration is a major and meaningful aspect to study.
This work frames in such a contest, basing its result on numeric simulations and some analytical tool. It will be proposed a method to evaluate the magnetic surfaces poloidal section without the recurrence to complex and heavy MHD equilibrium solver. The instabilities growth rate analysis and the pressure gradient length evaluation then, will be

[10]TCV, as a matter of facts, stands for "Tokamak à Configuration Variable" that literally translates in "Variable Configuration Tokamak".

carried out through GBS code, in both linear and nonlinear case, a complete code capable to keep in account the plasma turbulence in a self-consistent way, without the need to artificially dissociate the driving phenomena. The linear one will be coupled to the code implementing the surface's discretization method.
This thesis sets as his goal is to provide firstly a description of the physical basis of the poloidal cross section discretization method. Then the effect of the shaping on the plasma instabilities and on the turbulence will be analysed, finally comparing it to the full model. A non-linear model will be presented to the auto-consistent evaluation of the pressure gradient length, fundamental for the evaluation of the predicted confinement mode.
The document is organised as follows:
In Chapter 1 a brief resumé is displayed in order to better frame the technology at the basis of the discussed matter. In such an optics the aim is to provide some insight on the role of the nuclear fusion in modern energy source mix, its physical grounds and the machines used to exploit it. Particular focus is let to magnetic surfaces cross section shaping, constituting the core underneath the discussion.
In Chapter 2 it is provided a more complete treatment of the physical description of the phenomena. The derivation begins with the retrieval of multifluid equations for plasma and then develops towards the assumption made to reach the Braginiskii fluid equations. Finally, some further operations are made in order to adimensionalise the treated set. With such a work some new operators are defined. At the end, the linear GBS code approach is made explicit.
In Chapter 3 an agile discussion is carried on the code used in the linear analysis. Firstly, the linearisation of the GBS equation is tackled. Then the approach used to discretise the magnetic configuration is resumed. Such an approach constitutes an original aspect of this work and for that it has been chosen to deepen the procedure. At the end of the unit the four magnetic configurations used, Circular, Global Symmetric, Global Positive, Global Negative are presented.
In Chapter 4 the main linear results retrieved through the combination of the discretization code and linear GBS are presented, starting from a particular instability to land to the full model. Along the line of argument, the reduced sets of equation are presented and some analytical treatments are carried. The last section, finally, will display the method for the self-consistent evaluation of the pressure gradient length and its application.
In Chaptercap:cap5 the non-linear results of GBS code are displayed and discussed and then the evaluation pressure gradient length is evaluated. In Chapter 6 a resumé of the results is presented and some possible future steps are outlined.
In Appendix A, finally, it is briefly deduced the Grad-Shafranov equation and the Solov'ëv equilibrium is described in the main optics to provide an extended background on the

magnetohydrodynamic self-consistent configurations and to complete the meaning of the triangularity parameter.

2 | Modelling of Tokamak Periphery

In chapter 1 a synopsis of nuclear fusion and its placement in energetic problem is given, in which, as discussed in subsection 1.2.3, the plasma plays an unquestionable role. To be allowed to make quantitative prediction, however, some more forethought is needed in order to comprehend some more details on plasma modelling and its numerical treatment. Firstly, some insights on plasma description will be given, with focus on two-fluid Braginiskii model (§ 2.1) and its closure in the case of edge plasma (§ 2.1.2). Some attention will be given to discuss the conditions for which the approximation is valid (§ 2.1.1). Then, some furthers approximation will be discussed (§ 2.1.3) in order to obtain some handy set of equations, the drift-reduced Zeiler equations.
Then the set of equation GBS code solve are discussed (§ 2.2), treating the involved differential operators (§ 2.2.1), the adimensionalised set of equations (§ 2.2.2) and the geometry (§ 2.2.3). A brief insight in one of the principal unsuitable modes is provided. (§ 2.2.4). Finally, the chapter concludes with a brief discussion of previous work present in literature (§ 2.3).

2.1. The Two-Fluid Model

To get to a multiphase portrait is possible to lead from the Boltzmann equation stating the conservation of the number of particle through the evolution of $f_a(t, \vec{x}, \vec{v})$. This field describes the particles' density per unit of volume in phase space and the label a refers to a single charged particle population.

$$\frac{\partial f_a}{\partial t} + \vec{v} \cdot \frac{\partial f_a}{\partial \vec{x}} + \frac{\vec{F}_a}{m_a} \cdot \frac{\partial f_a}{\partial \vec{v}} = C_a \tag{2.1}$$

In this equation $\vec{F}_a$ is the Lorentz force $\vec{F}_a(t, \vec{x}, \vec{v}) = q_a(\vec{E}(t, \vec{x}) + \frac{1}{c}\vec{v} \times \vec{B}(t, \vec{x}))$, m_a is the

mass of the a-th species, q_a its charge and C_a is the collisional term that describes all collisional interaction between particles. In the specific it is this term who causes to the population to tend trough a Maxwellian distribution. The typical scale time in which this occurs it's said relaxation time.

Electromagnetic fields can be described through Maxwell equations

$$\nabla \cdot \vec{E} = 4\pi\rho_{ext} + 4\pi \sum_a \int q_a f_a(t, \vec{x}, \vec{v}) d\vec{v} \tag{2.2}$$

$$\nabla \times \vec{E} = -\frac{1}{c}\frac{\partial \vec{B}}{\partial t} \tag{2.3}$$

$$\nabla \cdot \vec{B} = 0 \tag{2.4}$$

$$\nabla \times \vec{B} = \frac{4\pi}{c}\vec{j}_{ext} + \frac{4\pi}{c} \sum_a \int q_a \vec{v} f_a(t, \vec{x}, \vec{v}) d\vec{v} + \frac{1}{c}\frac{\partial \vec{E}}{\partial t} \tag{2.5}$$

where the charge density and the current density due to plasma's particles are expresses throughout the particle density function. Those fields do not refer to microscopic value of the field since too many details would arise from such a picture but instead there are smoothed fields throughout some sort of average or filter. In that way the force F_a do not suffer from rapidly fluctuating microfields due to particle getting close each other. Anyway, such phenomena are not neglected but are summarized in the C_a operator of equation 2.1. For generality's sake it must be said that those are not the only phenomena described by the collision operator. In fact, ionisation, chemical reactions and atomic reactions can be inserted in the model through this therm. Anyway, in the following all those reactions can be neglected, so the collision operator will essentially describe scattering. This leads to the important property that

$$\int C_a d\vec{v} = 0 \tag{2.6}$$

Lastly is worthy to remember that the electromagnetic fields in equations 2.2-2.5 can be represented effectively with the potentials ϕ and $\vec{A}$. The relation between those and $\vec{E}$ and $\vec{B}$ is not unique (cfr. [20]). In the further we will use

$$\vec{E} = -\nabla\phi - \frac{1}{c}\frac{\partial \vec{A}}{\partial t} \tag{2.7}$$

$$\vec{B} = \nabla \times \vec{A} \tag{2.8}$$

To get to the multifluid description the time evolution of the first three f_a's momenta are

taken into account. Thereby, density, mean velocity and temperature are introduced.

$$n_a(t,\vec{x}) = \int f_a(t,\vec{x},\vec{v})d\vec{v} \tag{2.9}$$

$$\vec{V_a}(t,\vec{x}) = \frac{1}{n_a}\int \vec{v} f_a(t,\vec{x},\vec{v})d\vec{v} \tag{2.10}$$

$$T_a(t,\vec{x}) = \frac{1}{n_a}\int \frac{m_a}{3}(\vec{v}-\vec{V_a})^2 f_a(t,\vec{x},\vec{v})d\vec{v} \tag{2.11}$$

Those three new variables describe respectively the number of particles per unit space volume, the ordered velocity of the particles i.e. the velocity describing the local common motion of particles and, finally, the energy raising from the disordered velocity.

From equation 2.1, multiplying by the velocity functions, respectively, 1, $m_a\vec{v}$ and $\frac{m_a}{3}v$ and integrating along all the velocity space, we retrieve the multi-fluid equations, called thys way because to describe completely the plasma the three Navier-Stokes-like equation 2.12, 2.13 and 2.14 are needed for each species of the plasma:

$$\frac{\partial n_a}{\partial t} + \nabla\cdot(n_a\vec{V_a}) = 0 \tag{2.12}$$

$$m_a n_a(\frac{\partial \vec{V_a}}{\partial t} + \vec{V_a}\cdot\nabla\vec{V_a}) = -\nabla p_a - \nabla\cdot\pi_a - q_a n_a[\vec{E} + \frac{1}{c}\vec{V_a}\times\vec{B}] + \vec{R_a} \tag{2.13}$$

$$\frac{3}{2}n_a(\frac{\partial T_a}{\partial t} + \vec{V_a}\cdot\nabla T_a) + p_a\nabla\cdot\vec{V_a} = -\nabla\cdot\vec{q_a} - \pi_a : \nabla\vec{V_a} + Q_a \tag{2.14}$$

As it easily stands out new quantities arises in the equations due to the decomposition in ordered and disordered velocity, i.e. $\vec{v} = \vec{V_a} + \vec{v'}$. The explicit formulations of those new symbols are summarised in the table 2.1.

name	symbol	expression
Pressure	p_a	$n_a m_a < v'^2 >_a /3$
Viscous stress tensor	$[\pi_a]_{i,j}$	$n_a m_a < v'_i v'_j - v'^2/3\delta_{ij} >_a$
Momentum density due to collision	$\vec{R_a}$	$\int m\vec{v'}C_a$
Heat flux	$\vec{q_a}$	$< m/2 v'^2\vec{v} >_a$
Heat density due to collisions	Q_a	$\int m/2 v'^2 C_a d\vec{v}$

Table 2.1: Summary of different new symbols introduced in the equations 2.12 -2.14

In table 2.1 the operator $< \cdot >_a$ corresponds to $\frac{1}{n_a}\int \cdot f_a(t,\vec{x},\vec{v})d\vec{v}$. The explicit dependence of π, R_a, q_a, Q_a on the density function's momenta and their derivatives is not trivial. To express them the subsequent momentum would be needed and then its evolution equation,

This would lead to an infinite hierarchy of equation that, mathematically, is equivalent to the leading Boltzmann equation. This is called closure problem. A way to address this was proposed by Braginiskii in 1965. It is worth to notice that, instead, the expression of p_a is quite easy, as it holds that

$$p_a = n_a T_a \tag{2.15}$$

2.1.1. The Braginiskii Equation

As pointed out in [41] as long all quantities vary slowly in space and time is possible to use a local solution that derive from the existence of the relaxation process. Indeed, Boltzmann H theorem suggests (cfr. [21]) that this process causes any arbitrary distribution to evolve toward a maxwelian one, as it is the solution for the homogeneous Boltzmann equation, where the gradients and time derivative vanish identically. This mean that as long all phase space density's momenta are characterised by small gradients in time and space the actual distribution will be close to a maxwellian one and the error will be somehow proportional to those gradients. Since the maxellian distribution of the a-th specie is characterised completely by n_a, V_a and T_a the same quantities can be used to express the correction to the Maxwellian distribution and therefore π, $\vec{q}$, $\vec{R}$ and Q. The proportionality coefficients are called transport coefficients.
The smallness of gradients must anyway be quantified. For time variable it is possible to address that the collision time τ_R is much faster than the evolution time scale

$$\frac{1}{g}\frac{\partial g}{\partial t} \simeq \frac{1}{\tau} \ll \frac{1}{\tau_R} \tag{2.16}$$

where g is any field describing plasma properties. For what concerns the spatial derivatives it must hold that the scale length is big with respect the excursion of particles:

$$\frac{g}{\nabla_\perp g} \gg \rho_L \qquad\qquad \frac{g}{\nabla_\parallel g} \gg l_{mfp} \tag{2.17}$$

where ρ_L is the Larmor radius or the gyroradius and l_{mfp} is the mean free path i.e. the mean path done by particle between any collision and the subsequent. [1]

As Braginiskii did, from now on we will consider a completely ionised plasma formed only by a single species of ions, whose charge is namely Ze and the relative electrons e to

[1] The two operators are called parallel gradient and perpendicular gradient and they are defined as $\nabla_\parallel f = \vec{b}\cdot\nabla f$ and $\nabla_\perp f = \vec{b}\times(\vec{b}\times\nabla f)$ where $\vec{b} = \frac{\vec{B}}{B}$ is the magnetic field versor.

assure quasineutrality. The two components of the plasma will be labelled "i" for ion and "e" for electron. This will not lead to a lack of generality since is still possible to follow the same strategy for a multiple ion species plasma. Moreover, the transport coefficients described in the following are evaluated in a strong magnetic field approximation

$$\omega_{e,i}\tau_{ei} \gg 1 \tag{2.18}$$

Here, $\omega_{e,i}$ is the gyrofrequency $\omega_{e,i} = \frac{q_{e,i}B}{m_{e,i}c}$ and $\tau_{e,i}$ is the electron/ion collision time $\tau_e = \frac{3\sqrt{m_e}T_e^{3/2}}{4\sqrt{2\pi}\lambda e^4 Z^2 n_i}$, $\tau_i = \frac{3\sqrt{m_i}T_i^{3/2}}{4\sqrt{\pi}\lambda e^4 Z^4 n_i}$ and λ is the Coulomb logarithm.

2.1.2. Transport Coefficients

Firstly, a model for $\vec{R}$ in equation 2.13 is proposed. It is useful to remark that because of its physical interpretation, i.e. the force arising from the presence of collisions between the two species, and momentum balance it must hold

$$\vec{R_i} = \vec{R_e} \tag{2.19}$$

Moreover, each one is the sum of two contributions: a friction force arising from ion/electron collisions and a thermal force due to the simultaneous presence of a thermal gradient and collisions.

$$\vec{R_e} = \vec{R_u} + \vec{R_i} \tag{2.20}$$

$$\vec{R_u} = en_e(\frac{\vec{j_\parallel}}{\sigma_\parallel} + \frac{\vec{j_\perp}}{\sigma_\perp}) \tag{2.21}$$

$$\vec{R_t} = -0.71 n_e \nabla_\parallel T_e - \frac{3}{2}\frac{n_e}{\omega_e \tau_e}\vec{b} \times \nabla_\perp T_e \tag{2.22}$$

$$\tag{2.23}$$

Where $\vec{j_{\parallel,\perp}} = en_e(V_{\parallel,\perp,i} - V_{\parallel,\perp,e})$, $\parallel$ and $\perp$ are with respect to $\vec{B}$ and $\sigma_{\parallel,\perp}$ is the parallel/perpendicular conductivity. Their expressions will be listed in table 2.2.
At the same way is possible to split $\vec{q_e}$ in two terms, the first $\vec{q_{u,e}}$ related to the thermal force $\vec{R_t}$, the second $\vec{q_{e,u}}$ mainly due to thermal gradients. For what concerns $\vec{q_i}$, its expression is easier since is possible to neglect terms of order $\omega\tau_i$:

$$\vec{q_{u,e}} = 0.71 n_e T_e (\vec{V_{\parallel,e}} - \vec{V_{\parallel,i}}) + \frac{3}{2}\frac{n_e T_e}{\omega_e \tau_e}\vec{b} \times (\vec{V_{\parallel,e}} - \vec{V_{\parallel,i}}) \tag{2.24}$$

$$\vec{q_{t,e}} = -\chi^e_{\parallel}\nabla_{\parallel} T_e - \chi^e_{\perp}\nabla_{\perp} T_e - \frac{5}{2}\frac{c n_e T_e}{eB}\vec{b} \times \nabla T_e \tag{2.25}$$

$$\vec{q_i} = -\chi^i_{\parallel}\nabla_{\parallel} T_i - \chi^i_{\perp}\nabla_{\perp} T_i - \frac{5}{2}\frac{c n_i T_i}{ZeB}\vec{b} \times \nabla T_i \tag{2.26}$$

Here, $\chi^{e,i}_{\parallel,\perp}$ is the electron/ion parallel/perpendicular thermal conductivity.

As the second rank tensor π is considered, a reference system is needed to express its component. For that, z-direction is imposed to be aligned to the magnetic field. Moreover, the rate-of strain tensor W must be defined

$$W_{ij} = \frac{\partial V_i}{\partial x_j} + \frac{\partial V_j}{\partial x_i} - \frac{2}{3}\frac{\partial V_l}{\partial x_l}\delta_{ij} \tag{2.27}$$

And therefore

$$\pi_{zz} = -\eta_0 W_{zz} \tag{2.28}$$

$$\pi_{xx} = -\frac{\eta_0}{2}(W_{xx} + W_{yy}) - \frac{\eta_1}{2}(W_{xx} - W_{yy}) - \eta_3 W_{xy} \tag{2.29}$$

$$\pi_{yy} = -\frac{\eta_0}{2}(W_{xx} + W_{yy}) - \frac{\eta_1}{2}(W_{xx} - W_{yy}) + \eta_3 W_{xy} \tag{2.30}$$

$$\pi_{xy} = \pi_{yx} = -\eta_1 W_{xy} - \frac{\eta_3}{2}(W_{xx} - W_{yy}) \tag{2.31}$$

$$\pi_{xz} = \pi_{zx} = -\eta_2 W_{xz} - \eta_4 W_{yz} \tag{2.32}$$

$$\pi_{yz} = \pi_{zy} = -\eta_2 W_{yz} - \eta_4 W_{xz} \tag{2.33}$$

Also, the viscosities η_0, η_1, η_2, η_3, η_4 are listed below.

Finally, the heat generation term appearing in 2.14 can be made explicit as:

$$Q_e = -\vec{R_e} \cdot (V_e \vec{-} V_i) - Q_i \tag{2.34}$$

$$Q_i = \frac{3 m_e n_e}{m_i \tau_e}(T_e - T_i) \tag{2.35}$$

Of those terms the fist can be interpreted as Joule heating due to friction between ions and electrons and the second term as due to the temperature difference between the two species. In line of principle the Joule heating should appear also in Q_i but it is negligible with respect the other term.

symbol	expression
$\sigma_{\parallel}$	$\frac{e^2 n_e \tau_e}{m_e}$
$\sigma_{\perp}$	$1.96\sigma_{\parallel}$
$\chi^e_{\parallel}$	$3.16\frac{n_e T_e \tau_e}{m_e}$
$\chi^e_{\perp}$	$4.66\frac{n_e T_e}{m_e \omega_e^2 \tau_e}$
$\chi^i_{\parallel}$	$3.9\frac{n_i T_i \tau_i}{m_i}$
$\chi^i_{\perp}$	$2\frac{n_i T_i}{m_i \omega_i^2 \tau_i}$
η^e_0	$0.73 n_e T_e \tau_e$
η^e_1	$0.51\frac{n_e T_e}{\tau_e \omega_e^2}$
η^e_2	$4\eta^e_1$
η^e_3	$-\frac{n_e T_e}{2\omega_e}$
η^e_4	$2\eta^e_3$
η^i_0	$0.96 n_i T_i \tau_i$
η^i_1	$\frac{3}{10}\frac{n_i T_i}{\tau_i \omega_i^2}$
η^i_2	$4\eta^i_1$
η^i_3	$\frac{n_i T_i}{2\omega_i}$
η^i_4	$2\eta^i_3$

Table 2.2: Coefficients for the Braginskii closure [25]

2.1.3. Drift Reduced Approximation

The multifluid equations in the previous section (2.12-2.14) with the Braginiskii closure (§ 2.1.1, 2.1.2) still need further simplifications in order to be numerically handled.
As a matter of facts those equation allow to describe the plasma dynamics in a wide range of time and spatial scales, spanning from electron cyclotron frequency and electron Larmor radius, up to machine size and confinement time. In the edge region time variations are quite slower than ion gyromotion and spatial variations are in the order of $\rho_s = C_s/\omega_i$, the Larmor radius at the sound speed c_s approximation, assuming:

$$\frac{\partial}{\partial t} \sim \vec{V_{E\times B}} \cdot \nabla \sim \frac{\rho_s^2}{L_\perp}\omega_i \ll \omega_i \tag{2.36}$$

since the equilibrium scale length, $L_\perp$, is much larger than ρ_s. $(-\nabla\phi \times \vec{b})$ is the E×B velocity. As anticipated, moreover, the plasma will be considered to be quasineutral since turbulence plays a role at spacial scales $\rho_s \gg \lambda_D$ where $\lambda_D = \sqrt{T_e/(2\pi e^2 n)}$ is the Debye

length. As consequence $n_e = n_i = n$.

The main idea is therefore to split the dynamic in parallel and perpendicular direction, saving corrections up to first order:

$$\vec{V_{\perp,e}} = \vec{V}_{E\times B} + \vec{V}_{*,e} \tag{2.37}$$
$$\vec{V_{\perp,i}} = \vec{V}_{E\times B} + \vec{V}_{*,i} + \vec{V}_{pol} \tag{2.38}$$

where $\vec{V}_{*,a}$ is the a-th species diamagnetic drift

$$\vec{V}_{*,a} = \frac{c}{enB}\vec{b} \times \nabla p_a \tag{2.39}$$

and $\vec{V_{pol}}$ is the polarization drift, a first order correction. A complete derivation of 2.37 - 2.38 and the consequences of such approach can be found in [44]

Continuity Equations

Since the particles motion along the perpendicular and the parallel directions have been split, the continuity equations reads:

$$\frac{\partial n_e}{\partial t} + \nabla \cdot \left[n \left(\vec{V}_{E\times B} + \vec{V}_{*,e} + \vec{V}_{\parallel,e} \right) \right] = 0 \tag{2.40}$$
$$\frac{\partial n_i}{\partial t} + \nabla \cdot \left[n \left(\vec{V}_{E\times B} + \vec{V}_{*,i} + \vec{V}_{pol} + \vec{V}_{\parallel,e} \right) \right] = 0 \tag{2.41}$$

Vorticity Equation

It is useful to define a new variable, $\omega = \nabla^2_\perp \phi$, the vorticity, which is related to the fluid rotation on the plane perpendicular to the magnetic field. An equation describing the evolution of such variable can be obtained by subtracting the equation 2.12 for both ions and electron and decomposing velocity as proposed in **??**, and applying Boussinesq approximation[2] [13] leading us to

$$\frac{nc}{B\omega_i}\frac{d}{dt}(-\nabla^2_\perp \phi - \frac{\nabla^2_\perp p_i}{en}) + \frac{1}{3m_i\omega_i}\vec{b} \times \vec{\kappa} \cdot \nabla G_i + \nabla_\parallel \frac{j_\parallel}{e} + \nabla \cdot n(\vec{V}_{*,i} - \vec{V}_{*,e}) = 0 \tag{2.42}$$

where $\vec{\kappa} = \vec{b} \cdot \nabla \vec{b}$ is the field curvature, $\frac{d}{dt} = \frac{\partial}{\partial t} + (\vec{V}_{E\times B} + \vec{V}_{\parallel,i}) \cdot \nabla$ and $G_i = -\eta_0(2\nabla_\parallel \vec{V}_{\parallel,i} - \vec{\kappa} \cdot V_i - \frac{1}{3}\nabla \cdot \vec{V_i})$ being the stress function.

[2] Boussinesq approximation consist in $\nabla_\perp \frac{nc}{B\omega_i}\frac{d}{dt}(\vec{E} - \frac{\nabla_\perp p_i}{en}) \simeq \frac{nc}{B\omega_i}\frac{d}{dt}(-\nabla^2_\perp \phi - \frac{\nabla^2_\perp p_i}{en})$

Semi-Electrostatic Limit

To exclude unwanted modes the vector potential (cfr. equations 2.7-2.8) is chosen to be purely parallel to the magnetic field. The magnitude of the vector potential is symbolised by ψ and it is said poloidal flux function.

$$\delta\vec{A} = -\psi\vec{b} \tag{2.43}$$

Therefore, the electric field is given by

$$\vec{E} = -\nabla\phi + \frac{1}{c}\frac{\partial\psi}{\partial t}\vec{b} \tag{2.44}$$

and therefore

$$\nabla_\parallel = \vec{b}\cdot\nabla + \frac{\vec{b}}{B}\times\nabla_\perp\psi\cdot\nabla \tag{2.45}$$

.

It is worth to notice that the Ampere's law now reads as:

$$\nabla_\perp^2\psi = \frac{4\pi}{c}j_\parallel \tag{2.46}$$

Parallel Motion

Time evolution equation for parallel motion can be obtained from equation 2.13 taking the parallel component only, and neglecting $\vec{R}_{e,\parallel}$. The equation reads:

$$m_e\frac{d^eV_{\parallel,e}}{dt} = -\frac{1}{n}\nabla_\parallel p_e - \frac{2}{3}\nabla_\parallel G_e + e\nabla_\parallel\phi - \frac{e}{c}\frac{\partial\psi}{\partial t} + e\frac{j_\parallel}{\sigma_\parallel} - 0.71\nabla_\parallel T_e \tag{2.47}$$

Here $\frac{d^e}{dt} = \frac{\partial}{\partial t} + (\vec{V}_{E\times B} + \vec{V}_{\parallel,e})\cdot\nabla$, the velocity being advected by $\vec{V}_{E\times B} + \vec{V}_{\parallel,e}$ only.
The equation for ion parallel velocity, instead, can be retrieved summing up the parallel component of electron and ion momentum equation 2.13

$$m_i\frac{dV_{\parallel,i}}{dt} = -\frac{1}{n}\nabla(p_i + p_e) - p_i\nabla\times\frac{\vec{b}}{\omega_i}\cdot\nabla V_{\parallel,i} - \frac{2}{3}\nabla_\parallel G_i \tag{2.48}$$

Temperature Equations

The electron temperature equation can be obtained from 2.14. Here the frictional heat generation Q_e and the perpendicular conductivity have been neglected. The obtained

equation reads:

$$\frac{3}{2}n\frac{d^eT_e}{dt}+\frac{3}{2}n\vec{V}_{*,e}\cdot\nabla T_e+p_e\nabla\cdot\vec{V}_e-\frac{5}{2}\frac{c}{e}\nabla\cdot p_e\left(\frac{\vec{b}}{B}\times\nabla T_e\right)-0.71T_e\nabla_\parallel j_\parallel$$
$$-\nabla\cdot(\chi_\parallel\nabla_\parallel T_e)=0 \quad (2.49)$$

For what concerns ion temperature, by some handling, making use of the ion continuity equation 2.41, and neglecting the advection of $\vec{V}_{pol}$ in the total derivative the equation 2.50 is recovered:

$$\frac{3}{2}n\frac{dT_i}{dt}+T_i\left[n\nabla\cdot\left(\vec{V}_{E\times B}+\vec{V}_{\parallel,e}\right)+\nabla\cdot\left(n\vec{V}_{*,e}\right)\right]+\frac{5}{2}\frac{c}{e}p_i\left(\nabla\times\frac{\vec{b}}{B}\right)\cdot\nabla T_i=0 \quad (2.50)$$

2.1.4. Summary of Results

In the previous section various different approximation have been examined. The only equation left out is the one for the parallel motion which is simply resumed by projecting eq.2.13 on the parallel direction. Some terms can be neglected though. For a better description of the whole process we once more refer to [1].
The complete set of equation is therefore

$$\frac{\partial n}{\partial t}+\nabla\cdot(\vec{V}_{E\times B}+\vec{V}_{*,e}+\vec{V}_{\parallel,e})=0 \quad (2.51)$$

$$\frac{nc}{B\omega_i}\frac{d}{dt}(-\nabla_\perp^2\phi)+\frac{1}{3m_i\omega_i}\vec{b}\times\vec{\kappa}\cdot\nabla G_i+\nabla_\parallel\frac{j_\parallel}{e}+\nabla\cdot n(\vec{V}_{*,i}-\vec{V}_{*,e})=0 \quad (2.52)$$

$$m_e\frac{\partial^e V_{\parallel,e}}{\partial t}=-\frac{1}{n}\nabla_\parallel p_e-\frac{2}{3}\nabla_\parallel G_e+e\nabla_\parallel\phi-\frac{e}{c}\frac{\partial\psi}{\partial t}+e\frac{j_\parallel}{\sigma_\parallel}-0.71\nabla_\parallel T_e \quad (2.53)$$

$$m_i\frac{\partial V_{\parallel,i}}{\partial t}=-\frac{1}{n}\nabla_\parallel(p_i+p_e)-p_i\nabla\times\frac{\vec{b}}{\omega_i}\cdot\nabla V_{\parallel,i}-\frac{2}{3}\nabla_\parallel G_i \quad (2.54)$$

$$\frac{3}{2}n\frac{d^eT_e}{dt}+\frac{3}{2}n\vec{V}_{*,e}\cdot\nabla T_e+p_e\nabla\cdot\vec{V}_e-\frac{5}{2}\frac{c}{e}\nabla\cdot p_e\left(\frac{\vec{b}}{B}\times\nabla T_e\right)-0.71T_e\nabla_\parallel j_\parallel$$
$$-\nabla\cdot(\chi_\parallel\nabla_\parallel T_e)=0 \quad (2.55)$$

$$\frac{3}{2}n\frac{dT_i}{dt}+T_i\left[n\nabla\cdot\left(\vec{V}_{E\times B}+\vec{V}_{\parallel,e}\right)+\nabla\cdot\left(n\vec{V}_{*,e}\right)\right]+\frac{5}{2}\frac{c}{e}p_i\left(\nabla\times\frac{\vec{b}}{B}\right)\cdot\nabla T_i=0 \quad (2.56)$$

2.2. The GBS code

In line of principle the above equations 2.51-2.56 could be handled in a numeric code to obtain some results but some further simplifications will be taken into place

2.2.1. Some Mathematical Operators

Firstly, some new mathematical operators are introduced.

- Curvature Operator: This operator, $C(\cdot) = \frac{B}{2}\left(\nabla \times \frac{\vec{b}}{B}\right) \cdot \nabla(\cdot)$, emerges from terms in the form $\nabla \cdot (n\vec{V}_{*,e})$. It holds:

$$\nabla \cdot (n\vec{V}_{*,e}) = -\frac{c}{e}\left(\nabla \times \frac{\vec{b}}{B}\right) \cdot \nabla p_e - \frac{2c}{eB}C(p_e) \tag{2.57}$$

- Poisson brackets: This operator, $[\phi, \cdot] = \vec{b} \cdot (\nabla\phi \times \nabla(\cdot))$, is found in:

$$\nabla \cdot (n\vec{V}_{E\times B}) = c\nabla n \cdot \left(-\nabla\phi \times \frac{\vec{b}}{B}\right) + cn\nabla \cdot \left(\nabla\phi \times \frac{\vec{b}}{B}\right) = \frac{c}{B}[\phi, n] + \frac{2cn}{B}C(\phi) \tag{2.58}$$

- The subsequent term is treated as follow:

$$\nabla \cdot (n\vec{V_{\parallel,e}}) = \nabla n \cdot \vec{V_{\parallel,e}} + n\nabla \cdot \vec{V_{\parallel,e}} \simeq V_{\parallel,e}\nabla_\parallel n + n\nabla_\parallel V_{\parallel,e} \tag{2.59}$$

  In that way $\nabla \cdot \vec{b}$ term is neglected, with the finite aspect ratio effects. The outcomes due to finite aspect ratio are investigated in [42]

2.2.2. GBS Equations

In order to make more manageable the equations 2.51-2.55 some sort of adimensionalisation is needed. To not further complicate the notation, the same symbol is used for the dimensionless and dimensional quantity.

The dimensionless set of equation used in GBS is the following

$$\frac{\partial n}{\partial t} = -\frac{R}{B\rho_{s0}}[\phi, n] + \frac{2}{B}\left[nC(T_e) + T_e C(n) - nC(\phi)\right] - n\nabla_\parallel V_{\parallel,e} - V_{\parallel,e}\nabla_\parallel n + \mathcal{D}_n(n) + S_n \tag{2.60}$$

$$\frac{\partial \omega}{\partial t} + \tau\frac{\partial \nabla_\perp^2 T_i}{\partial t} = -\frac{R}{B\rho_{s0}}[\phi, \omega] - \tau\frac{R}{B\rho_{s0}}[\phi, \nabla_\parallel^2 T_i] - V_{\parallel,i}\nabla_\parallel\omega - \tau V_{\parallel,i}\nabla_\parallel\nabla_\perp^2 T_i + B^2\left[\nabla_\parallel(V_{\parallel,i} - V_{\parallel,e}) + (V_{\parallel,i} - V_{\parallel,e})\frac{\nabla_\parallel n}{n}\right] + \frac{B}{2n}C(G_i) + 2B\left[\tau C(T_i) + \tau\frac{T_i}{n}C(n) + C(T_e) + \frac{T_e}{n}C(n)\right] + \mathcal{D}_\omega(\omega) + S_\omega \tag{2.61}$$

$$\frac{\partial V_{\parallel,e}}{\partial t} + \frac{m_i}{m_e}\frac{\beta}{2}\frac{\partial \psi}{\partial t} = -\frac{R}{B\rho_{s0}}[\phi, V_{\parallel,e}] - V_{\parallel,e}\nabla_\parallel V_{\parallel,e} - \frac{m_i}{m_e}\frac{2}{3}\nabla_\parallel G_e + \frac{m_i}{m_e}\nabla_\parallel\phi + -\frac{m_i}{m_e}\nu(V_{\parallel,e} - V_{\parallel,i}) - \frac{m_i}{m_e}\frac{T_e}{n}\nabla_\parallel n - 1.71\frac{m_i}{m_e}\nabla_\parallel T_e + \mathcal{D}_{V_{\parallel,e}}(V_{\parallel,e}) + S_{V_{\parallel,e}} \tag{2.62}$$

$$\frac{\partial V_{\parallel,i}}{\partial t} = -\frac{R}{B\rho_{s0}}[\phi, V_{\parallel,i}] - V_{\parallel,i}\nabla_\perp V_{\parallel,i} - \frac{2}{3}\nabla_\parallel G_i - \nabla_\parallel T_e - T_e\frac{\nabla_\parallel n}{n} - \tau\nabla_\parallel T_i - \tau T_i\frac{\nabla_\parallel n}{n} + \mathcal{D}_{V_{\parallel,i}}(V_{\parallel,i}) + S_{V_{\parallel,i}} \tag{2.63}$$

$$\frac{\partial T_e}{\partial t} = -\frac{R}{B\rho_{s0}}[\phi, T_e] - V_{\parallel,e}\nabla_\parallel T_e + \frac{4}{3B}\left[\frac{7}{2}T_e C(T_e) + \frac{T_e^2}{n}C(n) - T_e C(\phi)\right] + \frac{2}{3}\left[T_e\left(0.71\nabla_\parallel V_{\parallel,i} - 1.71\nabla_\parallel V_{\parallel,e}\right) + 0.71T_e(V_{\parallel,i} - V_{\parallel,e})\frac{\nabla_\parallel n}{n}\right] + \mathcal{D}_{T_e}(T_e) + \mathcal{D}_{T_e}^{\parallel}(T_e) + S_{T_e} \tag{2.64}$$

$$\frac{\partial T_i}{\partial t} = -\frac{R}{B\rho_{s0}}[\phi, T_e] + \frac{4T_i}{3B}\left[C(T_e) + \frac{T_e}{n}C(n)\right] - \frac{4}{3B}T_i C(\phi) - \frac{2}{3}T_i\nabla_\parallel V_{\parallel,e} + \frac{2}{3}T_i(V_{\parallel,i} - V_{\parallel,e})\frac{\nabla_\parallel n}{n} - V_{\parallel,i}\nabla_\parallel T_i - \tau\frac{10}{3B}T_i C(T_i) + \mathcal{D}_{T_i}(T_i) + S_{T_i} \tag{2.65}$$

the details on the physical model for the giroviscous terms G_i, G_e and the source ones S_n, S_ω, $S_{V_{\parallel,e}}$, $S_{V_{\parallel,i}}$, S_{T_e}, S_{T_i} the parallel thermal diffusion $\mathcal{D}_{T_e}^{\parallel}$ and the numerical implementation of diffusion operators $\mathcal{D}_n(n)$, $\mathcal{D}_\omega(\omega)$, $\mathcal{D}_{V_{\parallel,e}}(V_{\parallel,e})$, $\mathcal{D}_{V_{\parallel,i}}(V_{\parallel,i})$, $\mathcal{D}_{T_e}(T_e)$, $\mathcal{D}_{T_i}(T_i)$ can be found in [23]. The diffusion operators $\mathcal{D}$ have been introduced in the code for numerical purposes.

The non-dimensionalization process has been resumed in table 2.3, reporting the reference values for each variable in equation 2.60-2.65

reference	normalised quantities
n_0	n
T_{e0}	T_e, T_i
$c_{s0} = \sqrt{T_{eo}/m_i}$	$V_{\parallel,e}$, $V_{\parallel,i}$, c_s
T_{e0}/e	ϕ
$\beta c m_i c_{s0}/(2e)$	ψ
R_0/c_{s0}	t
$\rho_{s0} = c_{s0}/\omega_i$	all perpendicular directions
R_0	all parallel directions

Table 2.3: List of reference quantities and the quantities adimensionalised with respect each reference, R_0 being the major radius and $\beta = \frac{8\pi n_0 T_{e0}}{B^2}$ the compression ratio. Please note that for what concerns temperature and density, reference quantities are arbitrary

Moreover, in equation 2.62 the adimensionalised resistivity has been introduced:

$$\nu = \frac{e^2 n_0 R_0}{m_i \sigma_{\parallel} c_{s0}} \tag{2.66}$$

and the ion to electron temperature ratio in equations 2.61, 2.63, 2.65:

$$\tau = \frac{T_{i0}}{T_{e0}} \tag{2.67}$$

and the curvature operator (§ 2.2.1) is redefined multiplied by R_0 to keep it dimensionless.

As every differential equation, also 2.60-2.65 need some boundary and initial conditions. Since the tokamak is an axial-symmetric machine, in the toroidal direction ,a periodic boundary condition it is imposed. Moreover, because of the 3-D nature of the simulation, no boundary conditions are needed in the poloidal direction of the edge or the core. For what concern the SOL, some complex boundary conditions apply where the magnetic surface touches the wall. A complete treatment of them can be found in [23, 25]. On the temporal domain, instead the initial conditions are some arbitrary reasonable ones for a tokamak. Such approach is implemented because the simulations are run until the average field values reaches a stationary condition.

2.2.3. Simulations Geometry

It is worth to analyse in some details the geometry in which the analysis takes place. The thesis studies the behaviour of a plasma shaped in a topological solid torus throughout magnetic fields. This reflects into the model in the operator which have an explicit

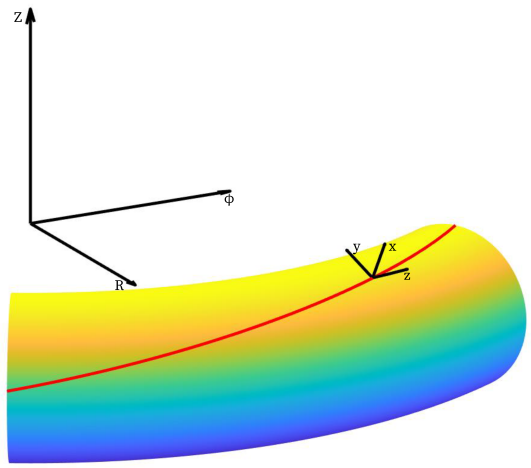

Figure 2.1: Portion of a toroidal surface with circular section. The two reference system [y,x,z] and [R,Φ,Z] are highlighted. The red line is a field line which wrap around the toroidal magnetic surface.

dependence on the magnetic field. Because of the tokamak design the magnetic field is in first approximation axial symmetric, our space of interest delimited by some surface obtained by revolving some closed line around the central vertical axis. The derivation of this shape will be part of this thesis's work. Since the focus is on the behaviour of edge region which is within the LCFS, the confinement design, both throughout a limiter or a divertor, does not affect the results. It is not worth, then, to analyse this detail further. Two different reference system will be used, mainly a right-handed local coordinate system [y, x, z], and a cylindrical right-handed coordinate system, noted with [R, Φ, Z]. x-coordinate is the flux coordinate i.e. in a circular configuration the radial direction, z is aligned with the toroidal direction and finally y is perpendicular to both x and z (figure 2.1). In the large aspect ratio limit the (x,y) plane correspond to the poloidal one. The [R, ϕ, Z] reference system is instead a right-handed cylindrical system, with Z direction aligned with the vertical axis, R the radial coordinate, and Φ the angle between the point and a given direction. This reference system is mainly useful to handle geometrical operators: curvature operator C and parallel gradient $\nabla_{\|}$.

2.2.4. Ballooning Mode

An important instability that is studied in this thesis is the so-called Ballooning Mode. It is an instability driven by the bad curvature region. For such a region is usually meant the portion of magnetic surface where it holds $\vec{\kappa}\cdot\nabla n < 0$. The phenomenon is driven unstable by the presence of collision in plasma, i.e. a finite resistance or by a finite electronic mass [44]. The instability is mainly governed by the diamagnetic electronic velocity and the $E \times B$ drift (§ 2.1.3).

$$\vec{V}_{*,e} = \frac{c}{en}\nabla \times \frac{p_e\vec{b}}{B} - 2\frac{cT_e}{eB}\vec{b} \times \vec{\kappa} \tag{2.68}$$

$$\vec{V}_{E\times B} = \frac{c}{B}(-\nabla\vec{\phi}\times \vec{b}) \tag{2.69}$$

Both velocities appear in the continuity equation (equation 2.60) in the form of $\nabla \cdot (n\vec{V})$ determining the local variation of the electron particle density. Therefore, the first component of equation 2.68 has any influence on the instability being described now. The second term, au contraire, advects the electrons in a direction perpendicular to both $\vec{b}$[3] and $\vec{\kappa}$. In presence of a density perturbation the divergence is not null and some charge separation arises, due to the electrons accumulating in some regions and leaving in some other unbalanced positive charges due to the ionic background. Following the build-up of charge separation an electric potential develops and therefore an electric field. The particles are finally advected by the $E \times B$ drift. If this last has the same direction of the density gradient the phenomenon is unstable, since the advected particles will increase even more the original perturbation. The mode is instead damped down if $\vec{\kappa} \cdot \nabla n < 0$. This, as a matter of fact, splits the tokamak in two areas, the high field zone, characterised by a dumped Ballooning Mode and the low field zone where the opposite happens.
As it has been said before there are two main branches, the resistive one (RBM), in which is the plasma collisionality that cause a non-zero shift between the density and potential perturbation's phases, and the inertial (InBM) one, in which is caused by the finite electron mass. It should be said, for completeness, that a third branch can be present. This last is called ideal Ballooning Mode (IdBM) and it is characterised by a β high enough to let electromagnetic effect to bend magnetic lines.
Anyway, along this work the focus will be on the resistive branch.

[3]As a remark it is useful to remember that $\vec{b}$ is the total magnetic field versor, i.e. $\vec{b} = \frac{\vec{B}}{B}$, including therefore also the toroidal magnetic field and being essentially in the toroidal direction.

2.3. Previous Studies on Periphery Dynamics

Since 1990s large efforts has been carried to study turbulent regime in tokamak edge as by Scott [39, 40], Rogers [2, 36] and Zeiler [1]. Using a similar set of equation derived from Braginiskii model they studied competition between different regimes: the two branches of ballooning mode (§ 2.2.4) resistive and ideal, and ion temperature gradient induced modes. In 2014 an enhanced analysis has been performed by Mosetto [25].
Scott inspected edge turbulence as the result of transfer of energy provided by a free energy source to the sinks [40]. The free energy source has been identified in the background pressure gradient advected by E×B drift and the dissipative sinks in the resistive current dumping at small scales.
Rogers et al. studied the edge turbulence as the competition of fore-mentioned regimes, trying to find the parametric subspaces in which one regime prevails on the other.
Both authors identified similar dimensionless control parameters. Among them it is worth to mention one taking into account β parameter ($\beta = (8\pi n T_e)/B^2$), and one resuming the effect of electron-ion collisions and the importance of adiabatic coupling.
It is valuable to stress that in the mentioned work pressure gradient is set a priori when numerical simulations are performed. Besides in experimental applications pressure gradient length is the self-consistent result of the interplay between all phenomena occurring in plasma.
Mosetto further investigate those aspects, elaborating a numerical theory to evaluate which ballooning mode or drift branch wave emerge and their interplay, sorting a set of parameters. Despite this analysis is carried in a circular limited geometry its analysis overcame self-consistency of pressure gradient problem, allowing to describe dependency of R/L_n over the space parameters.

3 | The Linear Solver

The chapter will provide a discussion of how you can apply the GBS code in a linear context.
Firstly, the mathematical problem is settled (§ 3.1). After the equations linearisation (§ 3.1.1), the arise of an eigenvalue problem is outlined (§ 3.1.2) and the way to treat it numerically is investigated (§ 3.1.3). At the end of the section a way to evaluate the poloidal wave-vector is proposed (§ 3.1.4).
In a second moment, the field line discretisation is tackled (§ 3.2), with particular attention to the physical basis (§ 3.2.1). At the end a brief display of the four magnetic configurations used in this work is presented (§ 3.3).

3.1. The linear GBS code

3.1.1. Linearisation

To perform a linear analysis the set of equations 2.60-2.65 must be linearised. In such form the equations can be handled throughout a linear solver.
So that such proceeding could be performed, operator's dependence on coordinates must be made explicit. The coordinates used in this chapter and in chapter 4 are the ones clarified in section 2.2.3, more precisely, the local reference system, [y,x,z]. However, operators' dependence on magnetic field will be written as a function of the magnetic field components in both [y,x,z] and the cylindrical reference system [R,Φ,Z].
The linearisation is carried out by a first order perturbation scheme. For each variable it will be assumed to correspond, in fist approximation, to an equilibrium value plus a first order perturbation. For every field f^* in equations 2.60-2.65 it is assumed that $f^* = f_0 + f$ where f_0 is the equilibrium field, i.e. the equilibrium that solve the system 2.60-2.65 when the time derivative is null. As it is usually done in perturbation theory, it is assumed that $f \ll f_0$.
It is assumed that the equilibrium for n e T_e can be described as $f_0 = f_{00}(1 + x/L_f)$, the Taylor polynomial of exponential function. Since it is a dimensionless value, it holds that

$f_{00} = 1$ if the reference in tab. 2.3 is chosen to be coincident to the equilibrium value. We will assume that from now on. For all the other fields, equilibrium value is null. In this work, in linear framework, it has been also assumed the cold ion limit. The underlying hypothesis states that ion temperature is negligible with respect electron one. Therefore $\tau = 0$ in equation 2.67, $T_i \sim 0$ and equation 2.65 reduce to a tautology. Therefore, only five equations are needed to describe the whole plasma. It is finally worth to recall that, since we are working in infinite aspect ratio, i.e. $\varepsilon = \mathrm{a}/R \to 0$ the distance from the magnetic axis R does not vary and therefore in can be confused with the tokamak major radius R_0 and treated as a constant.

$$\frac{\partial n}{\partial t} = \frac{R}{L_n}\frac{\partial \phi}{\partial y} + \frac{2}{B}\hat{C}(T_e) + \frac{2}{B}\hat{C}(n) - \frac{2}{B}\hat{C}(\phi) - \nabla_\parallel V_{\parallel,e} \tag{3.1}$$

$$\frac{\partial}{\partial t}(\nabla_\perp^2 \phi) = 2B[\hat{C}(T_e) + \hat{C}(n)] + B^2(\nabla_\parallel V_{\parallel,i} - \nabla_\parallel V_{\parallel,e}) \tag{3.2}$$

$$\frac{\partial}{\partial t}\left(\frac{m_e}{m_i}V_{\parallel,e} + \frac{\beta}{2}\psi\right) = -\nabla_\parallel n + \nabla_\parallel \phi - 1.71\nabla_\parallel T_e + \nu(V_{\parallel,i} - V_{\parallel,e}) \tag{3.3}$$

$$\frac{\partial V_{\parallel,i}}{\partial t} = -\nabla_\parallel n - \nabla_\parallel T_e \tag{3.4}$$

$$\begin{aligned}\frac{\partial T_e}{\partial t} = \eta\frac{R}{L_n}\frac{\partial \phi}{\partial y} + \frac{4}{3B}\left[\frac{7}{2}\hat{C}(T_e) + \hat{C}(n) - \hat{C}(\phi)\right] \\ + \frac{2}{3}0.71(\nabla_\parallel V_{\parallel,i} - \nabla_\parallel V_{\parallel,e}) - \frac{2}{3}\nabla_\parallel V_{\parallel,e}\end{aligned} \tag{3.5}$$

Where $\eta = \frac{L_n}{L_{T_e}}$ and $\hat{C}$ is the adimensionalised linear curvature operator. If β is not null, to close the system, since six variables are present, (n, T_e, ϕ, ψ, $V_{\parallel,e}$, $V_{\parallel,i}$), Ampère equation 2.46 is used.

$$\nabla_\perp^2 \psi = -V_{\parallel,e} \tag{3.6}$$

Here both ψ and $V_{\perp,e}$ as the operator are in the adimensionalised and the equation has been linearised. This allows us to reduce the unknown fields to five. A complete derivation of equations 3.1-3.5 can be found in [25]. Moreover, according to non-local, linear theories of curvature driven modes ([28], [35]), the turbulence in radial direction develops less than in poloidal direction since holds that $\frac{k_y}{k_x} \sim \sqrt{k_x L_p} \gg 1$. Is possible then to ignore radial mode dependence assuming $k_y \gg k_x$.

Because the x direction is negligible with respect to the other directions, the work develops only on the toroidal surface defined by the two variables (y,z). Therefore is finally possible to evaluate the geometric operators: the curvature operator

$$\hat{C} = \frac{B_Z(y)}{B_y(y)}\frac{\partial}{\partial y} = \frac{b_Z(y)}{b_y(y)}\frac{\partial}{\partial y} \tag{3.7}$$

the perpendicular laplacian:

$$\nabla_{\perp}^2 = \frac{\partial^2}{\partial y^2} \tag{3.8}$$

and the parallel gradient:

$$\nabla_{\parallel} = \frac{b_y(y)}{R}\frac{\partial}{\partial y} + \frac{\partial}{\partial z}. \tag{3.9}$$

In equations 3.7-3.11 B_i is the total magnetic field's component in i-th direction, b_i is the same component but normalised with respect to the magnetic field itself. Please note that in large aspect ratio, if the safety factor q is kept finite, the ratio between the poloidal and the toroidal field is small, i.e. $B_p/B_t = b_y = \varepsilon/q$.

3.1.2. The Eigenvalue Problem

Since x direction is negligible with respect to the other directions the linear analysis is carried on a two-dimensional manifold, described by the dimensionless coordinates [y,z]. Since R in large aspect ratio is a constant the adimensionalised coordinate z spans in the interval [0,2π], being oriented in the toroidal direction. The perpendicular direction, the poloidal one, instead, is described by y. Since the work takes place in the edge region, magnetic surfaces are closed and y is also periodic with period L_y, the length of the magnetic surface cross section.
To assure periodicity it has been chosen to carry a spectral analysis on the toroidal direction, i.e. to assume the perturbation

$$f(y, z, t) \propto e^{-in_z z} \tag{3.10}$$

Here i is the imaginary unit. This is enforced by Fourier theorem, stating that any periodical function can be written as the sum of complex exponential functions, each with an imaginary argument. Fourier theorem states also that the wave-number n_z must be an integer number. Being the equations 3.1-3.5 linear, the solution for any linear combination of toroidal modes is the linear combination of the solution for each mode. Therefore, it has been chosen to analyse each toroidal mode separately. Moreover, being the equation invariant for any angular displacement, the solution is undetermined up to a phase value in z. For this reason, it has been decided to choose the phase in such a way f(y,z,t) is even in the z direction. For that we will limit the analysis for positive values of n_z, the opposites leading to same results. The minus sign in the argument in equation 3.10 has been chosen for convenience.
It view of definition 3.10 it is possible to write the parallel gradient stated in 3.9 in its

final form:

$$\nabla_{\parallel} = Rb_y(y)\frac{\partial}{\partial y} - in_z \tag{3.11}$$

It is not possible to apply for y coordinate the procedure implemented for z coordinate, since the equations 3.1-3.5 are not linear in y for. The presence of the geometrical operators that depend on y themselves, indeed, spoils this property.
We assume, also, separability for the spatial and temporal variables. What it is therefore retrieved is that

$$f(y,z,t) \propto e^{\tilde{\gamma}t} \tag{3.12}$$

Since the z_ϕ eigenfunctions has been allowed to be a complex value, the same condition must be granted for the temporal one, this last resumed in $\tilde{\gamma} \in \mathbb{C}$. Inspecting equation 3.12, it is possible to assign a physical meaning to $\tilde{\gamma}$ real and imaginary part. $\gamma = \Re(\tilde{\gamma})$ is called mode growth rate and determine the exponential growth of this last. On the opposite, $\omega = \Im(\tilde{\gamma})$ is the pulsation of the mode and describe its temporal oscillation. The final expression for any perturbation field is therefore

$$f(y,z,t) = f(y)e^{\tilde{\gamma}t - in_z z} \tag{3.13}$$

The linear problem 3.1-3.5 can be therefore reduced to the eigenproblem:

$$\tilde{\gamma}n = \frac{R}{L_n}\frac{\partial \phi}{\partial y} + \frac{2}{B}\hat{C}(T_e) + \frac{2}{B}\hat{C}(n) - \frac{2}{B}\hat{C}(\phi) - \nabla_{\parallel}V_{\parallel,e} \tag{3.14}$$

$$\tilde{\gamma}\nabla_{\perp}^2\phi = 2B[\hat{C}(T_e) + \hat{C}(n)] + B^2(\nabla_{\parallel}V_{\parallel,i} - \nabla_{\parallel}V_{\parallel,e}) \tag{3.15}$$

$$\tilde{\gamma}\left(\frac{m_e}{m_i}V_{\parallel,e} + \frac{\beta}{2}\psi\right) = -\nabla_{\parallel}n + \nabla_{\parallel}\phi - 1.71\nabla_{\parallel}T_e + \nu(V_{\parallel,i} - V_{\parallel,e}) \tag{3.16}$$

$$\tilde{\gamma}V_{\parallel,i} = -\nabla_{\parallel}n - \nabla_{\parallel}T_e \tag{3.17}$$

$$\begin{aligned}\tilde{\gamma}T = \eta\frac{R}{L_n}\frac{\partial\phi}{\partial y} + \frac{4}{3B}\left[\frac{7}{2}\hat{C}(T_e) + \hat{C}(n) - \hat{C}(\phi)\right] \\ + \frac{2}{3}0.71(\nabla_{\parallel}V_{\parallel,i} - \nabla_{\parallel}V_{\parallel,e}) - \frac{2}{3}\nabla_{\parallel}V_{\parallel,e}\end{aligned} \tag{3.18}$$

Problem 3.14-3.18 is a one-dimensional functional eigenproblem admitting in general a countable infinity of eigensolutions and eigenvalues because of the periodicity and nonlinear dependence on y and the temporal evolution of the n_z-th mode is a linear combination of each eigensolutions. By denoting $\gamma = \max_j(\gamma_j)$, where γ_j is the real part of the j-th eigenvalue, the asymptotic temporal z-mode's behaviour is characterised by a growth-rate γ. In this way, it is possible to associate to each z-mode a single value of growth-rate γ. The y dependence can be retrieved by looking at the eigenfunction corresponding to the

picked eigenvalue.
However, the problem is solvable provided that a null average condition on ϕ is imposed, to allow the invertibility of the perpendicular laplacian in periodic boundary conditions.

3.1.3. Linear Solver Discretization and Solution Methods

In precise algebra eigenproblem 3.14-3.18 would be a functional analysis problem but would be hardly handled by a computer.
To overcame this issue, it has been opted for a discrete approach. Assuming to have an evenly spaced grid for the y-direction, it is possible to approximate the exact solution of perturbed fields to the value they assume on each grid point. The vector $\vec{x} = [n_1, \dots, n_{N_y}, \phi_1, \dots, \phi_{N_y}, \psi_1, \dots, \psi_{N_y}, T_{e,1}, \dots, T_{e,N_y}, V_{\parallel,i,1}, \dots, V_{\parallel,i,N_y}]$ is introduced as the one containing the values of the different fields on the grid points. For stability purposes two grids are used [25]: an unshifted grid where n_j, ϕ_j, $T_{e,j}$ are evaluated, and a shifted grid on which $\psi_j, V_{\parallel,i,j}$ and $V_{\parallel,e,j}$ are defined.
The differential operators in the y direction, instead, can be approximated throughout a finite differences scheme to the matrix $D^{y,k}_{\alpha,\beta}$ according to the expression:

$$\frac{\partial^k f^*}{\partial y^k}|_{y=y_{\beta,i}} \simeq [D^{y,k}_{\alpha,\beta}\vec{f}_\alpha]_i \tag{3.19}$$

where $\vec{f}$ is a vector discretizing any L_y-periodic function f^* on N_y evenly spaced points. The k superscript is the order of the derivative. The subscripts, instead describes the grid we are working on. In $D^{y,k}_{\alpha,\beta}$ notation, therefore, α represent the grid to which the derived vector f_α belongs, β the grid on which the derivative is evaluated through y_β. All derivatives are square matrices $N_y \times N_y$ since the grid is periodic and present non null elements in the first p/2 upper and lower diagonals and in the upper-right and the lower-left corner where the periodicity conditions apply.

The other operators are built according to their definition. It must be noted that parallel gradient $D^{\parallel,1}$ and curvature $\hat{C}$ present a dependence on y. This is obtained by multiplying each row of the matrix $D^{y,1}_{\alpha,\beta}$ by the corresponding coefficient, consistently with the finite difference scheme and its definition. It holds, then:

$$[D^{\parallel,1}_{\alpha,\beta}]_{i,j} = \frac{1}{R} b_y(y_{\beta,i})[D^{y,1}_{\alpha,\beta}]_{i,j} - in_z[\mathbb{1}_{\alpha,\beta}]_{i,j} \tag{3.20}$$

and

$$[\hat{C}_{\alpha,\beta}]_{i,j} = \frac{b_Z(y_{\beta,i})}{b_y(y_{\beta,i})}[D^{y,1}_{\alpha,\beta}]_{i,j}. \tag{3.21}$$

where $\mathbb{1}_{\alpha,\beta}$ is the interpolation matrix between the two grid α and β and the first subscript of $y_{\beta,i}$ points out the grid on which the magnetic field is evaluated.

It is then possible to summarise equations 3.14-3.18 in symbolic form:

$$\gamma L\vec{x} = M\vec{x} \tag{3.22}$$

with

$$L = \begin{bmatrix} \mathbb{1}_{u,u} & 0_{u,u} & 0_{s,u} & 0_{u,u} & 0_{s,u} \\ 0_{u,u} & D^{y,2}_{u,u} & 0_{s,u} & 0_{u,u} & 0_{s,u} \\ 0_{u,s} & 0_{u,s} & (\frac{m_e}{m_i}L^{em}_{s,s} + \frac{\beta}{2}\mathbb{1}_{s,s}) & 0_{u,s} & 0_{s,s} \\ 0_{u,u} & 0_{u,u} & 0_{s,u} & \mathbb{1}_{u,u} & 0_{s,u} \\ 0_{u,s} & 0_{u,s} & 0_{s,s} & 0_{u,s} & \mathbb{1}_{s,s} \end{bmatrix} \tag{3.23}$$

and

$$M = \begin{bmatrix} 2\hat{C}_{u,u} & \frac{R}{L_n}D^{y,1}_{u,u} - 2\hat{C}_{u,u} & -D^{\parallel,1}_{s,u}L^{em}_{s,s} & 2\hat{C}_{u,u} & 0_{u,u} \\ 2\hat{C}_{u,u} & 0_{u,u} & -D^{\parallel,1}_{s,u}L^{em}_{s,s} & 2\hat{C}_{u,u} & D^{\parallel,1}_{s,u} \\ -D^{\parallel,1}_{u,s} & D^{\parallel,1}_{u,s} & -\nu\mathbb{1}_{s,s}L^{em}_{s,s} & -1.71D^{em}_{u,s} & \nu\mathbb{1}_{s,s} \\ \frac{4}{3}\hat{C}_{u,u} & \eta\frac{R}{L_n}D^{y,1}_{u,u} - \frac{4}{3}\hat{C}_{u,u} & -0.71\frac{2}{3}D^{\parallel,1}_{s,u}L^{em}_{s,s} & \frac{14}{3}\hat{C}_{u,u} & 0.71\frac{2}{3}D^{\parallel,1}_{s,u} \\ -D^{\parallel,1}_{u,s} & 0_{u,s} & \frac{\beta}{2}\frac{R}{L_n}(1+\eta)D^{y,1}_{s,s} & -D^{y,1}_{s,s} & 0_{s,s} \end{bmatrix} \tag{3.24}$$

In the matrices $\mathbb{1}_{u,u}$ and $\mathbb{1}_{s,s}$ are the identity matrix, 0 the empty one.
The $L^{em}_{s,s}$ notation allow to switch from ψ to $V_{\parallel,e}$ without changing the whole structure of M matrix. As a matter of fact, ψ appear in equation 2.53 only if $\beta \neq 0$. Therefore, $L^{em}_{s,s} = -D^{y,2}_{s,s}$ when $\beta \neq 0$, making possible to insert naturally the Ampère equation closure 3.6 in the solver. Otherwise, for a null compression ratio, the closure is not needed anymore since ψ do not appear in the resolved set of equations. Therefore it is possible to let $L^{em}_{s,s} = \mathbb{1}_{s,s}$ [25].

It must be noted that a little change in the matrices is needed to allow inversibility of L. As a matter of fact, periodic laplacian is not invertible. For that a zero average condition is imposed on ϕ. To implement it the N_y-th line in L and M operators are replaced respectively with the lines

$$[\underbrace{0,\dots,0}_{N_y},\underbrace{1,\dots,1}_{N_y},\underbrace{0,\dots,0}_{3N_y}]$$

$$[\underbrace{0,\dots,0}_{5N_y}]$$

To solve the 3.22, remembering that it is the discrete problem of 3.14-3.18, it can be

solved addressing it as a generalised eigenvalue problem. The generalised eigenvalue of the matrix M with respect to L with the maximum real part is evaluated as the growth-rate of the mode taken into account. The corresponding eigenvalue, generally complex, is then the discretization for the perturbation of the different field along y.

Another way to address the problem is throughout the so called Θ-method [31], remembering that the equation 3.22, we are trying to solve, firstly derives from 3.1-3.5. Therefore, it is treated as a PDE, with a time advancing scheme. The initial values are assessed randomly and then gamma is evaluated as

$$\gamma_{i,t} = \frac{1}{\Delta t} \log \left| \frac{x_{i,t}}{x_{i,t-1}} \right| \tag{3.25}$$

The resolving scheme is

$$\vec{x}_{t+1} = \vec{x}_t + \Delta t[(1-\Theta)L^{-}1M\vec{x}_t + \Theta L^{-1}M\vec{x}_{t+1}] \tag{3.26}$$

where t describe the time step advancing. If $\Theta = 0$ the method is fully explicit, and implicit otherwise. If $\Theta = 1/2$ the scheme is second order convergent in time [31], first order otherwise. We will use mainly the first approach to get result and the second one to confirm them or as a diagnostic tool.

3.1.4. Poloidal Wave-Vector Evaluation

As it has been said in previous subsection 3.1.2, the general eigensolution of problem 3.14-3.18 is not characterised by a well-defined k_y. As will be treated in chapter 4, however, k_y is an important parameter in the study of the tokamak transport properties. Therefore, it would be desirable to have a way to evaluate it anyway. Clearly, such method must reduce to the proper wave-vector if the eigenvalue is a sinusoidal function.
In the present work it has been assumed the perturbation k_y to be evaluated through an integral mean. The Fourier transform of problem 3.14-3.18's eigenfunction corresponding to the maximum growth rate is taken. Then, the first momentum of Fourier transform's absolute value is used to evaluate the averaged k_y. It is assumed, then, that the chosen component has a normalised Fourier Transform, i.e. $\int_0^{+\infty} |\mathcal{F}\{\psi\}(k)|dk = 1$. This does not lack in generality since the eignesolutions are defined up to a multiplicative constant. For convention, in this work, it will be used the ϕ component of the whole eigenvalue

$[n, \phi, \psi, V_{\parallel,i}, T_e]$ to the evaluation of k_y. Therefore

$$k_y = \int_0^{+\infty} k|\mathcal{F}\{\psi\}(k)|dk \tag{3.27}$$

This is easily transposed to the discrete approximation described in subsection 3.1.3 substituting the Fourier transform $\mathcal{F}\{\cdot\}$ with the discrete Fourier transform $\mathcal{F}_D\{\cdot\}$ and the integration process with a trapezoidal numerical integration.

3.2. Field Lines Disctetisation

In previous subsection, 3.1.3 it has been assumed the existence of a grid discretizing the y direction. Because of the definition of y, the grid discretizes also the magnetic surfaces' poloidal cross section. In subsection 1.3 it has been briefly recalled that shaping is the effect obtained through additional coils placed horizontally and it consists in the plasma cross section and the magnetic surfaces taking some sort of shape different from the circular one. The obtained shape mostly depends on the external coils, notably on their position and on the amount of current that flows through them. Those parameters, naturally, must be made explicit as inputs. The choice that has been made is to request the position with respect to the plasma current centre and the relative current intensity magnitude with respect to the plasma current flowing in the machine.
For what concerns the plasma current some important assumptions have been allowed. Firstly, the plasma current density has been estimated as proportional to a circular gaussian distribution. This is mainly due to avoid divergences in the magnetic field in proximity of the plasma current. This hypothesis is reasonable and sufficiently supported by experimental shots [7, 9] and is adequately effortless to handle analytically. The circularity assumption is a bit more subtle but is still legitimate: the most of the current, because of the density radial dependence, flows in the core, this last being the region less influenced by the shaping effects.

Secondly the position of the plasma current's centre has been assumed fixed with respect to the external shaping coils. This is not true in general, since it depends on the self-consistent equilibrium that establishes. For sake of simplicity the magnetic axis it assumed fixed. Said that, once specified the intensity of the plasma current and the typical length for the gaussian dependence the plasma current is completely characterised. It is worth to notice that the plasma current intensity is redundant and not necessary for the magnetic surfaces' evaluation, since scaling all the currents the same magnetic surfaces

are obtained. Instead, they are essential for the poloidal magnetic field, evaluated for the curvature and parallel gradient operators (equations 3.7, 3.11).
With all the above-mentioned parameters on plasma current and coil filaments it is possible to assemble the complete structure of nested magnetic surfaces. A last information must be provided: a point belonging to the surface itself. In that way the working space is determined uniquely.

3.2.1. Physical Basis of Grid and Magnetic Field Definition

With all those information it is possible to evaluate magnetic surfaces. Starting from MHD it is possible to state that magnetic surfaces are also characterised by a constant value of the flux function Ψ, a field related to the magnetic poloidal field through the dimensional equation:

$$\vec{B_p} = \frac{1}{R}\nabla\Psi \times \vec{e}_\phi \tag{3.28}$$

where ϕ is the poloidal direction and $\vec{e}_\phi$ the versor oriented positively with respect to it. For a more complete treatment it is possible to refers to A.
As stated in subsection 2.2.3 the work takes place in large aspect ratio. This means that it is possible to reduce the expression of the magnetic field produced by a coil into the one of an infinitely long filament, an analytic well know result given by the Ampère law:

$$\vec{B}_p = \frac{2I_T}{c\sqrt{(R-R_0)^2+(Z-Z_0)^2}}\vec{e}_\alpha \tag{3.29}$$

where I_T is the current flowing in the filament and (R_0, Z_0) is the filament position. In equations 3.29 and 3.30 the α direction is the one perpendicular to the radius $(R-R0, Z-Z0)$ in the RZ plane, positive in counter-clockwise direction.
For a gaussian-distributed current, instead, the expression is somehow more complicated but it can still be expressed as:

$$\vec{B}_{p,gauss} = \frac{2I_T}{c\sqrt{(R-R_0)^2+(Z-Z_0)^2}}\left(1-e^{-\frac{(R-R_0)^2+(Z-Z_0)^2}{2a_g^2}}\right)\vec{e}_\alpha \tag{3.30}$$

It is therefore possible to write the flux function of the whole system.

$$\Psi(R,Z) = \frac{A}{2}\left[\log(R^2+Z^2) + \mathrm{Ei}\left(\frac{R^2+Z^2}{2a_g^2}\right) + \sum_{j=1}^{N} I_j \log((R-R_j)^2+(Z-Z_j)^2)\right] \tag{3.31}$$

Here A resumes a coefficient proportional to the flowing current, a_g is the gaussian attenuation length, (R_j, Z_j) are the coordinates of the j-th current filament and I_j is its relative intensity with respect to the plasma current.

Once such a function is built, it is possible to determine numerically the contour on which it hold the condition

$$\Psi(R,Z) = \Psi(P_0) = \Psi_0 \tag{3.32}$$

P_0 being the expressed point in order to define uniquely the magnetic surface. The numerical discretisation is carried out in order to have evenly spaced points in the grid.
In that way the code is able to produce two vectors containing the R and Z coordinate of each grid point and a third one displaying the value of the curvilinear abscissa, coinciding with the value of y in the local reference system. Variable's origin has been chosen to lay in where the curve meets the HFS mid-plane.

The values of R and Z also allow to evaluate the magnetic field along the curve. Those values are needed to compute the geometrical operators: the curvature $\hat{C}$ (equation 3.7) and the parallel gradient $\nabla_\parallel$ (equation 3.11). The magnetic poloidal field is assessed with the same approach of Ψ, i.e. the sum of the different analytical solutions for infinite current wires translated in the filament position.

$$b_R(R,Z) = -A\left(1 - e^{-\frac{R^2+Z^2}{a_g^2}}\right)\frac{Z}{R^2+Z^2} - A\sum_{j=1}^{N} I_j \frac{Z-Z_j}{(R-R_j)^2+(Z-Z_j)^2} \tag{3.33}$$

$$b_Z(R,Z) = A\left(1 - e^{-\frac{R^2+Z^2}{a_g^2}}\right)\frac{R}{R^2+Z^2} + A\sum_{j=1}^{N} I_j \frac{R-R_j}{(R-R_j)^2+(Z-Z_j)^2} \tag{3.34}$$

Clearly, since we have imposed a scalar condition (equation 3.32) in a two-dimensional space, the analysis takes place on a one-dimensional variety. R and Z are a function of the curvilinear abscissa y and so b_R and b_Z do.
It is finally possible to evaluate also b_y, simply as the 2-norm of the $\vec{b_p} = (b_R, b_Z)$ vector in

the RZ space. It is possible to do this, since the local coordinate system is defined in such a way that y is always parallel to the magnetic field (§ 2.2.3). Therefore, its component is equal to the modulus since the poloidal magnetic vector is always directed in y direction.

$$b_y(y) = ||\vec{b}(y)||_2 = \sqrt{b_R^2(y) + b_Z^2(y)} \tag{3.35}$$

It is worth to recall that those expressions are coincident to the poloidal magnetic field ones. As a matter of fact, since we are using adimensionalised variables, the b parameters correspond numerically to the various poloidal magnetic field's components $B_{p,i}$, since $\vec{b} = \frac{\vec{B}_p}{B} \sim \frac{\vec{B}_p}{B_T}$ and the reference value is the toroidal field, its dimensionless value being one.

3.3. Magnetic Configurations

In this last section the four configuration used in the simulation work to study the plasma instabilities are made explicit with all their parameters.

3.3.1. Circular Configuration

In circular configuration the plasma current alone is sufficient to create the magnetohydrodinamic equilibrium, since no shaping is present. In figure 3.1 it can be appreciated that, as a result of the absence of other shaping filaments, all lines are closed and there is no X-point. The LCFS corresponding to the first surface intersecting the wall.

Here below the main parameters used for Circular configuration in this work are listed in table 3.1.

	Parameters
R_j	$[\,-\,]$
Z_j	$[\,-\,]$
I_j	$[\,-\,]$
A	$250/33$
a_g	$25/\sqrt{2}$
P_0	$[\,100\,,\,0\,]$

Table 3.1: Summary of the parameter used to build the Circular configuration

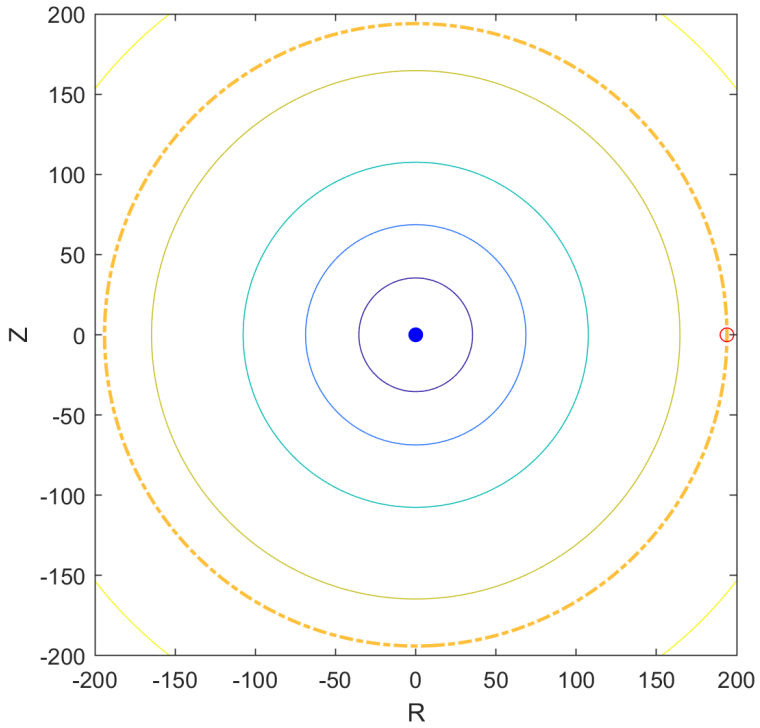

Figure 3.1: Circular magnetic configuration. In the picture the plasma current is denoted by a circular blue dot, the point $P0$ through a void red circlet. The thick dashed line is the cross section of the magnetic surface on which simulations are run. The thinner coloured lines are other magnetic surfaces' sections.

3.3.2. X-Point Configurations

Null triangularity

In this configuration, that in this work will be named Global Symmetric (GS), a current is inserted with the aim to shape the plasma. Since the coil is centred it has not a triangularity effect. It causes, instead, a variation on the safety factor q along the field line. As a matter of fact, since $q = \frac{a}{Rb_y}$ and b_y goes quickly to zero in the proximity of the X-point, q increases sharply when it passes through the bottom of the magnetic surface. Since in MHD q is defined as $q = \frac{d\theta}{d\phi}$ the number of toroidal turns per poloidal turns peaks sharply as q upturns and then the magnetic field line stays more recurrently in lower part of the tokamak. The global symmetric configuration is displayed in figure 3.2.

Here below main parameters used for Global Symmetric configuration in this work are listed in table 3.2.

	Parameters
R_j	[0]
Z_j	[−664]
I_j	[0.72]
A	23
a_g	90
P_0	[190 , 0]

Table 3.2: Summary of the parameter used to build the Circular configuration

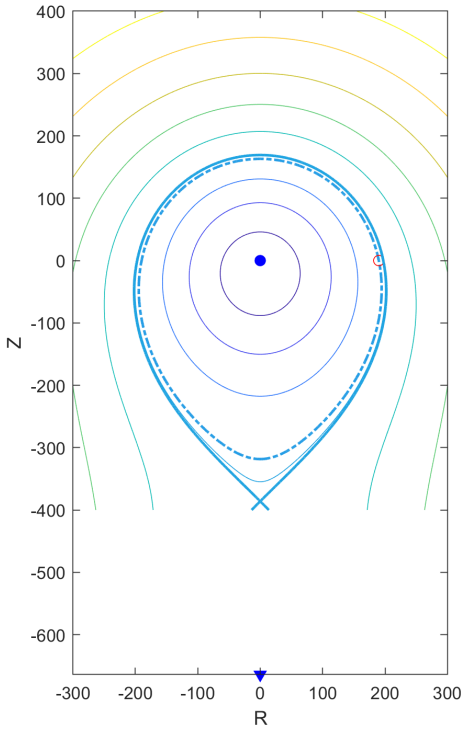

Figure 3.2: Global Symmetric configuration. In the picture the plasma current is denoted by a circular blue dot, current filament is flagged by a blue triangle, the point $P0$ through a void red circlet. The thick dashed line is the cross section of the magnetic surface on which simulations are run. The thinner coloured lines are other magnetic surfaces' sections. The separatrix is stressed through a solid thick line. It is easy to descry the inner closed lines and the outer open lines. The abrupt interruption on the outer part are due to the limit of our computational region, that can be correspond loosely to the tokamak walls.

Positive Triangularity

In the positive triangularity configuration, called in this work Global Positive (GP), the shape is characterised by a "D" shape pointing towards the LFS. This result is achieved by three magnetic coils disposed asymmetrically around the plasma. This causes the safety factor to bump up and down along the poloidal section, with its maxima in the section nearest to the shaping filaments. To this, it adds the fact that the shape is not symmetric anymore and the arc in which the curvature - that points inward - has the same direction to the density gradient[1] - that points outwards - is much longer than the one having the parallel configuration. To make this discussion clear it must be specified that the tokamak's symmetry axis is on the left of figure 3.3

Here below main parameters used for Global Positive configuration in this work are listed in table 3.3.

	Parameters
R_j	[−180, −180, 390]
Z_j	[−664, 456, 0]
I_j	[1.5, 0.72, 0.37]
A	17.2
a_g	78
P_0	[−190 , 0]

Table 3.3: Summary of the parameter used to build the Circular configuration

[1] In few words, the outer part, the arc facing the exterior of the tokamak in the LFS

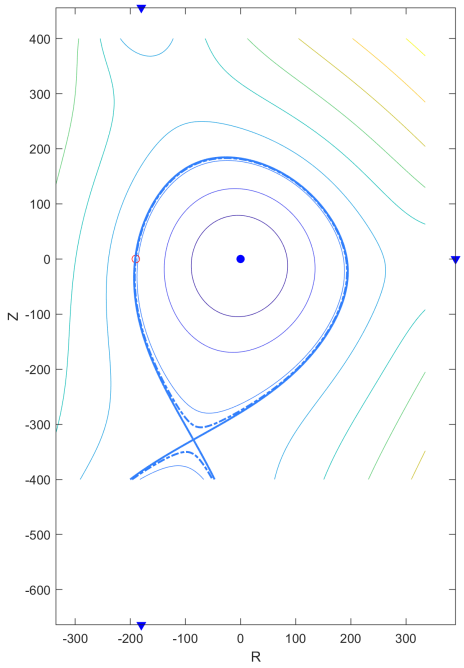

Figure 3.3: Positive Symmetric configuration. In the picture the plasma current is denoted by a circular blue dot, current filaments are flagged by a blue triangle, the point $P0$ through a void red circlet. The thick dashed line is the cross section of the magnetic surface on which simulations are run. The thinner coloured lines are other magnetic surfaces' sections. The separatrix is stressed through a solid thick line. It is easy to descry the inner closed lines and the outer open lines. The abrupt interruption on the outer part are due to the limit of our computational region, that can be correspond loosely to the tokamak walls.

Negative Triangularity

The negative triangulation configuration, in this work called Global Negative (GN), is the symmetric transformation of GP with respect to a vertical axis due to the change in sign in the R-coordinates of the shaping filaments. It is characterised by a "D" shape pointing toward the HFS.
All considerations made on the Global Positive configurations are still valid but they must be flipped. The tokamak's symmetry axis is on the left of figure 3.4

Here below main parameters used for Global Negative configuration in this work are listed in table 3.4.

	Parameters
R_j	[180, 180, −390]
Z_j	[−664, 456, 0]
I_j	[1.5, 0.72, 0.37]
A	17.2
a_g	78
P_0	[190 , 0]

Table 3.4: Summary of the parameter used to build the Circular configuration

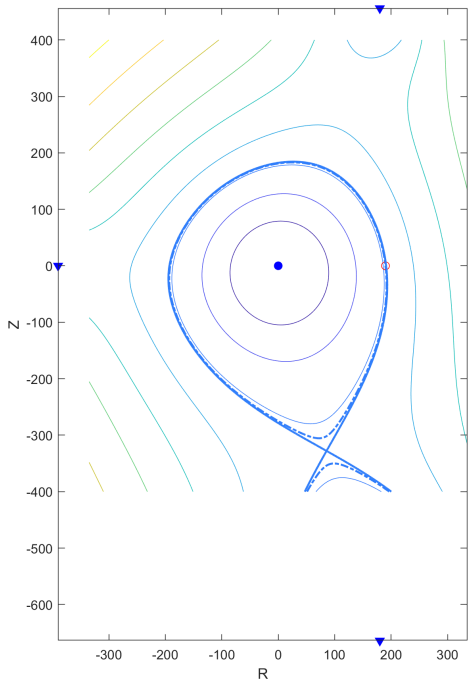

Figure 3.4: Negative Symmetric configuration. In the picture the plasma current is denoted by a circular blue dot, current filaments are flagged by a blue triangle, the point $P0$ through a void red circlet. The thick dashed line is the cross section of the magnetic surface on which simulations are run. The thinner coloured lines are other magnetic surfaces' sections. The separatrix is stressed through a solid thick line. It is easy to descry the inner closed lines and the outer open lines. The abrupt interruption on the outer part are due to the limit of our computational region, that can be correspond loosely to the tokamak walls.

4 | Linear GBS Results

In this chapter the main results of the linear GBS code are resumed.
Firstly, after a brief discussion on the instabilities' drive (§ 4.1), the topic is focalised on the Ballooning Mode dispersion relation (§ 4.2), deriving some analytical discussions (§ 4.2.1).
Then the results of GBS linear calculations are presented. Firstly the ones referring to the circular configuration (§ 4.3), in both RBM model (§ 4.3.1) and in full model (§ 4.3.2). Then the results for the shaped configurations are tackled (§ 4.4), always in RBM model (§ 4.4.1) and full one (§ 4.4.2).
The chapter continues with the evaluation of the pressure gradient length L_p (§ 4.5) and converges finally on a comparison with the previous literature (§ 4.6).

4.1. The Instabilities' Drive

In literature [5, 44] the main drive causing plasma instabilities has been identified as the pressure gradient that develops along the x direction. In linear analysis this last is restricted only to the equilibrium values for temperature and density fields, in the form of an exponential decay. A further approximation has been included, confounding the exponential function with its first order Taylor polynomial, an inaccuracy justified by the narrowness of the edge region with respect to the radius of the whole cross section. This spatial evolution, as a matter of fact, it has been observed to be a good approximation for what happen in the edge region both on the basis of experimental discharges [7, 9] and for nonlinear numerical simulations of the whole plasma.
The x dependency is fundamental since it is the drive of the simulated phenomenon. It is due to the pressure gradient, indeed, that the various fields can be cross-dependant, through the Poisson brackets operator. It is important, therefore, to deepen slightly the two parameters on which the pressure profile depends, η and R/L_n, being the first the ratio between density gradient length and temperature gradient length, and L_n/R the adimensionalisation of L_n. Given what recalled from section 3.1.1 and equation 2.15 it is

possible to state that

$$p_0 = p_{00}\left[1 + \left(\frac{1}{L_{T_e}} + \frac{1}{L_n}\right)x\right] \tag{4.1}$$

Holding that

$$L_p = \left(\frac{1}{L_{T_e}} + \frac{1}{L_n}\right)^{-1} = \frac{L_n}{1+\eta} \tag{4.2}$$

It must be stressed that the two parameters that describe the pressure gradient length, are both an input and an output of the problem. Despite the code needs them to run, it is possible to give as an input only a fist approximation of their value on the basis of previous experiences. The effective value of this parameters depends on a self-consistent description of the whole phenomena. The way to treat it will be discussed in 4.5.

4.2. RBM Dispersion Relation

To describe properly the Ballooning Mode some assumptions must be made. It is quite straightforward that the description is embedded in the GBS set of equations 3.14-3.18 but some simplifications must be carried out in order to remove coupling with other phenomena. To avoid coupling with sound waves, $k_\parallel \ll \gamma$ (in dimensionless form) is imposed, de facto corresponding into neglecting the $V_\parallel$ dynamics. The compressibility terms are dropped in continuity equations being smaller than R/L_n. Finally, to avoid Drift Waves coupling, the diamagnetic term $\nabla_\parallel(n + 1.71T_e)$ is dropped. A complete discussion is found in [25].
The resulting eigenvalue equations for RBM is therefore:

$$\gamma n = \frac{R}{L_n}\frac{\partial \phi}{\partial y} \tag{4.3}$$

$$\gamma \nabla_\perp^2 \phi = 2\hat{C}(n + T_e) + \nabla_\parallel \nabla_\perp^2 \psi \tag{4.4}$$

$$\gamma \frac{\beta}{2}\psi = \nu \nabla_\perp^2 \psi + \nabla_\parallel \phi + (1 + 1.71\eta)\frac{\beta}{2}\frac{R}{L_n}\frac{\partial \psi}{\partial y} \tag{4.5}$$

$$\gamma T_e = \eta \frac{R}{L_n}\frac{\partial \phi}{\partial y} \tag{4.6}$$

L and M matrixes in equation 3.22 being therefore

$$L = \begin{bmatrix} \mathbb{1}_{u,u} & 0_{u,u} & 0_{s,u} & 0_{u,u} \\ 0_{u,u} & D^{y,2}_{u,u} & 0_{s,u} & 0_{u,u} \\ 0_{u,s} & 0_{u,s} & \frac{\beta}{2}\mathbb{1}_{s,s} & 0_{u,s} \\ 0_{u,u} & 0_{u,u} & 0_{s,u} & \mathbb{1}_{u,u} \end{bmatrix} \tag{4.7}$$

and

$$M = \begin{bmatrix} 0_{u,u} & \frac{R}{L_n} D^{y,1}_{u,u} & 0_{s,u} & 0_{u,u} \\ 2\hat{C}_{u,u} & 0_{u,u} & -D^{\parallel,1}_{s,u} L^{em}_{s,s} & 2\hat{C}_{u,u} \\ 0_{u,s} & D^{\parallel,1}_{u,s} & -\nu \mathbb{1}_{s,s} L^{em}_{s,s} + (1 + 1.71\eta)\frac{\beta}{2}\frac{R}{L_n} D^{y,1}_{s,s} & 0_{u,s} \\ 0_{u,u} & \eta \frac{R}{L_n} D^{y,1}_{u,u} & 0_{s,u} & 0_{u,u} \end{bmatrix} \tag{4.8}$$

It is worth to highlight the role of β parameter in the current work. As a matter of fact, the aim is to study the phenomena in the $\beta = 0$ limit. Unfortunately, if this condition is met, L matrix become singular and therefore not invertible, since Ohm's equation would set an algebraic constrain on the magnetic potential ψ instead of describing its evolution. This could be addressed by reducing the number of variables to n, ϕ and T_e only and the number of equations as a consequence. This, however, would lead to the occurrence of the parallel laplacian operator $\nabla^2_{\parallel}$ that contain the term $\partial_y b_y$ which analytical evaluation can be tricky. Since a smoother solution was present, letting beta be small but not zero, it has been opted for this last.

4.2.1. Analytical Results for RBM

It is not possible to tackle analytically set of equations 4.3-4.6 in an arbitrary geometry. Anyway, it is possible to retrieve some important, however partial, information.
Firstly, it is readily achievable to assess, from equations 4.3 and 4.6 that the perturbations on temperature and density are proportional, leading to hot and dense regions, facing colder and looser ones.
It is not possible to easily say much more on an arbitrary geometry and therefore it can be worthy to study the behaviour in a circular, simplified geometry. In such geometry the most problematic term is the curvature operator, that would lead to a convolution integral in a Fourier approach. To overcome this obstacle the procedure is to study, in a local frame, what it happens to the most unstable point, i.e., where the curvature drive is the most intense. Remembering equation 3.7, this point is where the y-dependant coefficient of the curvature is maximum. Since this last has the arrangement of $\check{c}(y) = \frac{b_Z(y)}{\sqrt{b_Z(y)^2 + b_R(y)^2}}$, it is unambiguous that the two conditions to find it are $b_R(y) = 0$ and $b_z(y) > 0$. The first condition lead to the two points where the magnetic surface cross section has a vertical tangent. Since it is a closed curve there must be at least two of those point because of the Rolle theorem. The one with negative $\check{c}$, the innermost of the two, has a stabilising role and therefore it is not interesting in this evaluation.
In such frame, neglecting the effect of the Ohm's equation 4.5 and assuming a vanishing

gradient for electron velocity, following the steps of [5] it is retrieved the equation

$$\gamma^2 k_y^2 \phi - 2(1+\eta)\frac{R}{L_n} k_y^2 \phi = 0 \tag{4.9}$$

To have a non null perturbation on ϕ, the following condition it must hold:

$$\gamma = \gamma_{id}^{RBM} = \sqrt{2\frac{R}{L_p}} \tag{4.10}$$

Such equation, does not discriminate between the different modes but foreseen a behaviour independent of the wave-vector. If, instead, we take into account the effect of the resistance ν, the evaluation of a similar process leads to

$$\left(\gamma^2 + \frac{1}{\nu}\frac{k_\parallel^2}{k_y^2}\gamma - (\gamma_{id}^{RBM})^2\right)\phi = 0 \tag{4.11}$$

By some manipulation of 3.11, taking into account that b_y is constant in a circular geometry, it is possible to express $\frac{k_\parallel}{k_y}$ as a function of poloidal and toroidal wave-numbers. It holds that $\frac{k_\parallel}{k_y} = a\left(\frac{1}{q} - \frac{n_Z}{m}\right)$, where n_z is the wave-number of z-direction, and therefore an input of the problem, and m the one in y-direction, and therefore an output. It holds, also, that the local worst growth rate in the resistive case can be expressed as

$$\gamma = \sqrt{(\gamma_{id}^{RBM})^2 + \left(\frac{a^2}{2\nu}\right)^2\left(\frac{1}{q} - \frac{n_Z}{m}\right)^4} - \left(\frac{a^2}{2\nu}\right)\left(\frac{1}{q} - \frac{n_Z}{m}\right)^2 \tag{4.12}$$

It emerges, in this last equation a dependence on the mode, trough the z-wave-number n_Z and the evaluated y-wave-vector $k_y = (2\pi m)/L_y$. The maximum instability it is obtained if the condition $m = qn_Z$ is fulfilled.

4.3. Circular Configuration Simulations Results

Circular geometry is the starting point of this thesis work. It's role has been mainly for benchmark purposes but it shows, anyhow, some important characteristic with the respect the shaped configurations. Two linear simulations have been performed in circular geometry, in RBM model (equations 4.3-4.6) and in full model (equations 3.14-3.18)

4.3.1. RBM Branch

The analysis of the RBM branch in circular geometry has been carried solving with GBS linear code the set of equations 4.3-4.6. The resulting dispersion relation is reported in figure 4.1. It is possible to observe a monotonically increasing function that well matches with previous literature results [25].

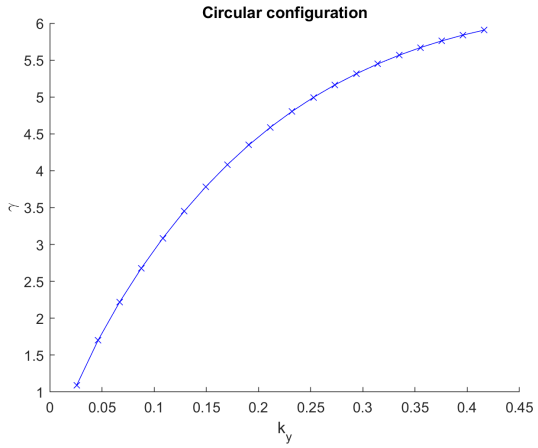

Figure 4.1: Growth rate for a circular configuration simulated within RBM set of equations, as a function of the evaluated y-wave-vector k_y. The used parameters are $R_0 = 700$, $\eta = 1$, $\beta = 10^{-8}$, $R/L_n = 20$

In agreement with equation 4.9 the evaluated growth rate is always smaller than γ_{id}^{RBM}. This holds since the evaluation carried through in subsection 4.2.1 is local and achieved for the point where the instability's drive plays the most intense role, i.e. the LFS mid-plane. In section 4.1 it has been stated that the driver is the equilibrium pressure gradient in the bad curvature region. However, the exponential growth of the mode implies that the perturbation self-sustains and locally grows proportionally to particular linear combination of the various fields' perturbations, dictated by the model used. Therefore, the perturbation distribution along the poloidal cross section plays a major role in determining the mode's growth rate. Since each point suffers a different local drive along the y coordinate, the mode growth rate varies according to the perturbation distribution. A localised perturbation in a thin interval around the LFS mid-plane results in higher growth rate than one with not negligible components scattered all around the poloidal cross section, Since the perturbations, in general, are not localised in the LFS mid-plane but have a not negligible component on a wider y interval, the growth rate is always smaller than γ_{id}^{RBM}. The dependence of γ growth rate on the mode, therefore, cannot be pictured by the model retrieved in 4.2.1 but it can be attributed to the different length of the interval where the perturbation is not null. In 4.4 two different eigenvalues are displayed and the

difference in localisation is clear in n, ϕ and T_e eigenvalue. For small k_y the growth rate tends to zero. This is mainly due to the delocalisation of the mode, as is pictured in figure 4.4a displaying a mode characterised by small variation between the LFS and the HFS.

For what concerns the relation between n_z and m wave-numbers, the results are pictured in 4.2. Here the prediction made in 4.12 is made explicit. Since the analysis is for the most unstable mode it is reasonable to expect to retrieve the condition that maximise 4.12. This is the case for this simulation.

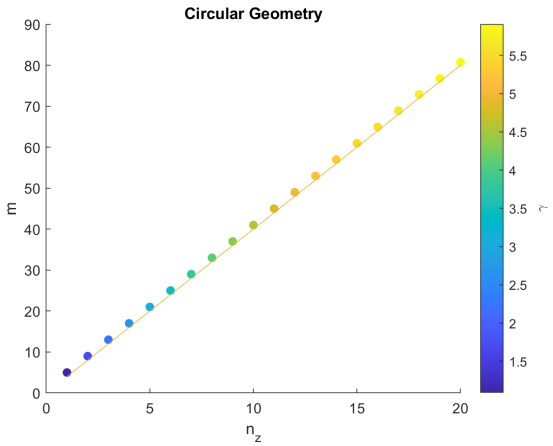

Figure 4.2: In picture the distribution of the evaluated poloidal wave-number is plotted with respect to the toroidal wave-number in the circular geometry in RBM simulation. The above solid line displays the locus $m = qn$. The agreement between that and the simulated points is very good, the distance being less than 0.1%, as predicted by 4.12. The colorbar displays the eigenvalue's real part magnitude.

As it is possible to see from figure 4.2 the n_z and m well align along the straight line $m \simeq qn_z$. The $\sim$ symbol is due to the fact that n_z, m and k_y can assume only a discrete set of values. The respect of this rule can be observed in the eigenvalues, the number of oscillations being roughly equal to qn_z. However, neither 4.12 is able to predict the value of γ since this last comes from the interplay of points with different instability drive.

4.3.2. Full Model

To compare RBM results, obtained with the set of equations 4.3-4.6, a similar analysis through linear GBS code has been performed to the full model, equations 3.14-3.18.
In full model similar results are retrieved. The growth rate dependency on k_y, reported in 4.3a, shows a similar behaviour to the one evaluated in 4.1 and displays a similar value of γ. This could suggest that the principal unstable mode in this simulation is the RBM. Also the mode distribution in the (n_Z, m) plane follow the same scheme. It must be said,

however that, as extensively studied by [25], the principal mode depends on the set of parameters describing the plasma. Following the criteria derived in [25] it is possible to state that, in circular frame, in the simulation examined, the attended main behaviour is the RBM one, as the GBS linear code results suggest.

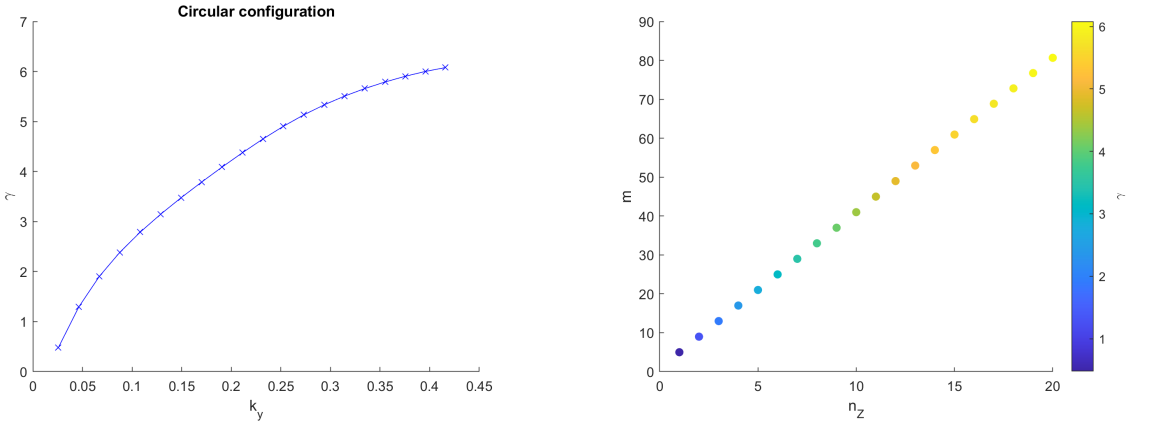

(a) Growth rate dispersion relation.

(b) Poloidal wave-number m with respect to the toroidal wave-number n_Z

Figure 4.3: Results of the linear GBS evaluation in a circular geometry with a full model. The used parameters are $R_0 = 700$, $\eta = 1$, $\beta = 10^{-8}$, $R/L_n = 20$

However, some discrepancies can be found, especially for what concerns the eigenvalues. As it is possible to see comparing 4.4b and 4.5b. Despite these two present a similar behaviour and shape the decrease at low field side is more accentuated in the RBM case, suggesting the coupling with other minor modes in the full picture, that suffers less dumping in the HFS.

Here below the eigenvalues for the two circular configurations simulations are reported.

4.4. Shaped Configurations Simulations Results

Six linear simulations have been performed, using the linear GBS solver. The three magnetic configuration used are the one presented in section 3.3: GS, GP and GN. For each of them two run have been carried, respectively with the RBM model (equations 4.3-4.6) and the full model (equations 3.14-3.18)

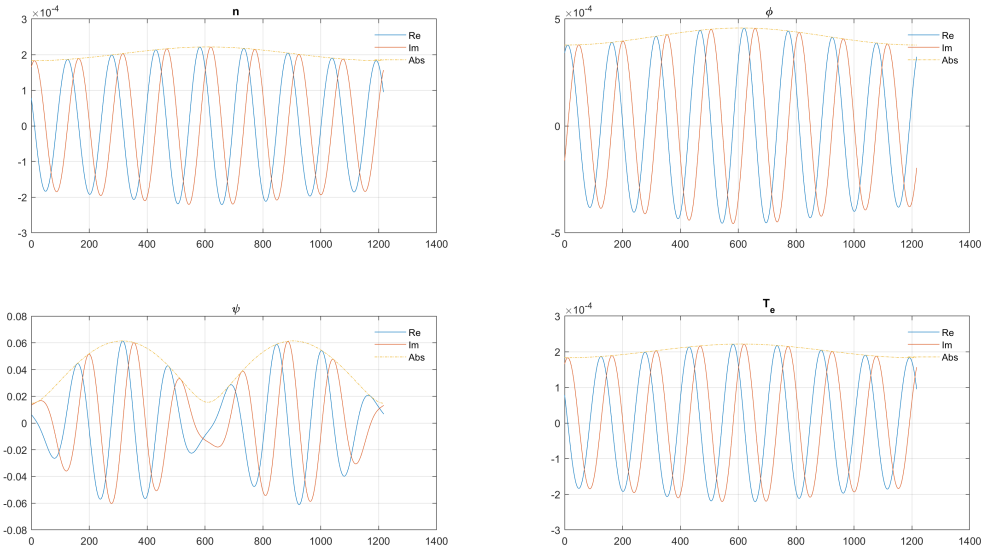

(a) $n_z = 2$ mode, Circular

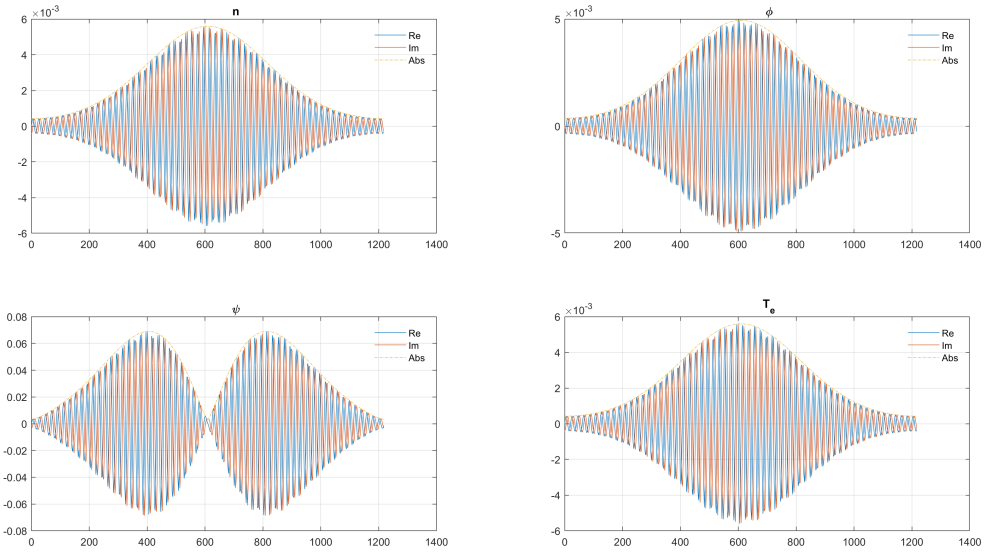

(b) $n_z = 15$ mode, Circular

Figure 4.4: Eigenvalues evaluated through GBS linear, for the RBM model in circular geometry. They represent the y dependence of the perturbation. y coordinates zero correspond to the LFS midplane.

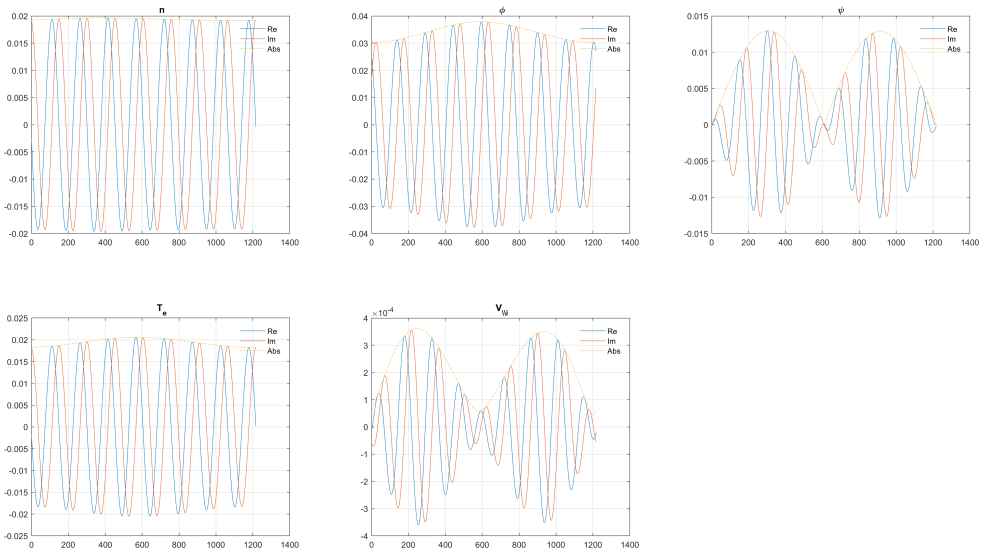

(a) $n_z = 2$ mode, Global Symmetric

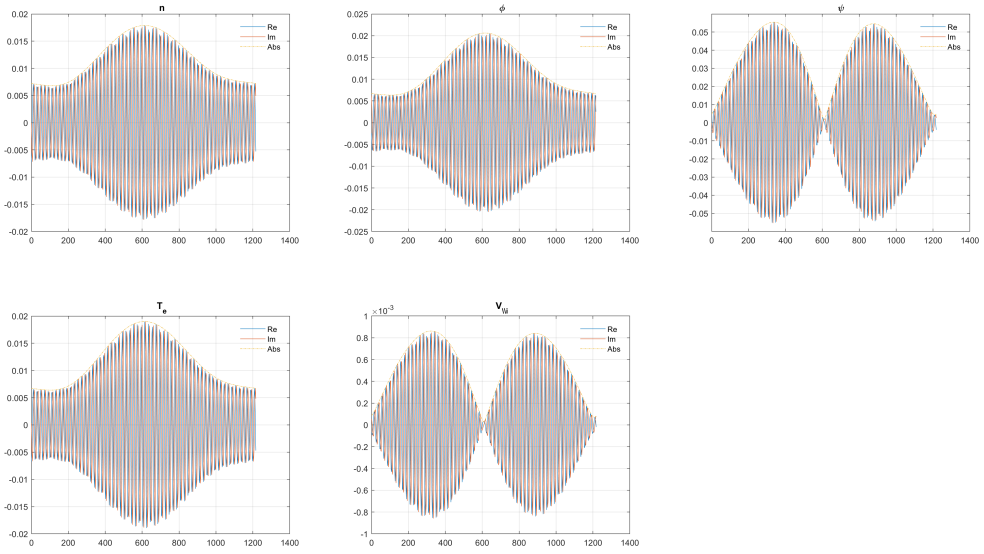

(b) $n_z = 15$ mode, Global Symmetric

Figure 4.5: Eigenvalues evaluated through GBS linear, for the full model in circular geometry. They represent the y dependence of the perturbation. y coordinates zero correspond to the LFS midplane.

4.4.1. RBM Branch

The three shaped configurations have been investigated: Global Symmetric, Global Positive and Global Negative, characterised, respectively, by a null, positive and negative triangularity. Firstly, an analysis trough on the RBM branch through the GBS linear code has been carried. The results have been resumed in figure 4.6.

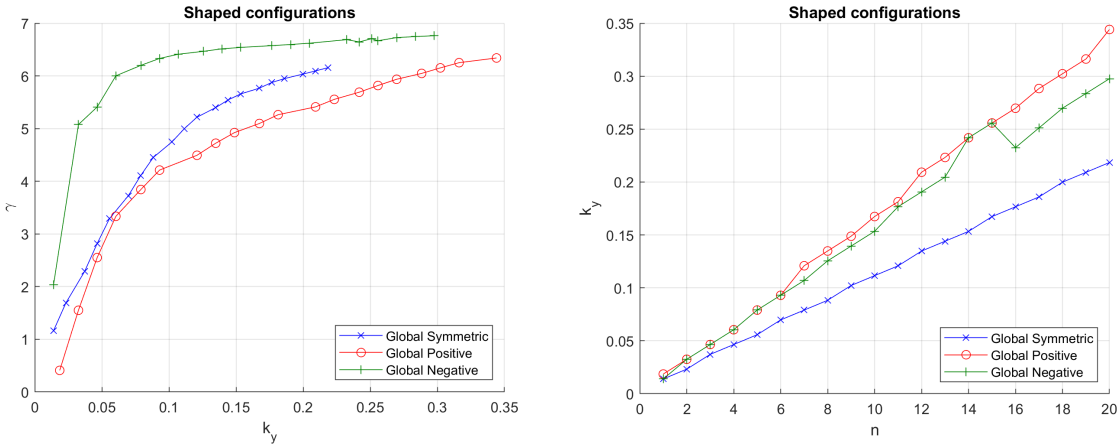

(a) Growth rate dispersion relation.

(b) Poloidal wave-vector k_y with respect to the toroidal wave-number n_Z

Figure 4.6: Results of the linear GBS evaluation in the shaped geometries with a RBM model. The used parameters are $R_0 = 700$, $\eta = 1$, $\beta = 10^{-8}$, $R/L_n = 20$.

Also, in this case the growth rate is a monotonically increasing function with k_y. The graph displays a maximum value in the order of γ_{id}^{RBM}, but always smaller than it. This is coherent with the above discussion, since, as it has been evaluated it, such parameter is the local grow rate of the most unstable point. Looking to the eigenvalues in figure 4.8, it can be noted an important, general localisation of the eigenvalue in the LFS, also at the lowest wave-numbers, as in 4.8a, justifying the steeper slope for small k_y, pictured in figure 4.6a. In this case the increase in the localisation is less evident, in n and T_e eigenvalues. However it is still present in ϕ. In T_e and n eigenvalues, instead, it can be noted a displacement of the maximum of the eigenvalue, and therefore of the perturbation, toward higher values of y. Since the maximum is always in the LFS, such shift causes an increase of the destabilising drive suffered by perturbation. Both this two mechanisms, the shift in T_e and n and the localisation in ϕ can be linked to the monotonically increasing behaviour of γ with n_Z. In figure 4.8a and 4.8b is perceivable in the eigensolutions of all the four variables a displacement of the mode maximum toward values with higher positive, curvature. However, for n, ϕ and T_e the modes present in both cases their maximum values in the region nearest the X-point (the closest point on the surface lays in y

= 405). This behaviour can be attributed to the high q that characterise that region. As discussed previously, in subsection 3.3, the fieldlines slow its twirling along the magnetic surface poloidal direction. Since so high local values of q $\geq$ 20 are reached the perturbation stays for a long time in the lower part of the magnetic configuration during its toroidal turn. Also because of that it is possible to remark, especially in 4.8a, an increase in the spatial frequency of the perturbation in the region nearest the X-point and a loosening in the further regions. This can still be attributed to q variation. The perturbation in the toroidal direction has the same spatial angular frequency everywhere but the fieldlines wrap on the torus with a different poloidal to toroidal ratio $\frac{d\phi}{d\theta} = \frac{1}{q}$, resulting in a variable poloidal frequency.
From such, two results emerge. The simulations suggest that this negative shape is deleterious for the RBM stability. For each wave-number the growth rate is bigger than the triangularity-less configuration. Global positive, on the contrary, shows a slightly better behaviour, with dumped instabilities. Moreover, the predicted effect of the shaping process, independently on the sign of the triangularity is to enlarge the wave-vector, of a comparable amount. The evaluated mean increase in the positive triangularity configuration is of 50% for the y-wave-vector with the same wave-number, and of 39% for the negative one.

4.4.2. Full Model

The full model has been implemented through GBS linear code with 4.3-4.6 model. This allows to study the complexity of the plasma loosing on one hand analytical manageability but supplying a complete picture of the phenomena.

For what concerns the growth rate, remembering the note on its real part, discussed in the subsection 3.1.2, the main features are kept unchanged. Simulations suggest that triangularity leads to a more unstable configuration, enhanced in the negative case. Differently, in full mode the positive and negative triangularity cross themselves, showing that high wave-number perturbations lead to an higher instability for the positive triangularity. Differently on the RBM case, here, the picture exhibits a non-null behaviour on small wave-numbers, behaving, therefore differently from a sound branch, as RBM is, suggesting to look somewhere else the reason for such conduct. The high wave-vector modes show a decrease in growth rate.
For what concerns eigenvectors they display a similar behaviour to the one in RBM case. As a matter of fact an increase of the wave-number reflects in an increase in the num-

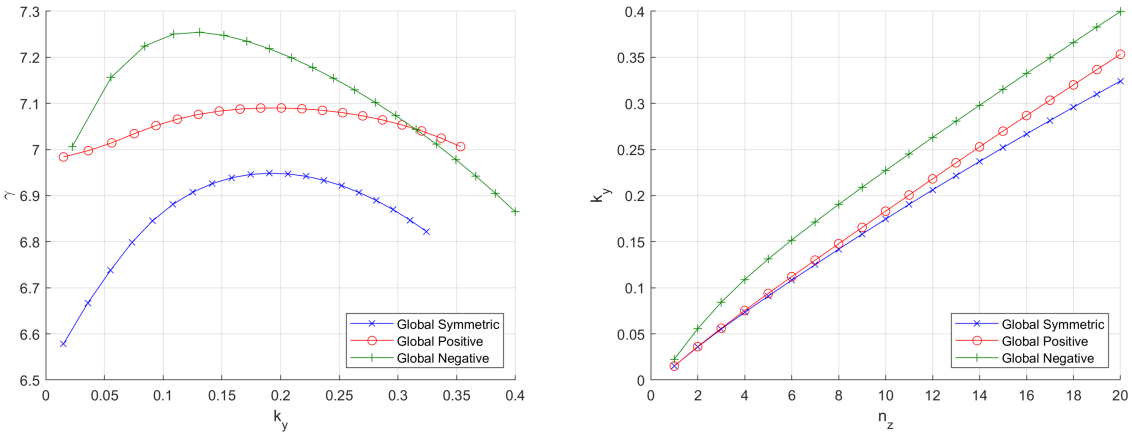

(a) (b)

Figure 4.7: The two figures display the dispersion relation for full simulation in the three shaped magnetic configurations. The used parameters are $R_0 = 700$, $\eta = 1$, $\beta = 10^{-8}$, $R/L_n = 20$.

ber of oscillations found in that, as clearly pictured by figures 4.9a and 4.9b. The main non-vanishing part of the eigensolutions is the LFS part, and near the bottom of the configuration in all cases. This suggests that in this configuration the main perturbation is the RBM.
Finally, an important difference in the behaviour depending on the triangularity is highlight by figures 4.8c and 4.8d. In the positive case the absolute value of the eigensolutions has quite milder slopes, with respect to the steeper ones in the negative case. Moreover Global Negative configuration is localised in higher values of y, leading to a more unstable mode.

Here below some eigenvectors are reported, evaluated for the two models and the three geometries in this section.

4.5. Numerical Evaluation of the Equilibrium Pressure Gradient

Following the path traced by Riva in [34], this chapter will try to evaluate the pressure gradient length L_p. In this section the assessment will be achieved through the linear GBS solver. To figure out the pressure gradient length trough the linear solver it is assumed a gradient removal turbulence saturation, i.e. the disappearance of the gradient

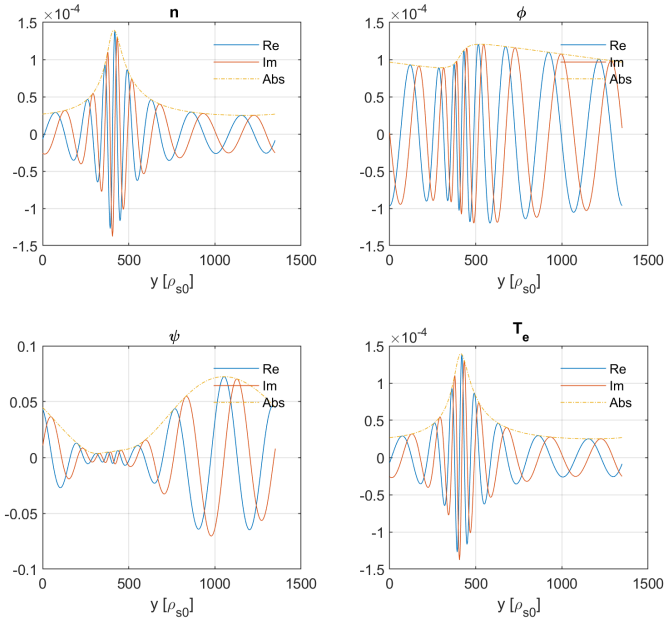

(a) $n_z = 2$ mode, Global Symmetric

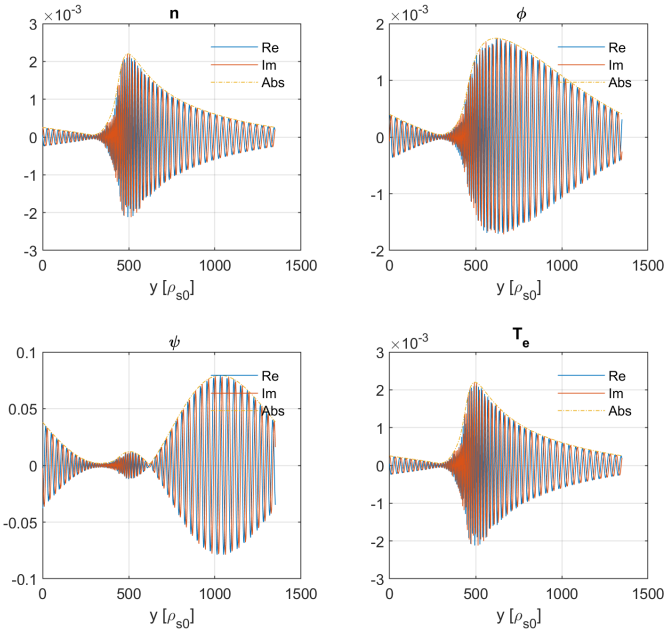

(b) $n_z = 15$ mode, Global Symmetric

Figure 4.8: Eigenvalues evaluated through GBS linear, for the RBM model in GS geometry. They represent the y dependence of the perturbation. y coordinates zero correspond to the LFS midplane.

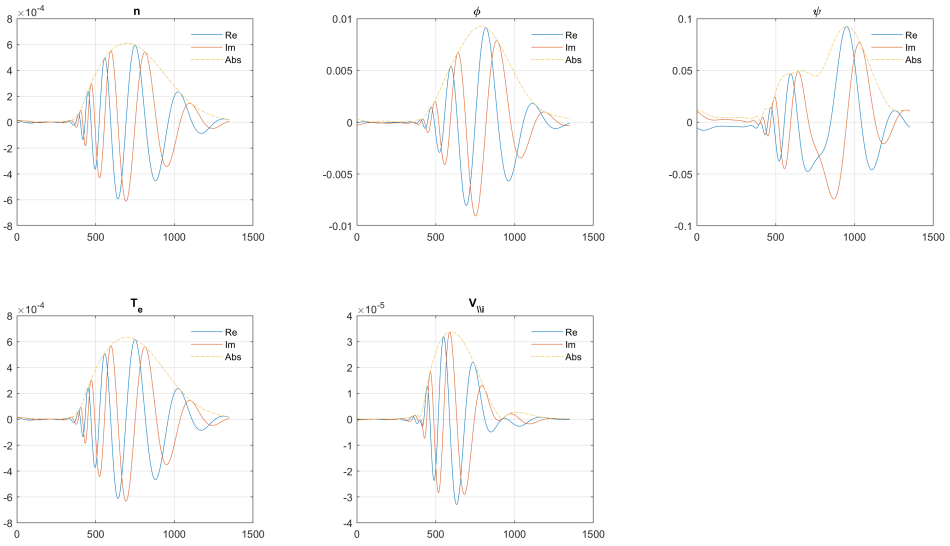

(a) $n_z = 2$ mode, Global Symmetric

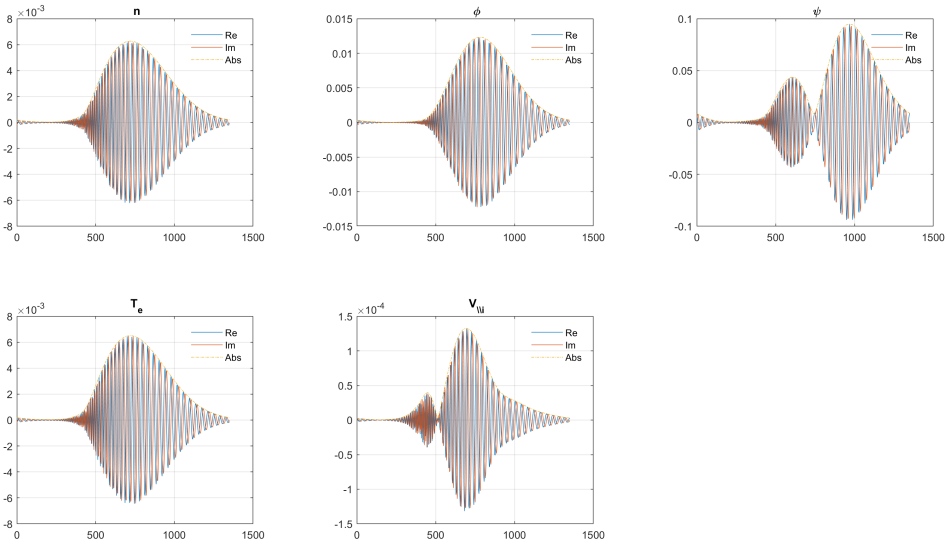

(b) $n_z = 15$ mode, Global Symmetric

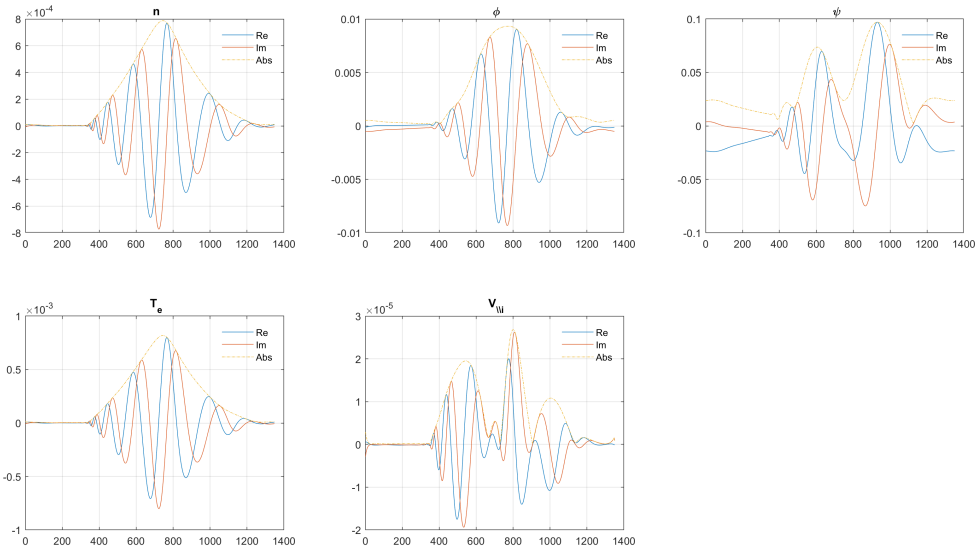

(c) $n_z = 2$ mode, Global Positive

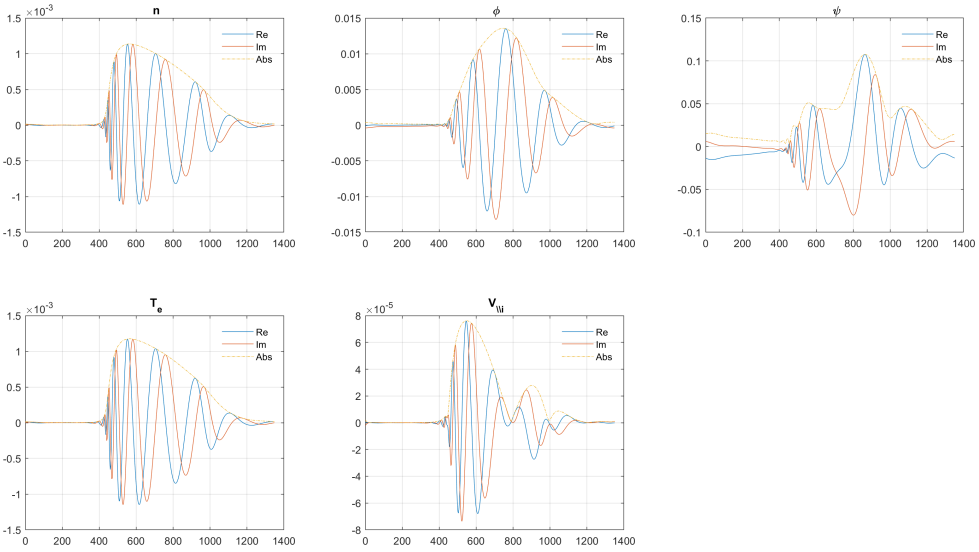

(d) $n_z = 2$ mode, Global Negative

Figure 4.8: Eigenvalues evaluated through GBS linear, for the full model in GS, GP and GN geometry. They represent the y dependence of the perturbation. y coordinates zero correspond to the LFS midplane.

and therefore the fading of the instability drive. This nonlinear phenomenon is thought to be at the basis of the turbulence in the edge region [8]. The estimate of L_p is therefore based on the gradient removal theory in a circular magnetic surface geometry. As derived in [34] the pressure gradient length can be evaluated throughout the inequality:

$$L_p = \frac{q}{c_s}\left(\frac{\gamma}{k_y}\right)_{max} \tag{4.13}$$

Since 4.13 is an implicit equation, it must be approached numerically. The procedure is to solve for 3.22 for γ for different L_p values, letting varying L_n and looking for the k_y for which the value $\frac{\gamma(k_y)}{k_y}$ is maximum. It is important to remember that we assume $c_s = 1$. Also, the work develops in a shaped geometry and therefore q depends on y through the equation $q = \frac{a(y)}{Rb_y(y)}$. Equation 4.13, on the other hand, do not shows an explicit dependence on y. For that, it has been used the value of q at the LFS mid-plane, the point where the drive is the most important. The considered parameters are $\eta = 1$, $R_0 = 700$, $\beta = 10^{-8}$.

	Global Symmetric	Global Positive	Global Negative
Linear L_p $[\rho_{s0}]$	42.4	34.9	59
q LFS midplane	3.48	3.24	2.75

Table 4.1: Summary of the pressure length evaluated in the different geometries, for both linear and nonlinear simulations.

Table 4.1 resumes the self-consistent settling of L_p gradient length, pictured in figures 4.9a, 4.9b and 4.9c.
Through the linear solver it is evaluated that positive triangulation has a beneficial effect, causing a steeper gradient and therefore a better confinement. Negative triangularity, instead, cause the profile to flatten out, providing a looser one. However, the evaluated length are too long if compared to the average minor radius of the surface we are working on. For the Global Symmetric the average minor radius is $\overline{a} = 219\rho_{s0}$ and for Global Negative and Global Positive Of $\overline{a} = 214\rho_{s0}$. L_p consists respectively in the 19.4%, 16.2% and 27.6% of the total minor radius. Such values are comparable to the thickness of the edge region, suggesting a very low decrease in the pressure profile, in contrast with what attended.

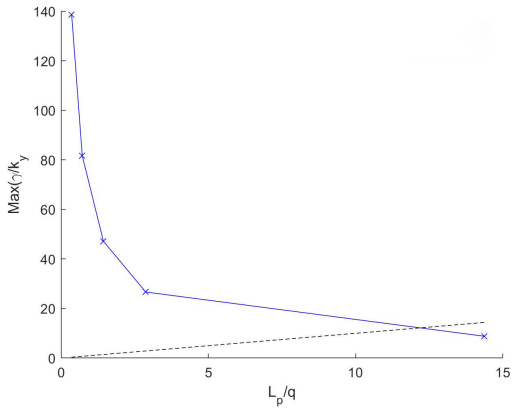

(a) Global Symmetric Geometry

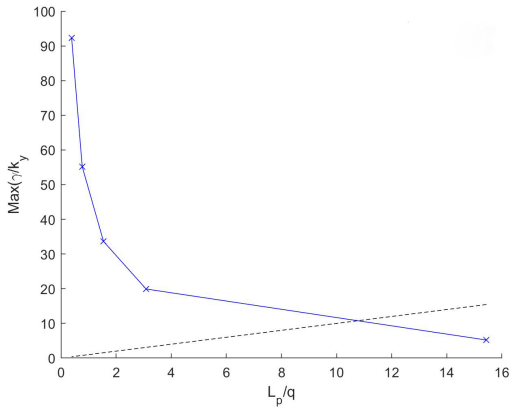

(b) Global Positive Geometry

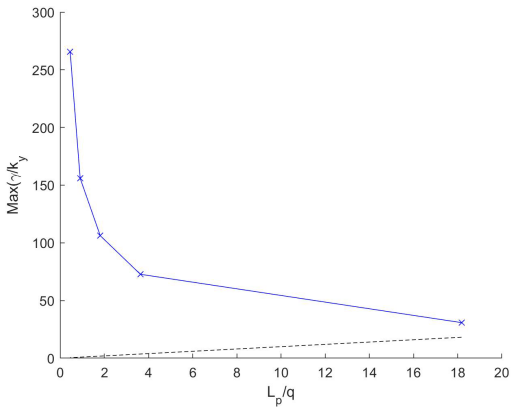

N

(c) Global Negative Geometry

Figure 4.9: Graphs used for the estimation of the pressure length L_p. The various points on the solid line correspond to the different simulation letting R/L_n vary. The dashed line corresponds to the identity. Their crossing point, therefore, is the one satisfying equation 4.13. For Global Negative a linear interpolation has been carried through.

4.6. Previous Literature Comparison

In previous sections 4.4 and 4.5, the effect of triangularity has been globally evaluated as negative for both stability and pressure gradient length.
A similar work, with a different methodology, has been carried out by Riva [34]. This section refers to his analysis on RBM stability and pressure gradient length evaluation for different values of elongation and triangularity[1] in a self-consistent Solov'ëv equilibrium. The two works have been carried in a similar plasma's parameters set as reported in table 4.2. The main differences consist in the $\frac{m_e}{m_i}$ parameter but it plays a minor role since, as discussed previously, also in the full model the main instability is Resistive Ballooning Mode, in which the electron mass is neglected. The main branch retrieved in this work is in agreement with the work made by Mosetto [25]. The comparison, however, can't be made explicit since configurations used in this work are not characterised by a well-defined value of triangularity.

	This work	Riva [34]
R_0	700	500
ε	0	0
η	1	0.66
ν	0.1	0.1
β	10^{-8}	0
$\frac{m_e}{m_i}$	0.005	0.0005

Table 4.2: Summary of the various quantity used in Riva's work and in this thesis.

In this work, similar numerical results to the ones retrieved by Riva have been found. Riva identifies in his analysis that for mild elongation, neglecting aspect ratio aspects and Shafranov shift, as is the case currently analysed, the maximum growth rate is characterised by a value of the ratio γ/γ_{id}^{RBM} in the interval [0.4-0.7]. The values obtained the present work fall in the upper part of such interval. In our case, being $\gamma_{id}^{RBM} = 8.94$ the evaluated growth rate are reported in table 4.3

	C	GS	GN	GP
$\gamma_{\max}$	5.91	6.15	6.34	6.76
$\gamma_{\max}/\gamma_{id}^{RBM}$	0.66	0.68	0.71	0.76

Table 4.3: Summary of the values obtained in RBM simulations (§ 4.3.1, 4.4.1)

[1] For a brief treatise of this parameters, it is possible to refer to A

The circular configuration leads to results well collimated with Riva's ones. However, in his work Riva evaluates negative triangularity as beneficial. The growth rate for negative triangularity is always smaller than the positive counterpart. On those aspects our results diverge.

For what concerns the pressure gradient length, instead, this thesis's results are in agreement with the elongation-less configuration, treated by Riva. The GS and GP L_p are in a some % interval around the value estimated by Riva, GN in a 20% one. In this case also the trend is respected. However, this discussion is a bit tricky, since the evaluated pressure gradient length drops as soon the elongation increases slightly and the trend reverses, making the GN configuration the one with better confinements properties. Since the configuration treated in this work has not a well-defined elongation and the results presented in Riva are harshly depending on this parameter, some deeper investigation would be needed.

5 | Non-Linear GBS Results

In this chapter a preliminary analysis of GBS code's non-linear results is discussed. In a first section (§ 5.1) the results are shifted through and a brief discussion is provided. Then, after a discussion on the impact of the Boussinesq approximation on the code (§ 5.2), the confinement properties emerging from the simulations are discussed (§ 5.3)

5.1. Shaped Configuration Simulations Results

Two sets of nonlinear simulations have been carried for each of the shaped configuration treated in section 3.3. Calculations have been accomplished through GBS code. The two sets distinguish for the different value in resistivity. The fist one is characterised by $\nu = 0.1$, the second one $\nu = 0.3$. Other relevant physical parameters are $R_0 = 500$, $\varepsilon = 0.3$, $\tau = 1$. With such values, from linear discussion in chapter 4 and previous literature [25], we expect to retrieve a situation principally characterised by RBM, therefore a dynamic in which LFS perturbation are the most important. A complete treatment in numeric can be found in [23]. For the reference temperature and density, typical values at LCFS of TCV L-mode discharge are considered, $n_0 \simeq 10^{19} m^{-3}$, $T_{e0} \simeq 20eV$.

From a preliminary analysis of figures 5.1 it is possible to remark an increase in particle and heat outflow from the LCFS in positive triangularity (5.1c-5.1d). In negative one (5.1f-5.1e) the outflow is still present but it is reduced with respect to positive one. Particularly, the outflows concentrate in the lower part of the configuration, in the area near the X-point. This phenomenon is even less evident in the symmetric configuration. Such behaviour recalls the eigenvalues evaluated in section 4.4 and pictured in figure 4.8, where the maximum of perturbations was found to be in the area close to the magnetic null point, especially in GN configuration.

For what concerns the edge region, roughly the annular area corresponding to values pictured in bright red in figures 5.1, it is possible to observe higher fluctuations in the LFS

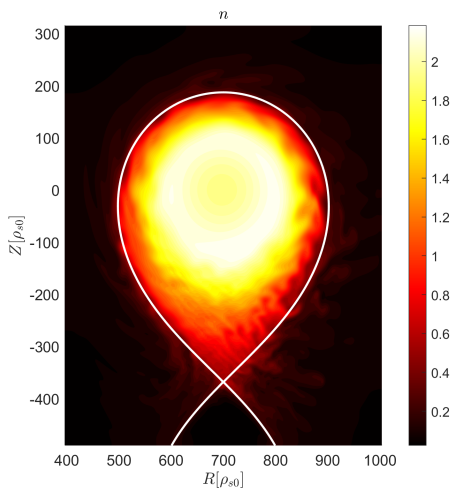

(a) GS, $\nu = 0, 1$, density distribution

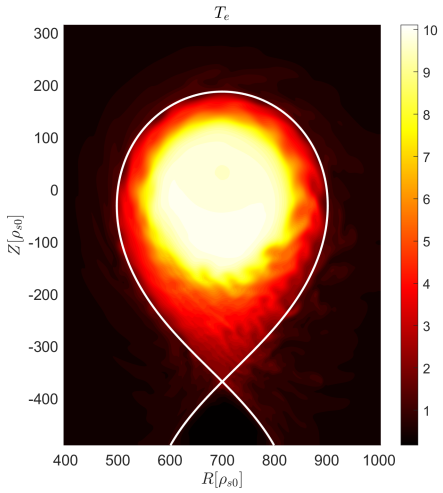

(b) GS, $\nu = 0, 1$, temperature distribution

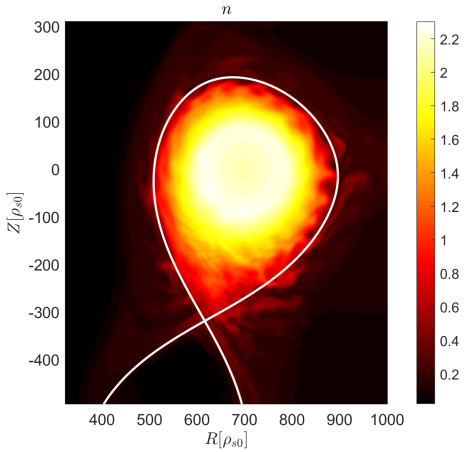

(c) GP, $\nu = 0, 1$, density distribution

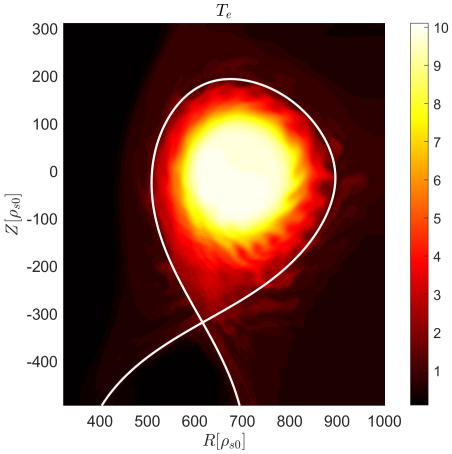

(d) GP, $\nu = 0, 1$, temperature distribution

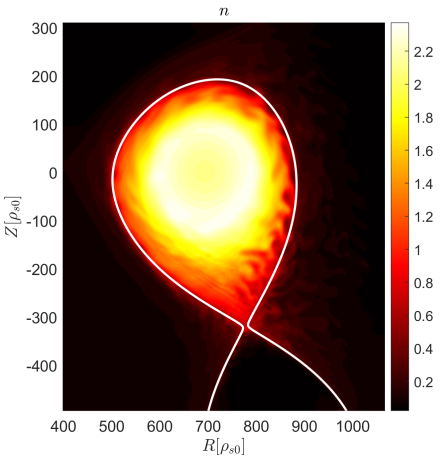

(e) GN, $\nu = 0, 1$, density distribution

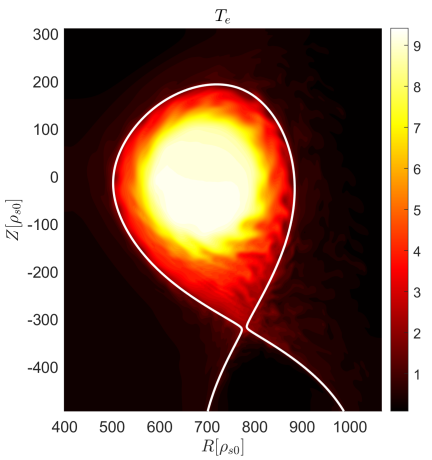

(f) GN, $\nu = 0, 1$, temperature distribution

Figure 5.1: Density and Temperature field in various magnetic configurations, evaluated through GBS code in $\nu = 0, 1$ case.

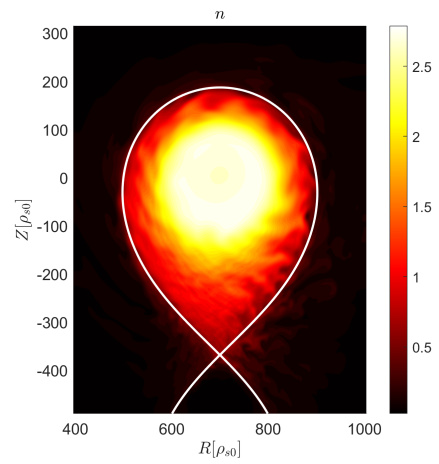

(a) GS, $\nu = 0, 3$, density distribution

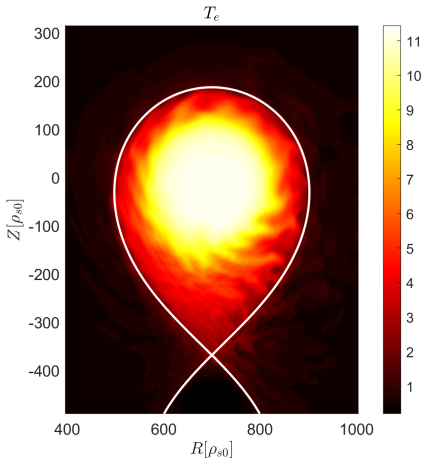

(b) GS, $\nu = 0, 3$, temperature distribution

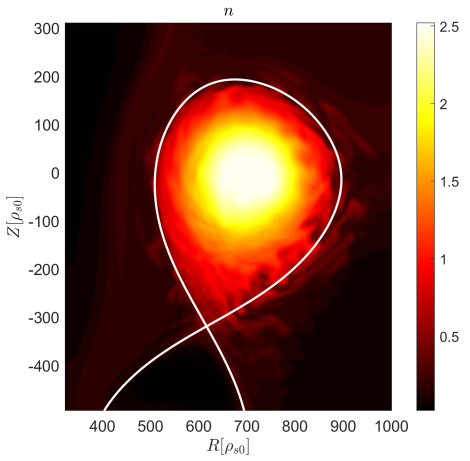

(c) GP, $\nu = 0, 3$, density distribution

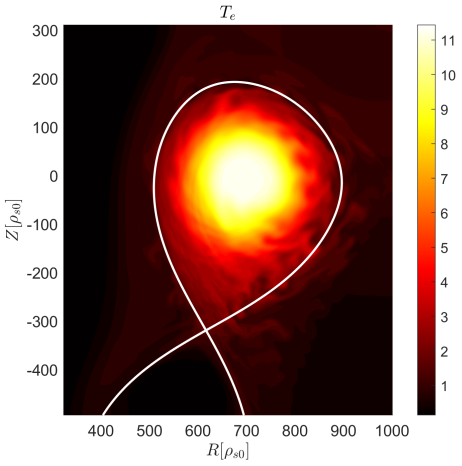

(d) GP, $\nu = 0, 3$, temperature distribution

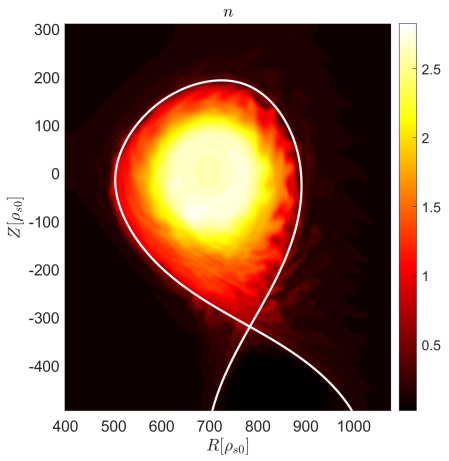

(e) GN, $\nu = 0, 3$, density distribution

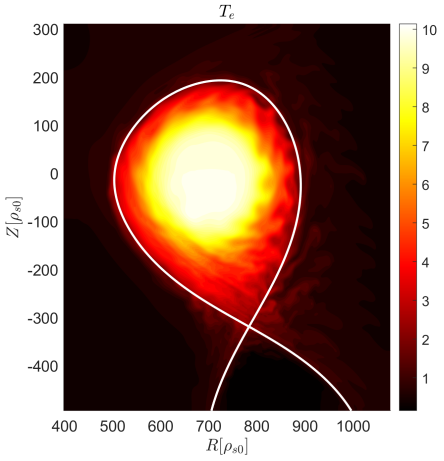

(f) GN, $\nu = 0, 3$, temperature distribution

Figure 5.2: Density and Temperature field in various magnetic configurations, evaluated through GBS code in $\nu = 0, 3$ case.

region in each configuration. In this region, also, more extended volumes characterised by low values of temperature and density, are present, with respect of the HFS. This suggests the presence of Resistive Ballooning Mode as the most important unstable perturbation for the chosen parameters set. Fluctuations are more important, however, in positive triangularity, suggesting worse confinement properties.
In $\nu = 0.3$ simulations, pictured in figure5.2, similar trends emerge. However, ELMs become more intense and extended with respect to $\nu = 0.1$. The instabilities seem to be increased, especially in the positive triangularity configuration, figures 5.2c, 5.2d. Moreover the confinement capabilities emerge to be worsen, since wider edge layers are pictured.

5.2. The Boussinesq approximation

An additional simulation was run for each resistivity value, with the fading of the Boussinesq approximation. The objective, here, was to infer the dependency of the simulations on the underlying hypotheses.
The Boussinesq approximation consists in $\nabla_\perp \frac{nc}{B\omega_i}\frac{d}{dt}(\vec{E} - \frac{\nabla_\perp p_i}{en}) \simeq \frac{nc}{B\omega_i}\frac{d}{dt}(-\nabla^2_\perp \phi - \frac{\nabla^2_\perp p_i}{en})$ [13] , i.e. in the possibility to switch between the $\nabla_\perp$ and $\frac{d}{dt}$ operators.

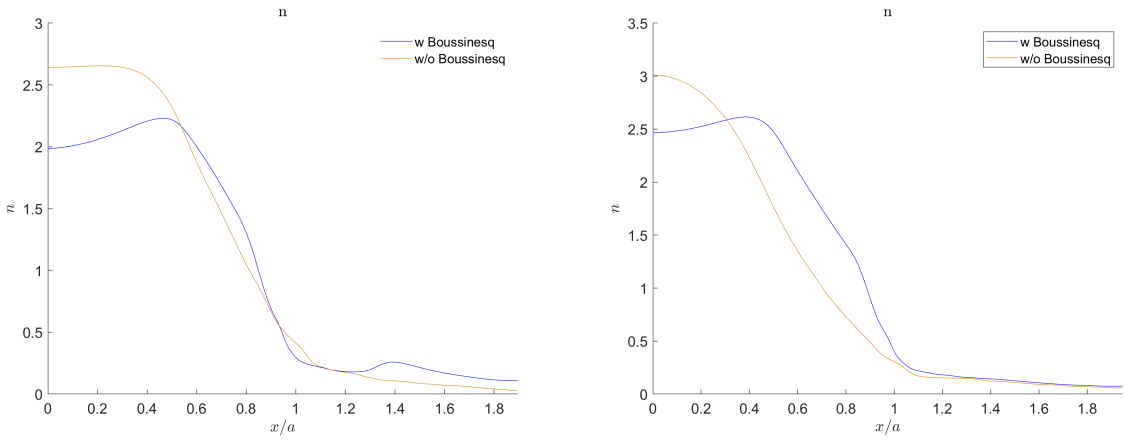

(a) $\nu = 0,1$ (b) $\nu = 0.3$

Figure 5.3: x-dependence of n field in the LFS outer mid-plane, in a time averaged, toroidal averaged picture.

In figure 5.3, the radial dependence at LFS outer mid-plane is retrieved, i.e. on the line that from the center of the configuration travel toward the outside of the plasma in the LFS, in the horizontal direction. The displayed values have been averaged in time and on the toroidal angle in order to cut off oscillation and to get as close as possible to the

actual equilibrium value. On such line, the edge layer is found roughly in the interval [0.9, 1] of the variable x/a. From calculations it is retrieved a good agreement for $\nu = 0.1$ and a mildly good one for $\nu = 0.3$. This do not hold in the core where the results are noticeably different. Since $\frac{d}{dt} = \frac{\partial}{\partial t} + \vec{V} \cdot \nabla$, from figure 5.3 it seems that the operators $\vec{V} \cdot \nabla$ and $\nabla_\perp$ roughly commutes in the edge layer and the approximation holds.

5.3. Numerical Evaluation of the Equilibrium Pressure Gradient

With the results retrieved with GBS code, following the steps of [34], it is possible to evaluate the pressure gradient length and therefore the capability of the configuration to confine the plasma.
The results displayed in figures 5.1 and 5.2 are averaged on time and on the toroidal angle and illustrate the average behaviour on the poloidal plane. The radial dependencies are extrapolated for the LFS outer mid-plane as reported in figure 5.4. An exponential fit is performed for density field in order to capture a first approximation of its gradient length:

$$f_n(x) \propto e^{-\frac{x-a}{L_n}} \tag{5.1}$$

The same procedure is realised for temperature field. Once retried the density and temperature gradient lengths, it is possible to evaluate the pressure gradient lenght through equation 4.2

$$L_p = \left(\frac{1}{L_{T_e}} + \frac{1}{L_n} \right)^{-1} \tag{5.2}$$

The results obtained with this method are listed in table 5.1

	Global Symmetric	Global Positive	Global Negative
$\nu = 0,1$, Nonlinear	17.5	24.8	15.2
$\nu = 0,3$, Nonlinear	19.7	36.9	18.4
$\nu = 0,1$, Linear	42.4	34.9	59

Table 5.1: Summary of the evaluated pressure gradient length for various magnetic shaping. For comparison, the values evaluated in 4.5 are reported.

The emerging picture is coherent with what has been observed in section 5.1. Positive triangularity presents the worse confinement properties, exhibiting higher pressure gradient lengths. It seems, also, that negative one enhances plasma containment.
An higher resistivity, moreover, reflects to higher L_p, but the increase is important only

in Global Positive configuration.
Finally, the results of the numerical evaluation in linear case is reported, through equation 4.13. The evaluated values are completely in disagree in both value and trend. This can be partially be attributed to the simplifications that it has been actuated in the linearisation process and the subsequent losses of self-saturation effects. Moreover in nonlinear results finite aspect ratio has been kept, providing an increase in stabilisation properties.

Nonlinear results, however, well match the ones found by Riva in [34]. In both works, it emerges that the most suitable configuration to confine the plasma is the one with negative triangularity, with an L_p of roughly 15, when $\nu = 0.1$. However, in his study, Riva takes surfaces characterised by a not negligible value of elongation. The confrontation, therefore, should be deepened with more subtle tools, since the two simulations are not directly comparable, except for a preliminar study.
On the whole, the general emerging picture for nonlinear simulation is one of improved confinement capacity for negative triangularity, consistent with previous studies.These results, in conflict with those presented in chapter 4, are more reliable than those obtained with a linear solver because they are able to capture more phenomena and take into account the stabilising effect of the finite aspect ratio.

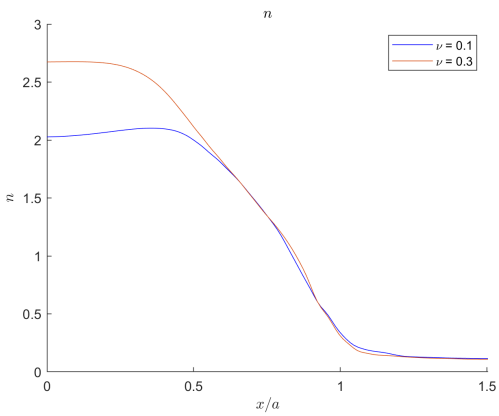

(a) GS, density radial distribution

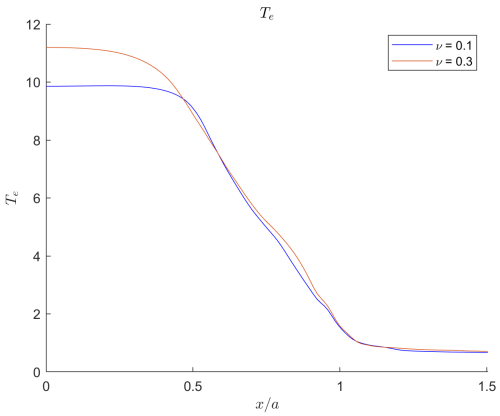

(b) GS, temperature radial distribution

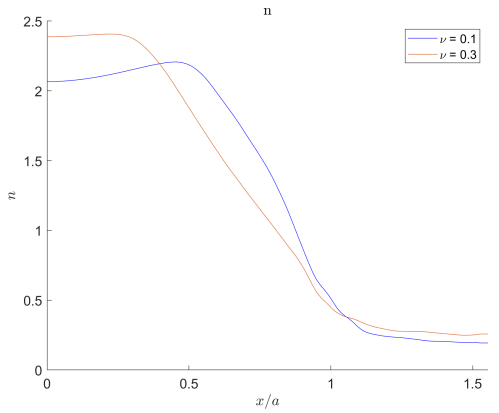

(c) GP, density radial distribution

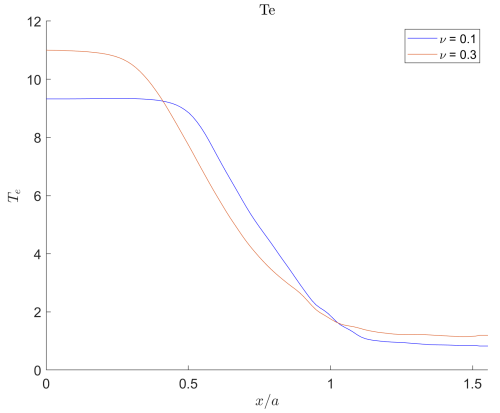

(d) GP, temperature radial distribution

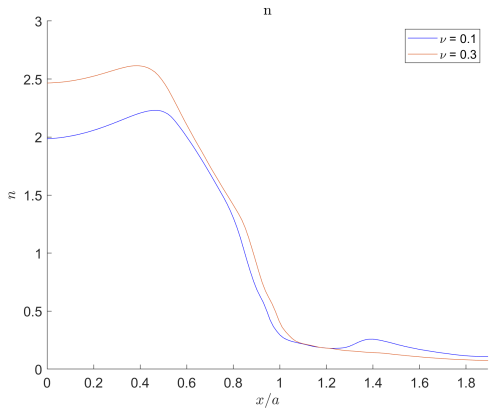

(e) GN, density radial distribution

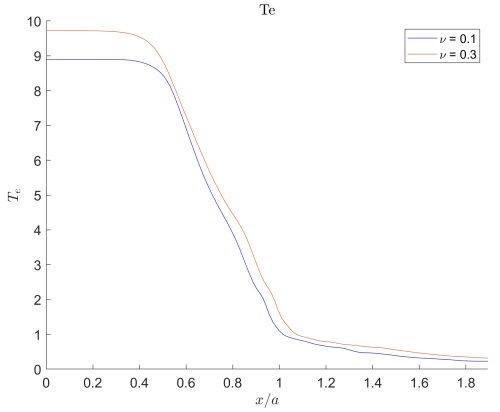

(f) GN, temperature radial distribution

Figure 5.4: Density and Temperature distribution at outer mid-plane in various magnetic configurations, evaluated through GBS code in $\nu = 0, 1$ and $\nu = 0.3$ case.

6 | Conclusions and Outlook

Understanding plasma turbulence in the tokamak edge is of fundamental importance since it regulates the overall performance of a tokamak, it controls the heat exhaust to the wall, the core confinements features and the transport properties of the plasma.
The tokamak boundary is usually characterised by a complex magnetic configuration, created through the interplay of plasma current and external magnetic coils. The magnetic configuration imposes to particles to stream along the closed loop field lines and contemporary to suffer a complex perpendicular dynamic, that eventually lead to the crossing of the Last Closed Flux Surface and the losing in the Scrape Off Layer. The shaping of the magnetic configuration and of the plasma is therefore a crucial topic. It allows to predict and control the confinement properties of the core and the instabilities in the magnetic configuration. The knowledge in the evolution of unstable modes in edge helps to predict and eventually control eventual bad behaviours in the tokamak. The analysis on the effects of plasma shaping allows to determine which are the most suitable configuration in terms of plasma control and core fusion conditions.
Chapter 2 describes the physical model considered in the present thesis, which is based on the drift-reduced Braginiskii equation.
Chapter 3 portrays the linear solver used to analyse plasma instabilities in the tokamak boundary. A linearisation of the GBS code is completed. The emerging eigenvalue problem has been discussed together to its numerical approach. The need for a poloidal discretisation of the magnetic surface has been considered and a method to meet this requirement has been inspected.
Chapter 4 reports on the main results obtained from linear simulations. In particular it has been firstly analysed the circular configuration, leading to known results, setting a benchmark for our discretisation method. Then the investigation is extended in the shaping domain. The resulting data suggest a destabilising role of the negative triangularity both for Resistive Ballooning Mode, and in the full model. Positive triangularity, instead, seems to have only mild effects on the instabilities growth-rate. It has been found that perturbations to magnetic equilibria localise preferentially in the Low Field Side of the tokamak and in the lower part, where the value of the safety factor is the highest.

This last behaviour it has been observed more remarkably in the negative triangularity configuration. Finally, the capability to compress the plasma has been judged through a nonlinear gradient removal theory. All the evaluated pressure gradient length are quite high with respect the edge thickness, suggesting an underneath laying numerical problem. Of the three configurations considered, however, the one with negative triangularity has been weighted as least capable to confine the plasma.
Chapter 5 details the results obtained from GBS simulations and provide a preliminary discussion and the effects of the Boussinesq approximation are quickly evaluated as not deeply influencing the discussion. Finally the pressure gradient has been retrieved basing on the nonlinear simulations. The results shows a bad confinement ability of the positive triangularity, which is worsened with the increase of plasma resistivity. Negative one, instead, emerges as the most suitable for plasma confinement. The results found in the linear discussion do not agree with the ones in this last.

Nonlinear, most reliable, data, in summary, portray negative triangularity as advantageous for the stability of the magnetic configuration. Plasma confinement capabilities were found to be better when negative triangularity shaping is imposed. In any case, this is not unequivocally found in both discussions and therefore a deeper analysis is necessary. The discordance between the linear analysis, the non linear one and that reported in [34] leads to questioning the validity of the results, in particular the linear ones. The succeeding of linear simulations in the circular benchmark suggests problems in the linear solver dealing with shaped configurations. Since only the geometric operators change between the two simulations, this gives clear clues as to where the problem may be.
Nevertheless, only three particular configurations and a single set of parameters were analysed. The analysis is therefore limited and different shaping or plasma conditions might lead to different results.
Future extensions of the present work can be found mainly in an extended analysis of different magnetic configurations and plasma parameters. Furthermore, it has been reported in previous literature that the aspect ratio and the Shafranov shift are stabilising parameters [34]. The inclusion of these variables, excluded in this work, may lead to results more in agreement with current literature.
In addition, a more thorough analysis of the geometric operators is desirable, especially with regard to their well-posedness. Such work has been initiated in the course of this thesis and there is evidence pointing to problems in the parallel gradient. Finally, extension to other branches of instability could lead to a more complete understanding of the phenomena involved, particularly when integrated with the Scrape Off Layer study. In

that case, the linear solver should be modified to deal also with open surfaces, and the edge conditions should be discussed.

Bibliography

[1] J. F. D. A. Zeiler, D. Biskamp and P. N. Guzdar. Three-dimensional fluid simulations of tokamak edge turbulence. *Physics of Plasmas*, 3(8), 1996.

[2] J. F. D. B. N. Rogers and A. Zeiler. Phase space of tokamak edge turbulence, the l-h transition, and the formation of the edge pedestal. *Phys. Rev. Lett.*, 81, 1998.

[3] A. Choudlhuri. *Astrophysics for Physicists*. Cambridge University Press, 2010. ISBN 9780521815533.

[4] R. M. C. de Jesus Jorge. *A moment-based model for plasma dynamics ar arbitrary collisionality*. PhD thesis, Faculté des sciences de base, EPFL, Lausanne, Switzerland, 2019.

[5] A. M. et al. Low-frequency linear-mode regimes in the tokamak scrape-off layer. *Physics of Plasmas*, 19, 2012. doi: 112103.

[6] J. et al. Socio-economic conditions for satisfying human needs at low energy use: An international analysis of social provisioning. *Global Environmental Change*, 2021. doi: https://doi.org/10.1016/j.gloenvcha.2021.102287.

[7] M. F. et al. The effect of triangularity on fluctuation in a tokamak plasma. *Nuclear Fusion*, 58, 2018.

[8] P. R. et. al. Plasma turbulence in the scrape-off layer of tokamak devices. *Physics of Plasmas*, 20, 2013. doi: 010702.

[9] Z. H. et al. Dependence of density fluctuations on shapre and collisionality in positive- and negative triangularity tokamak plasmas. *Plasma Phys. COntrol. Fusion*, 61, 2019.

[10] G. G. e. a. F. Wagner, G. Fussmann. Developement of an edge transport barrier at the h-mode transition of asdex. *Physical Review Letters*, 53(15), 1984.

[11] J. Freidberg. *Plasma Physics and Fusion Energy*. Cambridge University Press, 2007.

[12] v. W. C. G. Federici et al. URL `https://commons.wikimedia.org/wiki/File:DEMO_fusion_reactor_Bfield_surfaces.png`.

[13] S. G.Q.Yu and P. N. Guzdar. Two-dimensional modelling of blob dynamics in tokamak edge plasmas. *Physics of Plasmas*, 2006.

[14] P. Helander. Theory of plasma confinement in non-axisymmetric magnetic field. *Reports on Progress in Physics*, 77(8), 2014. doi: 087001.

[15] J. Huba. *NRL Plasma Formulary*. 2018.

[16] P. IEA. Multiple benefits of energy efficiency, 2019. URL `https://www.iea.org/reports/multiple-benefits-of-energy-efficiency`.

[17] J. Jacquinot. Fifty years in fusion and the way forward. *Nuclear Fusion*, 50(1), 2010. doi: 014001.

[18] K. S. Krane. *Introductory Nuclear Physics*. Wiley Sons, 1987.

[19] E. M. L. Lev D. Landau. *Course of Theoretical Physics, Volume 8: Electrodynamics of continuous Media*. Elsevier Science, 1995.

[20] E. M. L. Lev D. Landau. *Course of Theoretical Physics, Volume 2: The Classical Theory of Fields*. Elsevier Science, 1995.

[21] E. M. L. Lev D. Landau. *Course of Theoretical Physics, Volume 10: Physical Kinetics*. Elsevier Science, 1995.

[22] E. M. L. Lev D. Landau. *Course of Theoretical Physics, Volume 1: Mechanics*. Elsevier Science, 1995.

[23] P. R. M. Giacomin. Investigation of turbulent transport regimes in the tokamak edge by using two-fluid simulations. *Journal of Plasma Physics*, 86, 2020. doi: 905860502.

[24] C. Mercier. Equilibrium ans stability of a toroidal magnetohydrodynamic system in the neighbourhood of a magnetic axis. *Nuclear Fusion*, 4(3), 1964. doi: 213.

[25] A. Mosetto. *Turbolent regimes in the tokamak scrape-off layer*. PhD thesis, Faculté des sciences de base, EPFL, Lausanne, Switzerland, 2014.

[26] O. M. S. G. C. D. L. Our World Data. Primary direct energy consumption by source, world, 2020, . URL `https://ourworldindata.org/grapher/primary-energy-consumption-by-source?time=latest`.

[27] O. M. S. G. C. D. L. Our World Data. Crude oil spot prices, .

URL `https://ourworldindata.org/grapher/crude-oil-spot-prices?country=Brent~Dubai~Nigerian+Forcados~West+Texas+Intermediate`.

[28] B. N. R. P. Ricci and S. Brunner. High- and low-confinement modes in simple magnetized toroidal plasmas. *Physical Review Letters*, 2008.

[29] M. Passoni. Lecture on plasma physics. Dept. of Nuclear Eng., Politecnico di Milano. unpublished, 2020.

[30] L. J. P.W. Atkins. *Principi di Chimica*. Zanichelli, 2018. ISBN 9788808320971.

[31] A. Quarteroni. *Modellistica Numerica per Problemi differenziali*. Springer, 2016.

[32] Y. S. R. Aymar, P Barabaschi. The iter design. *Plasma Physics and Controlled Fusion*, 44(5), 2002. doi: 519.

[33] P. Ricci. Simulation of the scrape-off layer region of tokamak devices. *Journal of Plasma Physics*, 81(02), 2015.

[34] F. Riva. *Verification and validation procedures with applications to plasma-edge turbulence simulations*. PhD thesis, Faculté des sciences de base, EPFL, Lausanne, Switzerland, 2019.

[35] B. N. Rogers and W. Dorland. Noncurvature-driven modes in a transport barrier. *Physics of Plasmas*, 2005.

[36] B. N. Rogers and J. F. Drake. Enhancement of turbulence in tokamaks by magnetic fluctuations. *Phys. Rev. Lett.*, 79, 1997.

[37] G. Rossiter. Understanding and modelling fuel behaviour under irradiation. *Nuclear Fuel Cycle Science and Engineering*, 09 2012. doi: 10.1533/9780857096388.3.396.

[38] Z. R. S. Li, H. Jiang and C. Xu. Optimal tracking for a divergent-type parabolic pde system in current profile control. *Abstract and Applied Analysis*, 2014. doi: 10.1155/2014/940965.

[39] B. Scott. Three-dimensional computation of drift alfvén turbulence. *Plasma Physics and Controlled Fusion*, 39(10), 1997.

[40] B. Scott. The nonlinear drift wave instability and its role in tokamak edge turbulence. *New Journal of Physics*, 4(1), 2002.

[41] S.I.Braginskii. Transport processes in a plasma. *Reviews of Plasma Physics*, 1, 1965. doi: https://static.ias.edu/pitp/2016/sites/pitp/files/braginskii_1965-1.pdf.

[42] J. L. A. M. S.Joillet, F.D.Halpern and P. Ricci. Aspect ratio effects on limited scrape-off layer plasma turbulence. *Physics of Plasmas*, 2014.

[43] J. Wesson. Tokamaks. *Oxford, United Kingdom: Oxford University Press*, 2004.

[44] A. Zeiler. *Tokamak edge turbulence*. Max-Planck-Institut für Plasmaphysik, 1999.

A | Grad-Shafranov Equation and Solov'ëv equilibrium

In this section it will be derived the Grad-Shafranov equation describing magnetohydrodinamic equilibria. Along the discussion also the need of an external magnetic source for plasma confinement will be discussed. Finally the Solov'ëv equilibrium is stated.
The derivation has been carried on on the basis of [19] and [29]

To do so we must start from this set of equations describing a flow-less perfect conducting fluid:

$$\nabla P = \frac{1}{c}\vec{J} \times \vec{B} \tag{A.1}$$

$$\nabla \times \vec{B} = \frac{4\pi}{c}\vec{J} \tag{A.2}$$

$$\nabla \cdot \vec{B} = 0 \tag{A.3}$$

Equation A.1 corresponds to linear momentum conservation equation in MHD frame $\rho(\partial_t \vec{u} + \vec{u} \cdot \nabla \vec{u}) = -\nabla P - \frac{1}{4\pi}(\nabla \times \vec{B}) \times \vec{B}$ with vanishing velocity. Equations A.2 and A.3 are Maxwell equations for a magnetostatic field.
It is straightforward to see that $\vec{J}$ and $\vec{b}$ are perpendicular to ∇P, since $\vec{J} \cdot \nabla P = 0$ and $\vec{B} \cdot \nabla P = 0$. Supposing that $\vec{J}$ and $\vec{B}$ has a not vanishing modulus (otherwise we would have the trivial solution $P = 0$, $\vec{J} = 0$ and $\vec{B} = 0$) the magnetic field and the current density have perpendicular directions. Since they are both perpendicular to ∇P they describe a two-dimensional variety called magnetic surface.

It is possible to modify the equation A.1 in

$$\Pi = P\mathbb{1} - \frac{1}{4\pi}(\vec{B}\vec{B} - \frac{1}{2}B^2\mathbb{1}) \tag{A.4}$$

$$\nabla \cdot \Pi = 0 \tag{A.5}$$

where $\mathbb{1}$ describes the identity matrix and $\vec{a}\vec{b}$ is the matrix such that $[\vec{a}\vec{b}]_{i,j} = a_i b_j$, being $\vec{a}$ and $\vec{b}$ any two vector with the same dimension. Π is said stress tensor.

Since A.5, by developing $\nabla \cdot (\Pi \vec{r})$, integrating over a region of the space $\wp$, and applying Gauss theorem, it holds that

$$\int_{\wp} \left(3p + \frac{B^2}{8\pi}\right) dV = \oint_{\partial\wp} \left[\left(P + \frac{B^2}{8\pi}\right)\vec{r} - \frac{(\vec{B}\cdot\vec{r})\vec{B}}{4\pi}\right] d\vec{f} \tag{A.6}$$

This equation has been retrieved by S. Chandrasekhar and E. Fermi first in 1953.
If there is not some external magnetic sources and the fluid is confined in a finite region facing the external space were $P = 0$ we can expect the magnetic field going zero asymptotically as r^{-3} in a far region. If we let $\wp$ being the whole space, the right-hand side tends to zero. This is would lead to an impossible equation since the left-hand side is positive-defined. This implies the existence of an external magnetic field if a limited configuration is wanted to be maintained.

Following the work made by V.D.Shafranov and H.Grad in 1957, it is possible to reduce the set of equations A.2-A.3 to a single one.
In an axial-symmetric reference system, characterised by a right-handed poloidal reference system (R, ϕ, Z), since equation A.3 and $\nabla \cdot \vec{J} = 0$ it is possible to state that two fields Ψ and I exist such that

$$\vec{B_p} = \frac{1}{R}\nabla\Psi \times \hat{e}_\phi \tag{A.7}$$

$$\vec{J_p} = \frac{1}{2\pi R}\nabla I \times \hat{e}_\phi \tag{A.8}$$

where $\hat{e}_\phi$ is the versor pointing in ϕ direction and $\vec{a}_p = \hat{e}_\phi \times (\vec{a} \times \hat{e}_\phi) = \vec{a} - a_\phi \hat{e}_\phi$ is the reduction of vector $\vec{a}$ in the RZ plane[1].
It is worth to notice that Ψ is proportional to the magnetic flux through an horizontal surface or ray R and centred in the symmetry axis

$$\Psi(R, Z) = \int_0^R B_z r\, dr = \frac{1}{2\pi}\int_{D^2_R(0,0)} \vec{B}\cdot d\vec{f} \tag{A.9}$$

For the same reason I describes the total current flowing in the same surface.
Since it holds that $\nabla\Psi$ and ∇I are orthogonal to the magnetic field line and to the current line, they must be constant on the magnetic surfaces. If follows that any couple of the triplet Ψ, I and P can be expressed as the function of the third.
In particular it is possible to state that

$$P = P(\Psi) \qquad I = I(\Psi) \tag{A.10}$$

[1]This plane is named poloidal plane

From the equation A.2 and definitions A.7, A.8 it is possible to derive also the magnetic field's and current density's poloidal components:

$$B_\phi = \frac{2I}{cR} \tag{A.11}$$

$$J_\phi = -\frac{c}{4\pi R}\left[R\frac{\partial}{\partial R}\left(\frac{1}{R}\frac{\partial \Psi}{\partial R}\right) + \frac{\partial^2 \Psi}{\partial R^2}\right] = -\frac{c}{4\pi R}\Delta^* \Psi \tag{A.12}$$

The symbol Δ^*, a pseudo-Laplace elliptic operator, is said Stokes operator.
Finally, from equation A.1 it is possible to retrieve the Grad-Shafranov equation using equations A.7, A.8, A.11, A.12 and not letting $\nabla\Psi$ be identically null:

$$\Delta^* \Psi = -4\pi R^2 P' - \frac{4}{c^2}(I^2)' \tag{A.13}$$

where the symbol $(\cdot)'$ label the derivation with respect to Ψ.
To solve this equation an actual dependence must be assigned, arbitrarily, to P and I^2, depending on the configuration we are looking for. The boundary conditions are set on the boundary of the fluid volume to enforce continuity of Ψ and of its normal derivative. At the exterior of the fluid volume $P = 0$ and the magnetic field is determined by the homogeneous Grad-Shafranov equation A.13.
In that way a mapping for all the magnetic surfaces is defined:

$$\Psi(R, Z) = \Psi_0 \tag{A.14}$$

and all the fields are determined:

$$\vec{B} = \frac{1}{R}\nabla\Psi \times \hat{e}_\phi + \frac{2I(\Psi)}{cR}\hat{e}_\phi \tag{A.15}$$

$$\vec{J} = \frac{1}{2\pi R}\nabla I \times \hat{e}_\phi - \frac{c}{4\pi R}\Delta^*\Psi\hat{e}_\phi \tag{A.16}$$

$$P = P(\Psi) \tag{A.17}$$

It is interesting to deepen some of the feature of the solution of Grad-Shafranov equation. Firstly, the innermost surface usually degenerates in a curve where it holds that $\Psi(R_m, Z_m) = 0$. This locus is said magnetic axis. Some surface instead, can cross itself. It happens if the magnetic surface presents some point where $\nabla\Psi(R_X, Z_X) = 0$ and the (R_X, Z_X) point is said X-point. A surface with an X-point is usually said separatrix. If an X-point is present, it can happen that more than a magnetic axis is present. Usually, in practical application, only one of them is kept at the interior of the tokamak region,

the divertor preventing the plasma from reaching the others.
A well-known solution of equation A.13 is the so called Solov'ëv equilibrium. In this case the simplest non null solution are set for P and I^2, the linear one, in such a way that the derivatives in the equation are indipendant on Ψ. Ψ_0, R_m,α,λ are some constants. The equation we get and the relative solution is

$$\frac{dP}{d\Psi} = -\frac{\alpha}{4\pi}\Psi_0 \tag{A.18}$$

$$\frac{dI^2}{d\Psi} = -\frac{c^2}{4}\lambda R_m^2 \Psi_0 \tag{A.19}$$

$$\Delta^*\Psi = (\alpha R^2 + \lambda R_m^2)\Psi_0 \tag{A.20}$$

$$\Psi = \Psi_0 \left[\frac{1}{2}(\lambda R_m^2 + R^2)Z^2 + \frac{\alpha - 1}{8}(R - R_m)^2\right] \tag{A.21}$$

By a change of variables ($\xi = (R - R_0)/a$, $\zeta = Z/a$, $\bar{\Psi} = \Psi/\Psi_0$) it is possible to find its form:

$$\bar{\Psi} = \left[\xi - \frac{1}{2}\varepsilon(1 - \xi^2)\right]^2 + \left(1 - \frac{\varepsilon^2}{4}\right)[1 + \varepsilon\delta\xi(2 + \varepsilon\xi)]\left(\frac{\zeta}{\kappa}\right)^2 \tag{A.22}$$

In equation A.22 it is possible to notice some important parameters. First of all the aspect ratio, ε, describes how much the torus is thin, being the ratio between its major and minor radius, respectively R_0 and a. The ellipticity κ, instead, appears only as a multiplying factor for y. It is this parameter that controls how much the surfaces are squeezed into ellipsis. Finally, the triangularity δ is the only parameter that allows the symmetry with respect $(0, 0)$ point to be broken. It causes the deformation of the magnetic surfaces cross section toward a triangular shape.
It is finally worth to notice that near the magnetic axis, i.e. $\xi \sim \zeta \ll 1$, equation A.22 can be simplified in

$$\bar{\Psi} \simeq \left(\xi - \frac{1}{2}\varepsilon\right)^2 + \left(1 - \frac{\varepsilon^2}{4}\right)\left(\frac{\zeta}{\kappa}\right)^2 \tag{A.23}$$

In the magnetic axis prossimity, therefore, magnetic surfaces are ellipsis with the same ellipticity, slightly displaced on the ξ axis, with respect to R_0. The triangularity has effect only on higher order corrections in this region.

List of Figures

List of Tables

Acronyms

Acronym	Meaning
D	Deuterium
EOF	End of Life
GN	Global Negative
GP	Global Positive
GS	Global Symmetric
HFMP	High Field Mid-Plane
HFS	High Field Side
IdBM	Ideal Balooning Mode
InBM	Inertial Balooning Mode
LCFS	Last Closed FLux Surface
LFMP	Low Field Mid-Plane
LFS	Low Field Side
MHD	Magnetohydrodynamisc
PDE	Partial Differential Equation
RBM	Resistive Ballooning Mode
SOL	Scrape Off Layer
T	Tritium